

Electron Scattering and Nuclear Structure*

ROBERT HOFSTADTER

Department of Physics, Stanford University, Stanford, California

TABLE OF CONTENTS

	Page
I. Introduction.....	214
II. Scattering Theory	
(a) Scattering from Point Charges.....	215
(b) Scattering from Nuclei of Finite Size.....	216
(c) Phase-Shift Analysis of Electron Scattering.....	219
III. Various Scattering Phenomena	
(a) Nuclear Recoil.....	221
(b) Inelastic Scattering.....	222
(1) Excitation of Nuclear Levels.....	222
(2) Electrodissintegration—The Momentum Distribution of Nucleons in a Nucleus.....	223
(3) Breakup of the Nucleus.....	224
(4) Mesonic Processes.....	224
(5) Radiation.....	224
(c) Magnetic Scattering.....	225
(d) Angular Shapes of Nuclei.....	227
IV. Experimental Matters	
(a) The 190-Mev Apparatus	227
(b) The 550-Mev Spectrometer.....	231
(c) Behavior of Čerenkov Detectors.....	232
V. Results	
(a) The Proton.....	233
(b) The Deuteron.....	236
(c) The Alpha Particle.....	237
(d) Lithium and Beryllium.....	238
(e) Carbon.....	239
(f) Mg, Si, S, A, Sr.....	241
(g) The Medium-Heavy and Heavy Elements.....	242
VI. The Neutron.....	246
VII. The Validity of Electrodynamics.....	247
VIII. Comparisons with Other Measurements of Nuclear Sizes.....	248
IX. Summary.....	252
X. Conclusions.....	253
XI. Acknowledgments.....	254

I. INTRODUCTION

UNTIL a few years ago the principal information concerning geometric details of nuclear structure was derived from experiments on comparative energy releases in mirror nuclei, on fast neutron capture (and total) cross sections, on binding energies as they related

* The research reported here was supported jointly by the Office of Naval Research and the U. S. Atomic Energy Commission, and by the U. S. Air Force, through the Office of Scientific Research of the Air Research and Development Command.

to the Weizsäcker semiempirical formula, and, in the case of the heaviest elements, on the energies and half-lives of alpha activities. All approaches led to the same general range of values of the nuclear radii for a uniformly charged sphere, which was taken universally as the appropriate model of the nucleus. The results can be summarized in a well-known formula for the radius of a uniform sphere

$$R = r_0 A^{1/3} \times 10^{-13} \text{ cm.} \quad (1)$$

Henceforth, we shall measure all distances in terms of 10^{-13} cm as a unit and shall call this unit the fermi. For example, this formula puts the edge of the nuclear sphere of gold at a distance of 8.45 fermis from the center of the nucleus, if the constant r_0 is given a good compromise value of somewhere near 1.45 fermis. This model gives a uniform mass density to all nuclei, i.e.,

$$\rho_M = \frac{A}{(4/3)\pi R^3} \frac{\text{nucleons}}{(\text{fermi})^3} = \frac{1}{(4/3)\pi r_0^3} \frac{\text{nucleons}}{(\text{fermi})^3}$$

$$= 0.080 \frac{\text{nucleons}}{(\text{fermi})^3}, \quad (2)$$

and a variable charge density to the nuclei,

$$\rho_C = \frac{Ze}{(4/3)\pi R^3} = \frac{Z}{A} \frac{1}{(4/3)\pi r_0^3}$$

$$= \frac{Z}{A} \times 0.080 \frac{\text{proton charges}}{(\text{fermi})^3}. \quad (3)$$

These formulas are represented in Figs. 1(a) and 1(b) and show the relative size and shapes of a few representative nuclei.

In the last few years the work of Lyman *et al.*¹ Hofstadter *et al.*,²⁻⁴ Pidd *et al.*,⁵ and Fitch and Rainwater⁶ on electron scattering and μ -mesonic atoms showed that the radii determined by these methods were approximately 20% smaller for the heavier elements than those given by Eq. (1) with $r_0 = 1.45$ fermi. The μ -mesonic results also indicated that the lighter elements possessed smaller radii reduced according to

¹ Lyman, Hansen, and Scott, Phys. Rev. **84**, 626 (1951).

² Hofstadter, Fechter, and McIntyre, Phys. Rev. **91**, 422 (1953).

³ Hofstadter, Fechter, and McIntyre, Phys. Rev. **92**, 978 (1953). (The theoretical interpretation of the data was carried out by Yennie *et al.* See Secs. IIc and Vg.)

⁴ Hofstadter, Hahn, Knudsen, and McIntyre, Phys. Rev. **95**, 512 (1954).

⁵ Pidd, Hammer, and Raka, Phys. Rev. **92**, 436 (1953).

⁶ V. L. Fitch and J. Rainwater, Phys. Rev. **92**, 789 (1953).

the same formula: $r_0 = 1.20$ fermi. At the same time Cooper and Henley⁷ suggested that the data on mirror nuclei, relating, of course, to light nuclei, could be explained in terms of the smaller radii. Subsequently, some doubt has been expressed about this conclusion.⁸ In any case, the smaller radii obtained by these methods have come to be called "electromagnetic" radii. For want of a better word, the radii given by Eq. (1) for $r_0 = 1.45$ fermis may be called "nucleonic" radii, since the larger values arise from experiments in which nucleons interact with nuclei.

A considerable amount of work has been carried out on electron scattering at Stanford University in the period 1953–1956. This work has provided information on the charge densities of nuclei ranging from the proton to uranium. It appeared that something like a status report covering this material would be timely. Such a report could have the effect of gathering together various bits of existing information so that workers in the more general field of nuclear radii might have "electron scattering" radii and charge densities for comparison with their own data. It is the purpose of this review to present such an organization of the data, including some as yet unpublished work. This report should not be looked upon as a final word on the nuclear sizes and shapes determined by electron-scattering methods. Indeed, the future electron scattering program at high energies will undoubtedly yield some conclusions differing from the present ones and perhaps some surprises. However, it does not seem probable that major differences will arise and, therefore, a report at this time may be appropriate.

Although neither a historical nor a comprehensive report on the work of other laboratories engaged in electron scattering work is here intended, it is sincerely hoped that the present review will act as a stimulus to encourage workers in this and other fields to assemble their data on nuclear radii and even perhaps to encourage new experiments. A review on nuclear charge distributions by Ford and Hill⁹ has recently appeared and is one step in this direction.

II. SCATTERING THEORY

(a) Scattering from Point Charges

At the root of all elastic scattering processes involving charged particles lies Rutherford's famous formula. This formula,

$$\sigma(\theta) = \frac{z^2 Z^2 e^4}{16 E^2 \sin^4 \frac{1}{2}\theta}, \quad (4)$$

expresses the differential cross section $\sigma(\theta)$ for scattering incident charged point particles (charge ze) of *kinetic* energy E against immovable charged point centers,

⁷ L. N. Cooper and E. M. Henley, Phys. Rev. **92**, 801 (1953).

⁸ B. G. Jancovici, Phys. Rev. **95**, 389 (1954).

⁹ K. W. Ford and D. L. Hill, "The Distribution of Charge in the Nucleus," Ann. Revs. Nuclear Sci. A, 25–72 (1956).

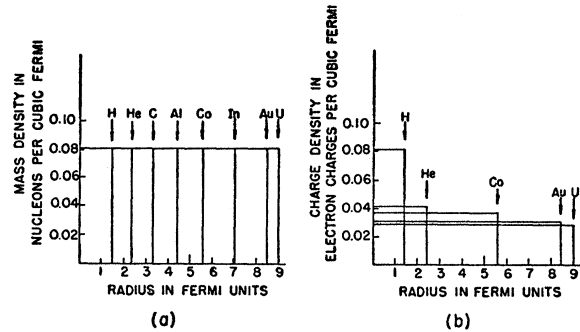


FIG. 1. (a) Mass density of nuclei for the uniform sphere [Eq. (2)]. (b) Charge density of nuclei for the uniform spherical model [Eq. (3)].

such as heavy nuclei (charge Ze), conceived as intense sources of an electric force field; θ is the polar angle of scattering. Rutherford scattering, [Eq. (4)], has been shown to be valid in quantum mechanics as well as in classical mechanics.¹⁰

While the Rutherford scattering law applies to alpha particles and protons of medium energies, it is not a relativistic formula and takes no account of the possible spins of the scattering partners nor of their possible identity.

Relativistic scattering of Dirac particles, such as electrons, against point nuclei, has been considered by Mott in a well-known paper.¹¹ In this case the incident particle, the electron, is assumed to have a spin (and a Dirac magnetic moment), although the scattering center (the nucleus) is assumed to have neither a spin nor a magnetic moment. Mott developed a series expression for the elastic scattering cross section and also gave an approximate formula, derived for elements that satisfy the inequality

$$\frac{Z}{137} = \frac{e^2}{\hbar c} \ll 1. \quad (5)$$

The approximation of Mott has been called Mott scattering and is given below in Eq. (6):

$$\sigma_M(\theta) = \left(\frac{Ze^2}{2mc^2} \right)^2 \left(\frac{1-\beta^2}{\beta^4} \right) \frac{1}{\sin^{4\frac{1}{2}\theta}} (1 - \beta^2 \sin^2 \frac{1}{2}\theta), \quad (6)$$

where

$$\beta = v/c, \quad z = 1; \quad (7)$$

v and c are velocity of the incident particle and the velocity of light, respectively. m is the rest mass of the electron. Equation (6) is written in terms of center-of-mass coordinates. Under conditions such as will be described in this review, β is always very close to unity and, consequently, in Eq. (6), β^4 will be put equal to

¹⁰ N. F. Mott and H. S. W. Massey, *The Theory of Atomic Collisions* (Clarendon Press, Oxford, 1949).

¹¹ N. F. Mott, Proc. Roy. Soc. (London) A124, 426 (1929); A135, 429 (1932).

unity, so that

$$1 - \beta^2 \sin^2 \frac{1}{2}\theta \approx \cos^2 \frac{1}{2}\theta \quad (8)$$

to a high degree of accuracy. Furthermore, the total energy of an electron is

$$E = \frac{mc^2}{(1 - \beta^2)^{\frac{1}{2}}} \quad (9)$$

so that

$$1 - \beta^2 = (mc^2/E)^2. \quad (10)$$

Making these changes in Eq. (6) results in the relativistic formula of Mott¹² for the elastic scattering of electrons

$$\sigma_M(\theta) = \left(\frac{Ze^2}{2E} \right)^2 \frac{\cos^2 \frac{1}{2}\theta}{\sin^4 \frac{1}{2}\theta} \quad (11)$$

with spin against spinless point nuclei of charge Ze . This formula is a very simple expression, indeed.

Equation (11) is quite accurate when condition (5) is satisfied. However, for more massive nuclei, where Z is large, Eq. (11) has been shown to be in error, as expected. Improvement of Eq. (11) has been attempted by many investigators and a description of these calculations will not be given here. McKinley and Feshbach¹³ and Feshbach¹⁴ have summarized the various investigations and have themselves put forward the proper corrections of Eq. (11) for nuclei of larger Z values. Their work has been confirmed by Dalitz,¹⁵ who used Born's second approximation.

When $Z/137$ is not large, a better approximation to Eq. (11) has been given by the above authors^{13,15}:

$$\sigma_F(\theta) = \left(\frac{Ze^2}{2E} \right)^2 \frac{\cos^2 \frac{1}{2}\theta}{\sin^4 \frac{1}{2}\theta} \left[1 + \frac{\pi Z}{137} \frac{(\sin \frac{1}{2}\theta)(1 - \sin \frac{1}{2}\theta)}{\cos^2 \frac{1}{2}\theta} \right] \quad (12)$$

under the same conditions applying to Eq. (11), except that condition (5) has been relaxed. At small angles, Eqs. (11) and (12) are equivalent to each other. Even at larger angles, the errors are rather small. The relative error in using (12) instead of (11) amounts to 3% and 7% for Si and Zn at $\theta = 90^\circ$, respectively, and to 17% and 35% for Si and Zn at 135° . Equation (12) may not be used for the heaviest nuclei. A closed formula, similar to (12) cannot be given for all values of Z , but numerical evaluation of the scattering for high Z is given in the paper of Feshbach.¹⁴ This author also gives the corresponding scattering results for positrons. Bartlett and Watson¹⁶ have made exact numerical calculations for the heavy nucleus mercury ($Z=80$). It may be noticed that the angular distributions given in

¹² See Eq. (36) for modifications required for the laboratory system of coordinates.

¹³ W. A. McKinley, Jr., and H. Feshbach, Phys. Rev. **74**, 1759 (1948). [These authors point out that Eq. (12) (above) was derived also by J. Schwinger.]

¹⁴ H. Feshbach, Phys. Rev. **88**, 295 (1952).

¹⁵ R. H. Dalitz, Proc. Roy. Soc. (London) **A206**, 509 (1951). [See also G. Parzen and T. Wainright, Phys. Rev. **96**, 188 (1954).]

¹⁶ J. H. Bartlett and R. E. Watson, Proc. Am. Acad. Arts Sci. **74**, 53 (1940).

Eqs. (11) and (12) are independent of incident energy. However, it must be remembered that these equations apply to scattering from an infinitely heavy nucleus and will, therefore, be strictly applicable only in the center-of-mass system of coordinates. For more realistic nuclei of conventional mass values, the center of mass will move forward at a considerable speed when the incident electrons have energies above 100 Mev and there will be a forward peaking of the angular distributions due to this effect at higher energies. This subject will be mentioned again later (see Sec. III-c).

Exact calculations for point-charge elastic scattering in copper and gold have been carried out at high electron energies by Yennie, Ravenhall, and Wilson^{17,18} by phase-shift methods and have been compared with the corresponding expressions in the first Born approximation (Fig. 1 of reference 17).

(b) Scattering from Nuclei of Finite Size

The first consideration of the effects of finite nuclear size on electron scattering appears to have been made by Guth.¹⁹ Later, and independently, similar ideas were developed by Rose.²⁰

Using more exact methods, Elton,²¹ Feshbach,²² and Acheson²³ have considered the finite size problem in relation to electron-scattering experiments at lower energies (up to 20 Mev), while Parzen²⁴ has dealt with an energy of 100 Mev for Pb. Still later, Smith²⁵ made a detailed study of this problem at high electron energies using the first Born approximation and subsequently presented the principal results in abbreviated form.²⁶

The results of Smith can be applied with accuracy only to light nuclei (Z small), but some of his results refer to both elastic and inelastic scattering. Schiff²⁷ has carried out similar first Born approximation calculations at high energies and has calculated other matters of interest in his paper.

Because the first Born approximation can be applied safely to light elements, and also, because the qualitative effects of finite nuclear size may be appreciated easily with this approximation, we shall devote the next few paragraphs to this topic.

(1) The First Born Approximation

Rose,²⁰ Smith,²⁵ and others have shown that, corresponding to Eq. (11) for a point charge, a scattering

¹⁷ Yennie, Ravenhall, and Wilson, Phys. Rev. **92**, 1325 (1953).

¹⁸ Yennie, Ravenhall, and Wilson, Phys. Rev. **95**, 500 (1954).

¹⁹ E. Guth, Wiener Anz. Akad. Wiss. No. 24, 299 (1934).

²⁰ M. E. Rose, Phys. Rev. **73**, 279 (1948).

²¹ L. R. B. Elton, Proc. Phys. Soc. (London) **A63**, 1115 (1950); **65**, 481 (1952); Phys. Rev. **79**, 412 (1950).

²² H. Feshbach, Phys. Rev. **84**, 1206 (1951).

²³ L. K. Acheson, Phys. Rev. **82**, 488 (1951).

²⁴ G. Parzen, Phys. Rev. **80**, 261 (1950); **80**, 355 (1950). [A numerical slip exists in the latter reference and the scattering curve (Fig. 1 of that paper) is not correct.]

²⁵ J. H. Smith, Ph.D., thesis, Cornell University, February, 1951 (unpublished).

²⁶ J. H. Smith, Phys. Rev. **95**, 271 (1954).

²⁷ L. I. Schiff, Phys. Rev. **92**, 988 (1953).

formula for elastic scattering, which replaces Eq. (11) when the nucleus is finite, must have the form

$$\sigma_s(\theta) = \left(\frac{Z e^2}{2E} \right)^2 \frac{\cos^2 \frac{1}{2}\theta}{\sin^4 \frac{1}{2}\theta} \left| \int_{\text{nuclear volume}} \rho(r) e^{i\mathbf{q} \cdot \mathbf{r}} d\tau \right|^2 \quad (13)$$

where $\rho(r)$ is the charge density within a nucleus as a function of radius vector from the center of the nucleus and $\hbar\mathbf{q}$ is the momentum transfer vector. The numerical magnitude of q for elastic scattering is, thus, given by

$$q = \frac{2E}{\hbar c} \sin^{\frac{1}{2}} \theta = \frac{2}{\lambda} \sin^{\frac{1}{2}} \theta \quad (14)$$

as shown in Fig. 2 where $|\mathbf{p}_1| = |\mathbf{p}_0|$. \mathbf{p}_0 and \mathbf{p}_1 are the incident and scattered momenta, respectively. λ in Eq. (14) is the reduced de Broglie wavelength of the high-energy incident electron:

$$\lambda = \hbar/p_0; \quad (15)$$

qr in Eq. (13) is, thus, a dimensionless phase factor.

The assumption is made once more that the nucleus does not recoil, or equivalently, that Fig. 2 is imagined to be in the center-of-mass frame.

It can be shown²⁵ that the integral in Eq. (13) can be reduced, so that

$$\sigma_s(\theta) = \left(\frac{Z e^2}{2E} \right)^2 \frac{\cos^2 \frac{1}{2}\theta}{\sin^4 \frac{1}{2}\theta} \left[\int_0^\infty \rho(r) \frac{\sin qr}{qr} \frac{dr}{4\pi r^2} \right]^2. \quad (16)$$

Since the quantity in square brackets multiplies the point charge cross section given by Eq. (11), it is customary to follow the precedent established in the electron diffraction and x-ray diffraction analogs of this equation and call this quantity

$$F = \frac{4\pi}{q} \int_0^\infty \rho(r) \sin(qr) r dr \quad (17)$$

the "form factor" or "structure factor" corresponding to a finite nuclear charge distribution. Indeed, the analogy is very close²⁸ and it is merely necessary to replace the electron cloud of an atom by the proton cloud of a nucleus. If the charge density in Eq. (16) is normalized to unity, the form factor F is a dimensionless quantity.

In dealing with the first Born approximation, the central idea is as follows: To obtain the actual scattering from a finite nucleus, it is necessary merely to multiply

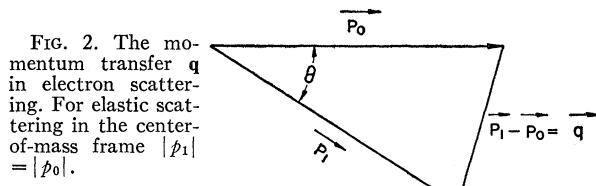


FIG. 2. The momentum transfer \mathbf{q} in electron scattering. For elastic scattering in the center-of-mass frame $|\mathbf{p}_1| = |\mathbf{p}_0|$.

²⁸ See, for example, Z. G. Pinsker *Electron Diffraction* (Butterworth Scientific Publications, London, 1953), p. 148, Eq. (7.25).

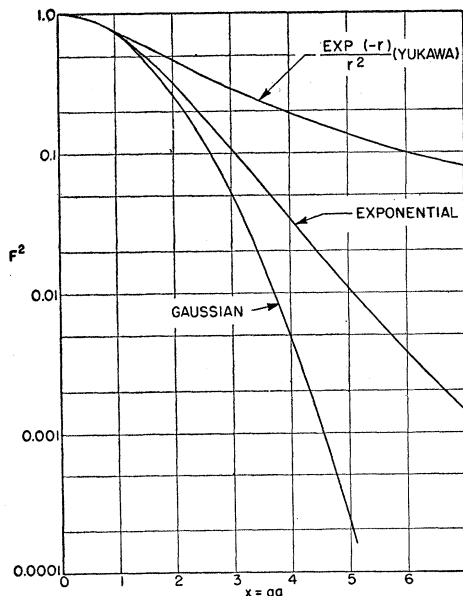


FIG. 3. The square of the form factor for typical charge distributions.

the point charge scattering cross section by the square of a form factor appropriate to the particular model of a nucleus under consideration. This procedure makes the calculations quite direct and usually quite simple, since it is only necessary to evaluate a single quadrature [Eq. (17)]. For light nuclei this is satisfactory. Unfortunately, for medium and heavy nuclei, this procedure fails. As is well known, the first Born approximation is equivalent to considering both the incident and diffracted waves as plane waves. Actually, the waves are distorted by the intense nuclear electromagnetic field, so that they can no longer be considered plane waves. Perhaps an equivalent way of saying this is that the first Born approximation amounts to a single scattering in the force field, while the exact scattering depends on a plurality of scatterings in the same force field.

In any event, the application of the Born formalism to elastic scattering provides a most valuable tool for analyzing electron scattering by light nuclei and is of qualitative value in discussing heavier nuclei. We shall make further remarks about the accuracy of the first Born approximation at a later time.

Making use of Eq. (17), we shall now give the results for a number of useful nuclear models. In order to present the calculations in the most succinct way, we have prepared in Table I²⁹ a series of form factors for several nuclear charge density distributions. In the table "a" represents the root-mean-square radius, weighted according to charge, and defined as

$$a = \int_0^\infty r^2 4\pi r^2 \rho dr = 4\pi \int_0^\infty \rho r^4 dr, \quad (18)$$

²⁹ This convenient form of the table is due to E. E. Chambers.

TABLE I. In this table $\rho(r)$ is the charge density function; "a" is the root-mean-square radius of the charge distribution; $F(qa)$ is the form factor; $x = qa$.

Model number	Name of model	Expression for charge density $4\pi a^3 \rho(r); y=r/a$	$F(qa); x=qa$
I	Point	δ function	1
II	Uniform	$\begin{cases} \frac{9}{5} \left(\frac{3}{5}\right)^{\frac{1}{3}} & \text{for } y \leq \left(\frac{5}{3}\right)^{\frac{1}{3}} \\ 0 & \text{for } y \geq \left(\frac{5}{3}\right)^{\frac{1}{3}} \end{cases}$	$5 \left(\frac{5}{3}\right)^{\frac{1}{3}} x^{-3} \left[\sin\left(\frac{5}{3}\right)^{\frac{1}{3}} x - \left(\frac{5}{3}\right)^{\frac{1}{3}} x \cos\left(\frac{5}{3}\right)^{\frac{1}{3}} x \right]$
III	Gaussian	$3 \left(\frac{6}{\pi}\right)^{\frac{1}{2}} \exp\left(-\frac{3}{2}y^2\right)$	$\exp(-x^2/6)$
IV	Exponential	$12\sqrt{3} \exp(-(12)^{\frac{1}{2}}y)$	$\left(1 + \frac{x^2}{12}\right)^{-2}$
V	Shell	$\delta(y-1)$	$x^{-1} \sin x$
VI	Hollow exponential	$\frac{200}{3} y \exp(-(20)^{\frac{1}{2}}y)$	$\left(1 - \frac{x^2}{60}\right) \left(1 + \frac{x^2}{20}\right)^{-3}$
VII	...	$\frac{75}{2} (30)^{\frac{1}{2}} y^2 \exp(-(30)^{\frac{1}{2}}y)$	$\left(1 - \frac{x^2}{30}\right) \left(1 + \frac{x^2}{30}\right)^{-4}$
VIII	Yukawa I	$\sqrt{2} y^{-2} \exp(-\sqrt{2}y)$	$\sqrt{2} x^{-1} \tan^{-1}(x/\sqrt{2})$
IX	Yukawa II	$6y^{-1} \exp(-\sqrt{6}y)$	$\left(1 + \frac{x^2}{6}\right)^{-1}$
X	Hollow Gaussian	$\frac{50}{3} \left(\frac{5}{2\pi}\right)^{\frac{1}{2}} y^2 \exp\left(-\frac{5}{2}y^2\right)$	$\left(1 - \frac{x^2}{15}\right) \exp\left(-\frac{x^2}{10}\right)$
XI	Generalized shell model	$\begin{cases} \frac{8}{\sqrt{\pi}} \frac{k^3}{(2+3\alpha)} (1+\alpha k^2 y^2) \exp(-k^2 y^2) \\ \text{where } k = \left[\frac{3(2+5\alpha)}{2(2+3\alpha)}\right]^{\frac{1}{2}} \end{cases}$	$\left[1 - \frac{\alpha x^2}{2k^2(2+3\alpha)}\right] \exp\left(-\frac{x^2}{4k^2}\right)$
XII	Modified exponential	$\frac{27}{\sqrt{2}} [1 + (18)^{\frac{1}{2}}y] \exp[-(18)^{\frac{1}{2}}y]$	$\left(1 + \frac{x^2}{18}\right)^{-3}$

where $\int_0^\infty 4\pi r^2 \rho dr$ is normalized to unity. The ratio $r/a = y$ and is a measure of radial distance in terms of the rms radius. In Table I, x is defined as qa .

If qa is small, where a is the root-mean-square radius, all form factors reduce to the simple expansion

$$F = 1 - (q^2 a^2 / 6) + \dots \quad (19)$$

At high energies this approximation is not useful because higher terms are needed.

Almost all useful nuclear shapes are included or approached more or less closely by one or another of the models listed in Table I. It is possible that repulsive core models are not sufficiently well approximated by any item of Table I. Several (form factors)² are shown in Figs. 3 and 4.

The usual procedure employed by the present author when using the Born method has been to try to fit experimental data in light nuclei with a few of the simple models. The search for a proper model is soon narrowed to one or possibly two of those given in Table I. The best fits of the parameter (or parameters) are then made.

It is also possible to invert the procedure and calculate the charge distribution from the experimental form factor. This has been done by Ravenhall³⁰ in analyzing accurate data on C¹² and will be a useful procedure when the experimental data become very precise. In the author's opinion, present-day accuracy does not warrant this approach in most cases, although

³⁰ D. G. Ravenhall (unpublished).

it should not be very long before this procedure will become valuable. In inverting Eq. (17) one obtains

$$\rho(r) = \frac{1}{2\pi^2 r} \int_0^\infty F(q) \sin(qr) q dq. \quad (20)$$

A useful fitting procedure has also been given by Schiff²⁷ for comparing the form factor F with a certain experimental quantity he finds which should agree with F if the correct model has been chosen.

(c) Phase-Shift Analysis of Electron Scattering

The work of Yennie, Ravenhall, and Wilson,^{17,18} Brenner, Brown, and Elton,³¹ and Elizabeth Baranger,³² showed conclusively that, for most nuclear models of medium and heavy elements, the exact elastic scattering cross sections departed markedly from those furnished by the first Born approximation. There appear to be two principal types of discrepancies, both apparent in Fig. 5, which is taken from the paper of Yennie *et al.*¹⁷ This figure refers to a uniform charge distribution in gold corresponding to an energy of about 150 Mev, and a similar charge distribution in copper corresponding to an energy of about 225 Mev. First, the Born approximation puts true zeroes into the form factors, while the accurate calculations show minima rather than true zeroes and in some cases only points of inflection corresponding to the zeroes of the first Born approximation. In the second place, radii determined from the Born approximation are, in general, larger than the exact calculations show. This may be made plausible by noticing the fact that the de Broglie wave of the incident electron appears to be shorter inside the nuclear electric force field than it is when free. This follows from the simple consideration that the effective kinetic energy appears to be greater within the field than outside the field because of the

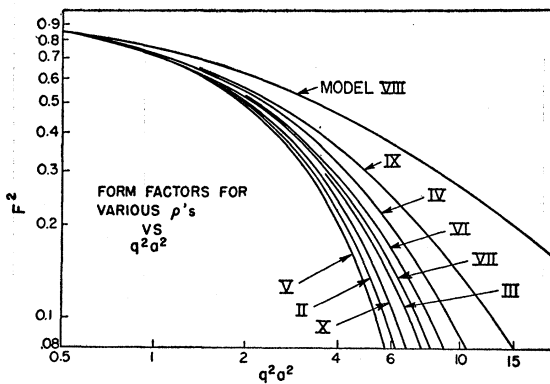


FIG. 4. The square of the form factor for several useful charge distributions at small values of qa . The model numbers refer to the charge densities of Table I. The graph was prepared by E. E. Chambers.

³¹ Brenner, Brown, and Elton, Phil. Mag. (7) 45, 524 (1954).

³² Elizabeth Baranger, Phys. Rev. 93, 1127 (1954).

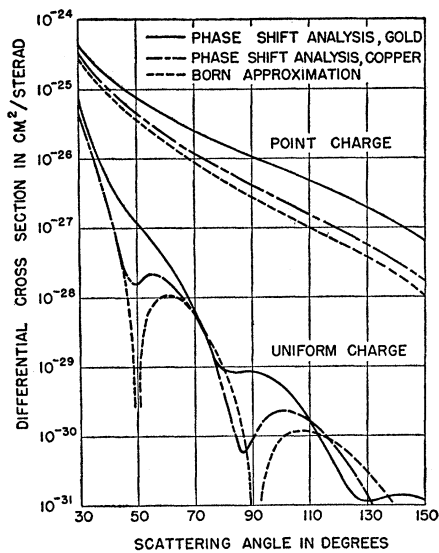


FIG. 5. Phase shift analyses by Yennie *et al.*^{17,18} for uniform spherical models of gold and copper. The point charge curves are shown as well as Born approximation results for all cases. The data refer to gold at approximately 150 Mev and copper at 225 Mev.

potential trough. The Born approximation does not take this fact into account. Since all lengths are measured by the electrons in units of λ , the nucleus appears larger in the Born approximation, where λ is not affected by the nuclear field, than in the exact case. Another way of saying this is that the diffraction features are associated with a given value of qR , where R is a typical radius parameter. Since $qR \propto R/\lambda$, a given diffraction feature will yield a smaller value of R , if λ is smaller than in free space. An argument of this type was given by Yennie *et al.*,¹⁷ but later it appeared that the Gaussian and exponential charge distribution did not conform exactly to the expected behavior. Perhaps the latter fact arises because the Gaussian and exponential charge distributions give monotonic angular distributions and, therefore, exhibit no diffraction features, a point upon which the plausibility argument rests. This matter is of some interest in understanding the physical features of the scattering phenomenon and it is to be hoped that an explanation may be forthcoming.

In any case, it is established that the first Born approximation may not be used for the heavy elements. In the case of copper, Fig. 5 shows that the Born approximation is much better than in gold, though by no means adequate. It is particularly bad in the neighborhood of the diffraction minima, which correspond to the true zeroes of the Born approximation. For nuclei with Z less than 10, the Born approximation will be satisfactory except right near the zeroes.

One reason why the first Born approximation is not good has been pointed out by Yennie *et al.*¹⁸ These authors find that the scattering amplitude, a complex

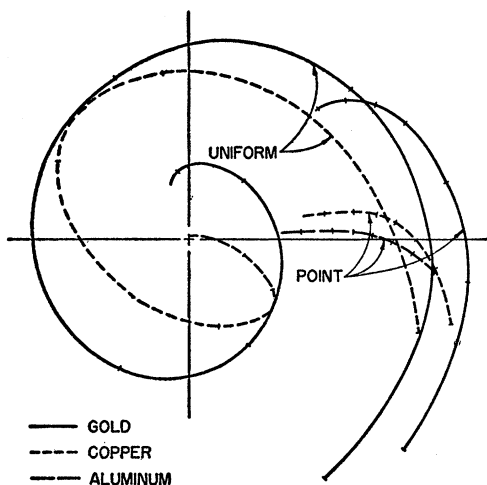


FIG. 6. \log_{10} of the modulus of the scattering amplitude plotted against θ (polar plot) for uniform models of gold, copper, and aluminum. Aluminum gives a result closest to a real number, indicating the validity of the Born approximation for light nuclei.

number in general, is widely different in the case of gold, from the scattering amplitude of the Born approximation. In the Born approximation the scattering amplitude is a real number and may be positive or negative and zero at a diffraction minimum. Figure 6 taken from their paper, shows the typical appearance of the \log_{10} of the modulus of the scattering amplitude plotted against the angle θ in a polar plot for a model of Type II (Table I).

Since the Born approximation cannot be used for the medium and heavy elements, and since no other simple method of approximation has yet been developed, the exact phase shift methods must be employed at present. There appears to be no other method available, at least, up to now, of fitting the experimental data other than by choosing a model and calculating the angular distribution. If differences from experiment are observed, the model is changed and a new calculation made. Successive attempts converge on a model, or series of related models. This procedure has been described in the paper of Yennie *et al.*¹⁸ where the Fermi smoothed uniform model was introduced. This particular model has the form of a Fermi type function³³ [Eq. (21)] and a typical shape is shown in Fig. 7. As may be seen later this model seems to be fairly close to the actual shape of the medium-heavy and heaviest nuclei.

$$\rho(r) = \frac{\rho_1}{\exp[(r-c)/z_1] + 1} \quad (21)$$

Experience with results of the type illustrated in Fig. 8 is helpful in deciding on the best model to fit the experimental data. Figure 8 shows three charge dis-

³³ Hahn, Ravenhall, and Hofstadter, Phys. Rev. 101, 1131 (1956). (The terminology of this paper is used for the Fermi model.)

tributions in the inset and the three corresponding theoretical angular distributions for gold at about 125 Mev obtained by the phase shift method. The uniformly charged sphere (square edge) shows the most prominent diffraction features. The most smoothed curve shows, as expected, the smoothest angular distribution. Brown and Elton³⁴ have carried out calculations with related models and have come to similar conclusions. Hill, Freeman, and Ford³⁵ have carried out a similar analysis using slightly different models and have also obtained the same kind of results. Simpler models have been treated by Glassgold.³⁶

Some brief remarks may be appropriate regarding the calculations of Yennie *et al.*¹⁸ and those of Brenner *et al.*³¹ These authors use the Dirac equation applied to a spherically symmetric static charge distribution. Quadrupole distortions are specifically avoided³⁷ and other dynamic effects are not taken into account such as possible dispersion corrections or correlations. The dispersion corrections have been considered by Schiff³⁸ who indicates that they should be small. The assumptions implicit in the theory, *viz.*, that the Dirac equation can be applied to the scattering, that the charge distribution can be treated as static, that electron-nucleon nonelectromagnetic forces do not exist, that the Coulomb law is valid at small distances, etc. can only be tested by the consistency of the theory and the scattering experiments at several energies and by the consistency of these conclusions with those found in other branches of nuclear physics. Thus far, there appear to be no reasons to doubt that the simple hypotheses made are not suitable, except possibly in the case of the proton (see Sec. VII).

Correlations between protons in the nucleus have

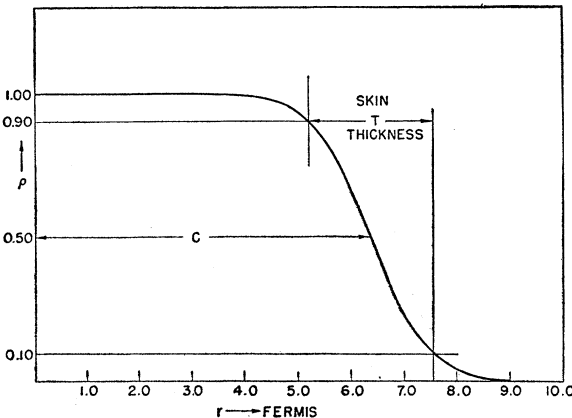


FIG. 7. The Fermi model. c is the distance to the half-density point and t is the skin thickness (90%-10% distance).

³⁴ G. E. Brown and L. R. B. Elton, Phil. Mag. 46, 164 (1955).

³⁵ Hill, Freeman, and Ford (private communication). (See also item 28 in reference 9.)

³⁶ A. E. Glassgold, Phys. Rev. 98, 1360 (1955).

³⁷ These will be discussed in Sec. Vg.

³⁸ L. I. Schiff, Phys. Rev. 98, 756 (1955).

been considered recently by Lewis³⁹ who has studied nonpotential scattering and who also gives some details about the second Born approximation.⁴⁰

III. VARIOUS SCATTERING PHENOMENA

Scattering phenomena can be broadly divided into elastic and inelastic types. In elastic scattering the kinetic energy of the two colliding particles remains constant in the center-of-mass frame. Alternatively, one may say that neither of the colliding bodies is raised to an excited state nor is a new particle produced. In our case, where one of the bodies is the electron, it suffices to observe that the nucleus remains in the ground state before and after the collision even though the nucleus may acquire a kinetic energy in the laboratory system. In inelastic scattering several types of behavior are observed, and they will be enumerated and described later.

In reality, because of the radiation by the electron of large numbers of soft quanta in the electric field surrounding the nucleus, it can truly be said that no scattering is precisely elastic. For example, if a 300-Mev electron is scattered by a heavy nucleus and emits three successive quanta of energies 0.1 ev, 1.0 ev, and 3.0 ev, the energy of the scattered electron is so minutely different from that of the incident energy that the collision may be termed elastic. In other words, if the detecting equipment cannot distinguish a 300-Mev electron from one with energy one part in 10^8 different from that energy, then the collision is elastic in any practical sense. We shall understand the term elastic collision in this sense. A correction for the radiation can be made when needed in comparing the experimental

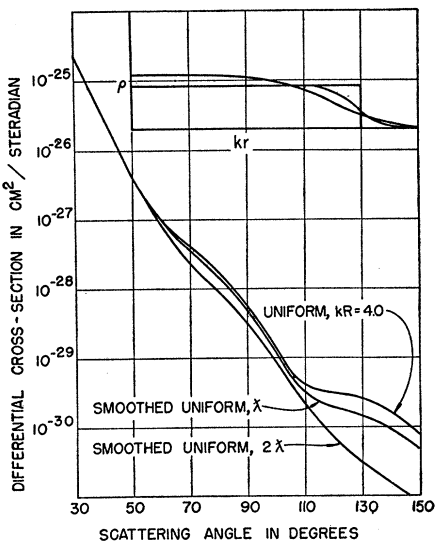


FIG. 8. Angular distributions for the three nuclear models shown in the inset. The uniform model shows the most prominent diffraction features.

³⁹ R. R. Lewis, Jr., Phys. Rev. 102, 544 (1956).

⁴⁰ R. R. Lewis, Jr., Phys. Rev. 102, 537 (1956).

results with theoretical expectations of elastic scattering.

(a) Nuclear Recoil

Before discussing the various types of inelastic scatterings, let us consider that kind which appears to be inelastic scattering in the laboratory frame, but which really is elastic scattering as seen in the center-of-mass frame. We mean to point simply to the change in energy suffered by a scattered electron arising from the transfer of kinetic energy and momentum to the struck nucleus. For example, an electron of incident energy 400 Mev will fly off with an energy of 326 Mev at 60° after scattering from a proton initially at rest. The remainder of the energy, 74 Mev, goes into the kinetic energy of the struck proton, which recoils at the appropriate angle demanded by the conservation theorems of energy and linear momentum. The collision is, of course, highly relativistic.

The relativistic kinematics of the collision are similar to those in the Compton effect, since at the high energies used in the scattering experiments ($E \gg mc^2$) the energy of the electron,

$$E = (c^2 p^2 + m^2 c^4)^{1/2}, \quad (22)$$

may be approximated with high accuracy by

$$E = cp, \quad (23)$$

and this is identical with the relation for x-rays. In place of the struck electron in the Compton effect, we now put the mass of the struck nucleus, and we are led to the result

$$E_n = \frac{E^2}{Mc^2} \frac{1 - \cos\theta}{1 + (E/Mc^2)(1 - \cos\theta)}, \quad (24)$$

where E_n is the kinetic energy of the struck nucleus and M its rest mass. This equation provides a simple and accurate means of calculating the energy of the scattered electron which is simply

$$E' = E - E_n. \quad (25)$$

At high energies it is entirely safe to use this expression, the error being less than 1% for 20 Mev and less than 0.1% for 200 Mev. When it is desired to calculate the exact energy loss, the kinematic collision equations can be obtained from many sources, e.g., Jánossy's book.⁴¹

An interesting observation from Eq. (24) results when θ is placed equal to π . In this case one obtains the usual result of the Compton effect

$$E_n = E \frac{2\alpha}{1 + 2\alpha}, \quad (26)$$

where

$$\alpha = E/Mc^2 \quad (27)$$

⁴¹ L. Jánossy, *Cosmic Rays* (Clarendon Press, Oxford, 1950), pp. 82-83.

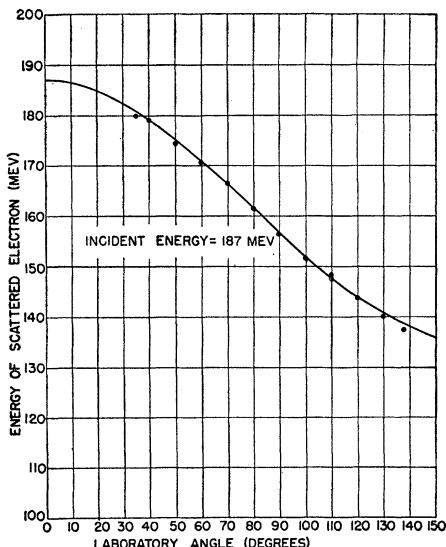


FIG. 9. Energy of electrons scattered from protons as a function of laboratory angle. The incident energy was approximately 187 Mev. The solid line is calculated from Eq. (24).

and

$$E' = E \frac{1}{1+2\alpha}. \quad (28)$$

When $2\alpha \gg 1$, thus, when the energy of the incident electron is large compared with Mc^2 ,

$$E' \rightarrow (Mc^2/2) \quad (29)$$

and the energy of the electron scattered near 180° saturates at one half of the rest energy of the struck nucleus. For a collision of an electron with a proton, the limiting energy of an electron scattered backward is 469 Mev. Therefore, valuable scattering experiments, using relatively small detecting devices, should be possible in the backward hemisphere even at very high electron energies, say, at 10 Bev, and possibly at higher energies if the cross sections are not too small.

To illustrate the application of Eq. (24) to an actual scattering problem,⁴² Fig. 9 shows the experimentally determined kinetic energy of the electrons scattered at various angles from a beam of 187-Mev electrons incident on a gaseous target of hydrogen. The solid line is the theoretical curve computed from Eq. (24). The points are experimental. The small deviations at small and large angles are due to energy loss of the electrons as they go obliquely through the gas chamber walls. The energies were measured from several sets of data obtained with a magnetic spectrometer from elastic scattering peaks such as those in Fig. 10. The incident energy for the several runs averaged together in Fig. 9 varied by about 1%.

The recoil energies in Eq. (24) vary inversely as the mass number of the target nucleus and, hence, it is

⁴² R. W. McAllister and R. Hofstadter, Phys. Rev. **102**, 851 (1956).

possible to separate the elastic scattering peaks from two elements in a compound target or even from two isotopes of the same element. In studying the scattering of electrons from protons, polyethylene proves to be a valuable target material, since the proton elastic scattering peak is situated far from the elastic carbon peak and the background subtraction problem is greatly simplified. The method has advantages, but to use it one must be sure that inelastic scattering from the heavier target does not fall at the same energy as the elastic peak of the element or isotope studied.

(b) Inelastic Scattering

In elastic scattering the nucleus is observed in its ground state before and after the scattering event. In scattering of an inelastic variety, the nucleus is left in a different condition after the scattering event has taken place: the passing electron has produced a transition from the nuclear ground state to some excited state or to a level in the continuum. We describe the following possibilities.

(1) Excitation of Nuclear Levels

The nucleus may be raised to a discrete excited state by the incident electron. The electron then flies off with its energy reduced by just the amount by which the nucleus has been excited. Figure 11 shows an example⁴³ of this phenomenon observed in carbon at an incident energy of 187 Mev and at a scattering angle of 80° . The elastic peak is seen near 185.1 Mev, shifted slightly downward because of the recoil of the carbon nucleus (and straightforward collision energy loss in the target). To its left, near 180.7 Mev, is an inelastic scattering peak somewhat less than half as large as the elastic peak. This scattering arises from excitation of the 4.43-Mev level of C^{12} . Also apparent in Fig. 11 are the smaller peaks due to scattering from the levels at 7.65 Mev, 9.61 Mev, and other higher levels. This behavior is characteristic of the inelastic scattering observed in many elements arising from the excitation

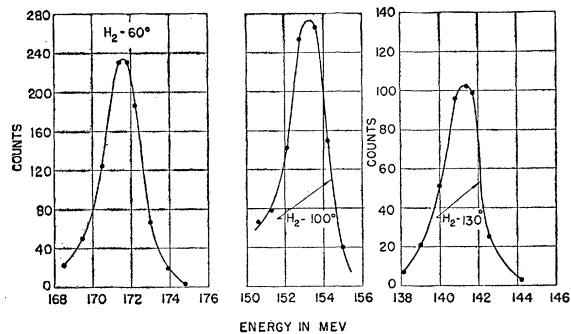


FIG. 10. Elastic peaks showing 187-Mev incident electrons scattered from protons at 60° , 100° , 130° . Note the shifts arising from recoil of the proton.

⁴³ J. H. Fregeau and R. Hofstadter, Phys. Rev. **99**, 1503 (1955).

of nuclear levels. This effect was first found in the case of beryllium^{3,44} and has since been observed in lithium,⁴⁵ magnesium, silicon, sulfur, calcium, strontium,⁴⁶ etc.

Inelastic scattering of this type has great intrinsic interest, because it permits the nucleus to be examined while it makes transitions to higher levels and, in fact, to higher levels than reached by most other methods. The values of transition matrix elements and the nuclear angular momenta and parities of states may also be found.⁴⁷ In qualitative language one sees, in this type of inelastic scattering, the dynamic character of the nucleus, while in the elastic scattering the static character of the nucleus in its ground state is revealed. Experimentally speaking, however, inelastic scattering of this type poses some problems when one is attempting to disentangle the elastic scattering peaks from others nearby. More will be said later about inelastic scattering and its interpretation.

(2) Electrodisintegration—(The Momentum Distribution of Nucleons in a Nucleus)

A second type of inelastic scattering occurs when a proton or neutron is ejected by the passing electron. This process may be called "electrodisintegration" and was observed in the case of deuterium⁴⁸ and has subsequently been seen also in helium⁴⁹ and in other elements. Figure 12 demonstrates the inelastic continuum due to this process in helium at BCDE where A shows the elastic peak in the scattering of 400-Mev (more exactly, 395-Mev) electrons from the alpha particle as

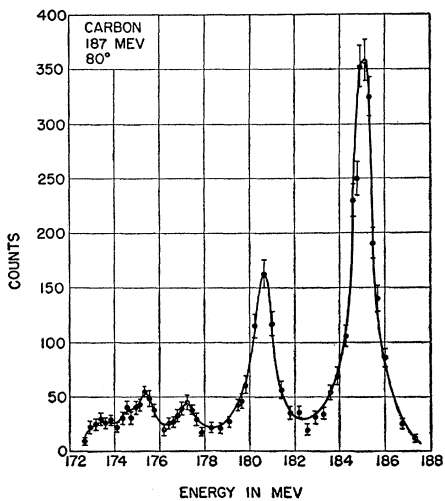


FIG. 11. The elastic scattering peak from carbon near 185 Mev and the inelastic scattering peaks from excited states of carbon. The peak near 180.7 Mev is associated with the 4.43-Mev level.

⁴⁴ McIntyre, Hahn, and Hofstadter, Phys. Rev. **94**, 1084 (1954).

⁴⁵ W. Hutchinson and J. F. Streib (unpublished).

⁴⁶ R. H. Helm, Ph.D. thesis, Stanford University, February, 1956.

⁴⁷ L. I. Schiff, Phys. Rev. **96**, 765 (1954).

⁴⁸ J. A. McIntyre and R. Hofstadter, Phys. Rev. **98**, 158 (1955).

⁴⁹ R. Blankenbecler and R. Hofstadter, Bull. Am. Phys. Soc. Ser. II, **1**, 10 (1956).

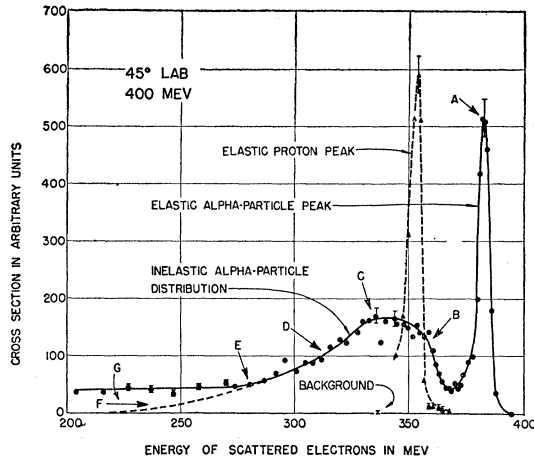


FIG. 12. Electrodisintegration of the alpha particle at 400 Mev and 45°. The elastic peak is shown at A. The inelastic continuum BCDE is related to the momentum distribution of nucleons within the alpha particle. G points to negative pion production. (See Sec. IVc in text.)

observed at a scattering angle of 45°. The figure also shows a comparison electron scattering peak from free protons in hydrogen. The different recoil energies of the proton and alpha particle may be noted. In scattering accompanied by the ejection of a nucleon, the scattered electron's energy must be reduced by at least the binding energy of that particular nucleon in the nucleus. In the case of the alpha particle, the ejection of one neutron or proton takes approximately 20 Mev and Fig. 12 shows that the high-energy slope of the inelastic continuum will plunge into the axis at approximately this interval from the elastic alpha peak

The low-energy side of the continuum results from the fact that a proton or neutron may be ejected with a higher energy than that given to a free proton, e.g., as given by the position of the free-proton peak in Fig. 12. The ejected proton or neutron may likewise receive less energy than a free proton recoil if that nucleon was moving with a velocity component, prior to ejection, in a direction opposite to that of the incident electron. If the nucleon was moving with a component parallel to the incident electron's path, the recoil energy will be larger and the scattered electron will, therefore, have less energy. If, finally, the nucleon is moving essentially perpendicular to the path of the incident electron, the scattered electron will have an energy, coinciding in first approximation, with the energy of electrons scattered from the free proton, except for the correction mentioned above, *viz.*, the energy required to remove the nucleon from the nucleus, i.e., its binding energy. This makes plausible the appearance of the peak of the elastic continuum at an energy approximately 20 Mev below the free-proton peak in Fig. 12. Similar features are seen in Fig. 13 where the scattering angle is 60° and the elastic alpha

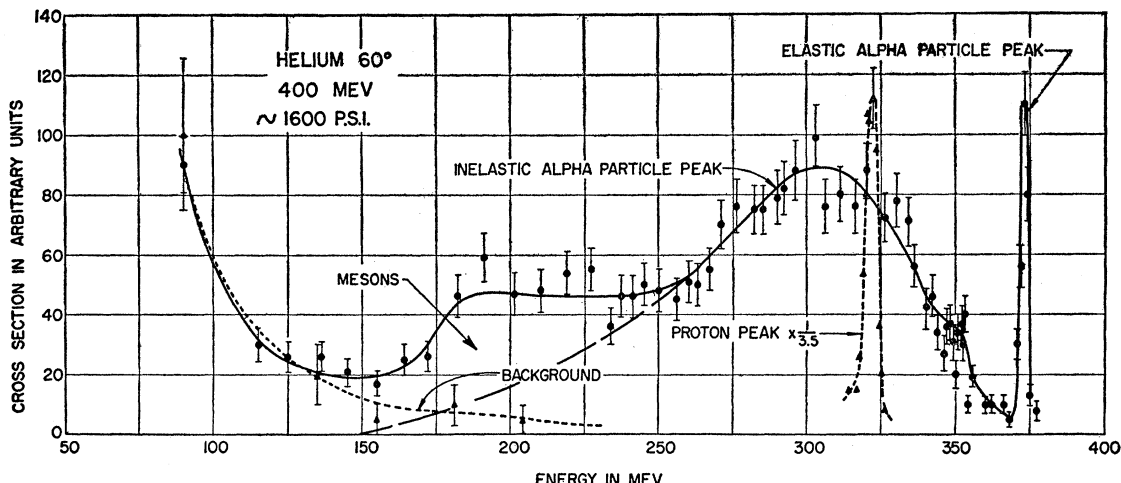


FIG. 13. The elastic and inelastic scattering of electrons from the alpha particle at 400 Mev and 60°. The area labeled "mesons" refers to negative pions produced in the target and emerging with the same momentum as the corresponding scattered electrons. The free proton peak is shown for comparison.

peak has become much smaller relative to the inelastic continuum. The same phenomena are observed in the case of inelastic scattering from the deuteron⁴⁸ where the binding energy is only 2.23 Mev. The study of such inelastic continua will, therefore, furnish valuable information about the momentum distribution of nucleons in a nucleus.

(3) Breakup of the Nucleus

A process similar to (2) may occur, except that more than one particle may be ejected simultaneously. It could be expected that fragments such as deuterons or alpha particles could be emitted. Possibly even fission may occur in some of the heavier nuclei. Such nuclear breakup undoubtedly occurs and contributes to the continua such as shown in Fig. 12. It will be difficult to separate single- and multi-nucleon breakup processes experimentally unless coincidence experiments or separate experiments searching specifically for nucleonic fragments can be performed.

(4) Mesonic Processes

A passing electron may cause charged or neutral mesons of various types to be emitted from the nucleus or from a nucleon. The materialization energy of such a particle must, of course, be provided and this is in the neighborhood of at least 140 Mev. Hence, scattered electrons engaging in this process will lie at low energies in the inelastic continua. Pi mesons made by this process have been detected in the very same apparatus in which the electrons were detected.^{49,50} In fact, part of the low energy tail of Fig. 13, indicated by the label, is due to pi mesons having the same momenta as electrons received by the spectrometer at this setting. The electrons themselves, the meson producers, so to

speak, have not yet been separated from the others scattered into the inelastic continuum by moving nucleons, but there is no doubt that they are present.

(5) Radiation

Accompanying both elastic and inelastic scattering of electrons is a radiation of photons. When the radiation goes mainly forward, this radiation is the familiar bremsstrahlung x-ray beam observed in betatrons and synchrotrons. Bremsstrahlung may be observed at any angle and may result from an electron scattered at almost any angle. Thus, the low-energy side of any elastic or inelastic peak will show a tail which decreases in the manner typical of radiative phenomena, i.e., as the reciprocal of the energy of the emitted radiation. At large energy losses of the incident electron (> 10 Mev), a single x-ray will be emitted. At small energy losses, say less than 1 ev, a Poisson distribution in the number of emitted photons will represent the distribution of prevailing radiation. Of course, a large single loss may also be accompanied by a shower of very low-energy photons. The radiative loss is probably well explained by the Bethe-Heitler theory, although it would be interesting to study the $1/(E - E_0)$ spectrum in some detail at large angles. This has not yet been done. A Born approximation theory has been formulated by Biel and Burhop for the process involving a finite nucleus.⁵¹

The foregoing remarks refer to the emission of real quanta. It is well known that virtual emission and absorption of radiation also occur during the act of scattering. The calculations including this process as well as real radiation were performed by Schwinger⁵² and

⁵¹ S. J. Biel and E. H. S. Burhop, Proc. Phys. Soc. (London) A68, 165 (1955).

⁵² J. Schwinger, Phys. Rev. 75, 898 (1949).

later by Suura.⁵³ Suura has given more general validity to the Schwinger calculation. For most practical purposes a correction must be added to the experimental scattering to compensate for the real and virtual radiative processes for photon energies less than or equal to ΔE . This correction is given by Schwinger as

$$I = I_0 e^{-\delta_r}, \quad (30)$$

where I is the measured scattering intensity and I_0 the value to be compared with a theory assuming elastic scattering alone. δ_r is the Schwinger radiative correction which is given sufficiently well by

$$\delta_r = \frac{4\alpha}{\pi} \left\{ K \left[\log \left(\frac{2E}{Mc^2} \sin \frac{\theta}{2} \right) - \frac{1}{2} \right] + \frac{17}{12} \right\}, \quad (31)$$

where

$$K = \log \frac{E}{\Delta E} - \frac{13}{12}, \quad (32)$$

and in which E is the energy of the scattered electron, α the fine structure constant, and m the rest mass of the electron. In practice, ΔE amounts to the smallest energy considered to be resolvable from the main elastic peak. This is usually something like the half-width of the elastic peak. The Schwinger correction is not very sensitive to practical values of ΔE and besides has a very small angular dependence. For this reason, it may usually be omitted in discussing angular distributions, although, in cases where accuracy is important, it must be taken into account. In studies where absolute cross sections are important, it is essential to include it. No detailed experimental test of the Schwinger correction has been made. A typical Schwinger correction may vary from 14% at 40° to 17% at 135° , where $E/\Delta E$ is in the neighborhood of 100.

The emission of real radiation, i.e., bremsstrahlung, by electrons emerging from a target of finite thickness, must also be corrected for. This results in a correction such that

$$I_1 = I e^{\delta_B} \quad (33)$$

where δ_B is given by⁵⁴

$$\delta_B = \frac{t}{\log 2} \log \frac{E}{\Delta E}, \quad (34)$$

and where "t" is the average target thickness through which the electrons pass (along the directions of the incident beam and scattered beam) and ΔE is the full width of an elastic peak at half-maximum. I_1 is the corrected intensity.

(c) Magnetic Scattering

For most nuclei, the elastic scattering is due entirely to the electric charge of the nucleus, i.e., to the electric

⁵³ H. Suura, Phys. Rev. **99**, 1020 (1955).

⁵⁴ H. A. Bethe and J. Ashkin, *Experimental Nuclear Physics*, edited by E. Segré (John Wiley and Sons, Inc., New York, 1953), Vol. I, Part II, p. 272. This result is derived from the original Bethe-Heitler theory.

field of force surrounding it. However, owing to finite size effects, we have seen that the elastic scattering at large angles and high energies can be reduced by many orders of magnitude below the scattering expected from a point charge and the Coulomb interaction. We shall ask the question: Does *any* elastic scattering remain at all after the charge scattering has dropped below experimental recognition? Another related question is: Does a neutron scatter electrons at high energy and do neutrons in a nucleus scatter electrons? The answers are affirmative in all cases and magnetic scattering has actually been observed in experiments at Stanford.^{42,55}

The proton.—Elastic scattering of high-energy electrons by the magnetic moment of the proton had actually been predicted by Rosenbluth⁵⁶ in 1950. Rosenbluth showed that there is a contribution to the elastic scattering from both the Dirac and the Pauli components of the proton's magnetic moment. The Pauli moment is usually referred to as the "anomalous" part of the proton's magnetic moment. Rosenbluth's results may be presented as follows: For a protonic point charge and point magnetic moment, the differential cross section σ_p is^{56a}:

$$\sigma_p(\theta) = \sigma_{NS} \left\{ 1 + \frac{q^2}{4M^2} [2(1+\mu)^2 \tan^2 \frac{1}{2}\theta + \mu^2] \right\}, \quad (35)$$

where

$$\sigma_{NS} = \frac{e^4}{4E^2} \frac{\cos^2 \frac{1}{2}\theta}{\sin^4 \frac{1}{2}\theta} \frac{1}{1 + (2E/M) \sin^2 \frac{1}{2}\theta} \quad (36)$$

and

$$q = \frac{2}{\lambda} \frac{\sin \frac{1}{2}\theta}{[1 + (2E/M) \sin^2 \frac{1}{2}\theta]^{\frac{1}{2}}}. \quad (37)$$

Equation (36) is simply Eq. (11), when $Z=1$ (proton) and when proper modifications are made in going from the center-of-mass frame to the laboratory frame of reference. The subscripts NS refer to the fact that Eq. (36) is the proper scattering formula for a proton without magnetic moment or spin (NS=no spin). Corresponding to the "q" of Eq. (14), the new q ($\hbar=1$) in Eq. (37), is the momentum transfer in the laboratory frame and has a suitable modifying factor required in this frame of reference. [Note that Eq. (37) follows simply from Eq. (24) by placing $1-\cos\theta = 2\sin^2 \frac{1}{2}\theta$ and putting $\hbar q = p_n$ where $E_n = p_n^2/2M$. Equation (37) is not restricted, however, to these approximations.]

Finally, Eq. (35) shows that a point proton scatters as a Mott proton would except that the scattering

⁵⁵ R. Hofstadter and R. W. McAllister, Phys. Rev. **98**, 217 (1955).

⁵⁶ M. N. Rosenbluth, Phys. Rev. **79**, 615 (1950). See also the reference to L. I. Schiff in this paper.

^{56a} Because of common practice we write Rosenbluth's formula in units such that $\hbar=c=1$, $e\hbar/Mc=e/M$, in these units and is the nuclear magneton. Thus, μ represents 1.79 nuclear magnetons (Pauli moment) and 1.00 represents the Dirac moment. $1.00+1.79=2.79$ is the entire proton moment in nuclear magnetons.

formula is modified by a factor S_p , which takes magnetic scattering into account:

$$S_p = 1 + S = 1 + \frac{q^2}{4M^2} [2(1+\mu)^2 \tan^2 \frac{1}{2}\theta + \mu^2]. \quad (38)$$

S_p is an energy-dependent term, since q depends on energy [$\lambda \propto (1/E)$]. S_p also depends on the scattering angle θ . The factor S_p becomes much larger than unity at high energies (q large) and large angles ($\tan^2 \frac{1}{2}\theta$ large). Under these conditions S_p is dominant in the scattering phenomenon, and the principal part of the scattering is now due to the quantity S which contains a $\tan^2 \frac{1}{2}\theta$ term. When associated with Eq. (36), the factor S_p produces a flattening-off of the cross section at large angles and as a result the magnetic moment scattering by a point is much more isotropic than Mott scattering from a pure charge.

Now if the proton should happen to be neither a point charge nor a point magnetic moment (as meson theory might lead us to expect), this would require the existence of form factors, whose presence would lead to a reduction of the effective values of the charge and magnetic moment. In fact, Rosenbluth⁵⁶ carried out such a calculation using a weak coupling meson theory. However, since a satisfactory meson theory is not known to exist nowadays, it is preferable to use phenomenological form factors to allow for the finite size effects in the proton. The "size" of the proton and its "shape" are assigned to the virtual cloud of mesons, both charged and neutral, which the proton may emit and reabsorb. Phenomenological form factors, F_1 and F_2 , have been introduced by Yennie, Lévy, and Ravenhall^{57,42} in accordance with the Rosenbluth scheme and a formalism due to Foldy.⁵⁵ F_1 is introduced to take care of a spread-out charge and a spread-out Dirac magnetic moment. F_2 is an independent quantity and takes care of a spread-out Pauli moment. Equation (39) shows how S_p is modified by the introduction of F_1 and F_2 :

$$\sigma(\theta) = \sigma_{NS} \left\{ F_1^2 + \frac{q^2}{4M^2} [2(F_1 + \mu F_2)^2 \tan^2 \frac{1}{2}\theta + \mu^2 F_2^2] \right\}. \quad (39)$$

F_1 and F_2 are each independent functions of the momentum transfer q .

The neutron.—In the case of the neutron, because its charge is zero, a naive approach would be to place $F_1=0$. This is actually correct in the static limit $q \rightarrow 0$. However, as the energy of the incident electrons increases and the wavelength, therefore, decreases, an electron which passes through a neutron cloud becomes sensitive to the positive and negative charge (or effective charge) clouds it sees and can suffer a deflection due to these charges. The effect would be expected to be small if the dimensions of the neutron's positive and

negative meson clouds are small. Thus, F_1 for a neutron really approaches a term $-\frac{1}{6}q^2 r_{1n}^{-2}$ as indicated by Eq. (19), with the leading static term there placed equal to zero.⁵⁷ The quantity F_2 for a neutron will be more conventional since the neutron does have a static magnetic moment equal to -1.91 nuclear magnetons. Hence,

$$F_{2n} = 1 - \frac{q^2 r_{2n}^{-2}}{6} + \dots \quad (40)$$

as long as qr_{2n} is small.

A critical review of the concepts discussed above is given by Yennie *et al.* in reference 57. We shall merely note here the further thought that a breakdown of electrodynamics, say, a failure of the Coulomb law at small distances, will have exactly the same effect as a finite size. We shall return to this point later (Sec. VII).

The deuteron.—In the case of magnetic scattering from the deuteron, the expected cross section should be smaller than the proton's, because the deuteron's static magnetic moment is $\mu_D = 0.858$ nuclear magneton, whereas the moment of the proton is 2.79 nuclear magnetons. Since the cross section is expected to vary as the square of the magnetic moment, the deuteron's magnetic scattering will only amount to approximately $\frac{1}{9}$ that of the proton. Hence, in the scattering of electrons from the deuteron, we shall expect to see almost pure charge scattering. This crude expectation is borne out by the result of Jankus⁵⁹ who has shown that the actual elastic scattering from the deuteron, neglecting very small quadrupole terms, is

$$\sigma_D(\theta) = \sigma_{NS} \left\{ 1 + \frac{2}{3} \frac{q^2}{4M^2} [2\mu_D^2 \tan^2 \frac{1}{2}\theta + \mu_D^2] \right\} F_D^2, \quad (41)$$

where σ_{NS} is given, as before, by Eq. (36), (with, of course, the deuteron mass M_D in place of the proton mass M in Eqs. (36) and (37)), μ_D is the static deuteron magnetic moment, and F_D is the form factor obtainable from the deuteron's charge density, as determined from the wave function of the deuteron in its ground state. The second term in the bracket is the magnetic term and its form confirms the remark made above about the small magnetic scattering. The spin of the deuteron is 1 and this accounts for the difference in the coefficient of the q^2 term between Eq. (35) and Eq. (41).

Naturally, if the magnetic moment μ_D is a sum of spreadout moments of the neutron and proton, a form factor will arise and will multiply μ_D . However, just how this modification needs to be made poses a difficult problem. This question has been considered briefly by Jankus⁵⁹ and in more detail by Yennie *et al.*⁵⁷ In any case, it is clear that the magnetic moment effects in the coherent (elastic) scattering from the deuteron will be smaller ($\sim \frac{1}{9}$) than the corresponding scattering from the proton. Further details will be discussed in Secs. Vb and VI.

⁵⁷ Yennie, Lévy, and Ravenhall (to be published).

⁵⁸ L. L. Foldy, Phys. Rev. 87, 688 (1952); 87, 693 (1952).

⁵⁹ V. Z. Jankus, Phys. Rev., to be published.

In the case of breakup of the deuteron, involving inelastic scattering, Jankus also shows that for large momentum transfers

$$\sigma_{D^{\text{in}}}(\theta) = \sigma_{\text{NS}} \left\{ 1 - F_D^2 + \frac{q^2}{4M^2} [2(\mu_p^2 + \mu_n^2 - 3F_D^2) \tan^{2\frac{1}{2}\theta} + \mu_p^2 + \mu_n^2 - 3F_D^2] \right\} \quad (42)$$

or, when F_D is small,

$$\sigma_{D^{\text{in}}}(\theta) = \sigma_{\text{NS}} \left\{ 1 + \frac{q^2}{4M^2} [2(\mu_p^2 + \mu_n^2) \tan^{2\frac{1}{2}\theta} + \mu_p^2 + \mu_n^2] \right\}. \quad (43)$$

In these equations, $\sigma_{D^{\text{in}}}(\theta)$ is the inelastic cross section. μ_p and μ_n are the proton and neutron magnetic moments, respectively, and F_D is the deuteron elastic form factor. When the momentum transfer is large, $F_D \approx 0$. We shall return to Eq. (43) in Sec. VI when we consider actual experiments on the proton and neutron.

It is clear that other spin-bearing nuclei will also show elastic magnetic scattering under the proper conditions. However, it may be expected that magnetic scattering will only be important for light elements with nonzero spins, for example, Li⁷. For a medium or heavy element, the magnetic moment and spin are due to only a few unpaired particles among the many particles which otherwise bear a charge. The magnetic effects reside in the surface and will be associated with a form factor decreasing perhaps even faster than that of charge scattering.

(d) Angular Shapes of Nuclei

Up to now we have discussed only radial variations of charge density in allowing for the effects of finite nuclear size. Actually the spectroscopic literature on quadrupole moments of nuclei and other evidence suggest that those nuclei lying between shell closures (magic number nuclei) should be distorted and not spherical. Nuclei lying close to magic numbers are quite probably very close to a spherical shape. Data obtained in the last few years in experiments on Coulomb excitation by alpha particles and protons give further reason to believe that many nuclei are ellipsoidal in their ground state. The Bohr-Mottelson⁶⁰ model explains this shape in terms of a collective motion of nucleons associating together to produce a traveling bulge moving about the nuclear surface. Such motions correspond to low-lying energy levels called "rotational levels" because of the analogy to rotational states in molecules. Whatever the actual shape of such nuclei, e.g., the rare earths, Ta, W, U, etc., there is little doubt that there is something special about them. The

⁶⁰ A. Bohr and B. R. Mottelson, Kgl. Danske Videnskab. Selskab. Mat.-fys. Medd. **27**, No. 16 (1953).

peculiarities of these nuclei are exhibited also in electron scattering studies. In these studies, the diffraction features seem more washed-out and smoothed than in the case of spherical nuclei such as Pb²⁰⁸ and Au¹⁹⁷.

In interpreting the experimental curves, it is necessary to include the effect of an ellipsoidal shape and to average it appropriately in all the aspects seen by approaching electrons. The averaging has the effect of rounding-off the nuclear surface and making the apparent surface thicker than it actually is. However, the rounding-off does not produce a large change in the scattering mainly because the surface is thick already. In any case, it is not enough to explain the smooth character of the scattering. The fact that low-lying levels exist means that the effects of scattering to these states must also be included: Transitions up to these levels are involved in electron scattering. The one-way transitions from the ground state to the excited rotational levels give rise to inelastic scattering. However, because of the small energy interval between the ground state and the rotational state, such inelastic scattering would be concealed, considering the presently attained resolution in the experiments on scattering. A resolving power of 1 part in 2000 would be required to separate the rotational scattering from the static scattering.

A theoretical treatment of the quadrupole effects on scattering has been given by Schiff⁴⁷ and also by Downs, Ravenhall, and Yennie,⁶¹ for nuclei in the region of tantalum. Further discussion of this work will be postponed until the experimental results are discussed.

IV. EXPERIMENTAL MATTERS

Two independent spectrometer installations have been used in the experiments at Stanford. They will be described separately below:

(a) 190-Mev Apparatus ("Halfway" Station)

Starting at approximately the halfway point along the length of the linear accelerator⁶² and continuing a length of some forty feet paralleling the accelerator, a shielded vault encloses the medium energy (up to 190 Mev) spectrometer and its associated equipment. Figure 14 shows the general layout of the main parts of the equipment. After passing through a brass collimator, a group of accelerated electrons of nearly uniform energy, selected by the uranium or brass slit S , is deflected and dispersed by "Deflecting Magnet C" in Fig. 14.^{3,63} This operation secures a relatively monoenergetic band of electrons which continues on its way into the field of a refocussing magnet "R." The magnet R straightens the beam again to its original direction and refocuses it to a point approximately 9 feet from the end of the magnet R . The principal idea of the

⁶¹ Downs, Ravenhall, and Yennie (to be published).

⁶² Chodorow, Ginzton, Hansen, Kyhl, Neal, Panofsky, and Staff, Rev. Sci. Instr. **26**, 134 (1955).

⁶³ W. K. H. Panofsky and J. A. McIntyre, Rev. Sci. Instr. **25**, 287 (1954).

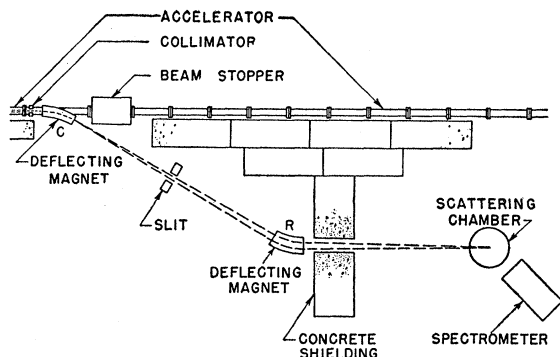


FIG. 14. The general layout of the equipment at the halfway point and the accelerator. Experiments, limited by the spectrometer to 190 Mev, are carried out in this area.

double deflection shown in Fig. 14 is to obtain a gamma-free beam of electrons. The second magnet bends the desired electrons away from the direction in which the large bremsstrahlung beam, produced at slit *S*, travels towards the concrete shield.

The arrangement of Fig. 14 produces vertical focusing at the target. A wedge at the exit face of magnet *R* is used to vary the focus and, thus, to position the spot exactly as desired. A slight curvature of the wedge face also helps to reduce the horizontal spot size. The path of electrons, from the gun of the accelerator all the way to the scattering target, lies in high vacuum. The size of the target spot depends on the size of the collimator opening and is approximately 1 mm high and 3 mm wide with a $\frac{1}{16}$ -inch diameter collimator and 3 mm \times 15 mm for a $\frac{1}{4}$ -inch diameter collimator. Rectangular collimators have been used frequently to make the spot approximately circular and to obtain the maximum intensity for a given spot diameter. The largest spot size used has been $\frac{1}{8}$ inch high and $\frac{3}{8}$ inch wide.

The spot can be observed through a telescope and mirror arrangement focusing on a CsBr(Tl) fluorescent crystal plate one inch square and one millimeter thick. The luminescence produced by the beam appears very clearly on this plate and can be observed at 80 feet even at quite low beam intensities—on the order of 10^6 electrons per pulse (60 pulses per second). CsBr(Tl) is remarkably resistant to the electron radiation, perhaps due to the fact that a large fraction of the impinging energy leaves the crystal in the form of light, instead of remaining as heat or energy causing structural damage.

The beam at the halfway station, focused at the target, has contained as many as two to three times 10^9 electrons per pulse in a band of energy about 2 Mev wide at 188 Mev. Since the accelerator produces pulses at a rate of 60 times a second, this is equivalent to an average current of a few hundredths of a microampere of useful resolved beam. [In the end station (see later) more intense beams are obtained.] This is a powerful beam and permits the measurement of small scattering cross sections.

Unfortunately, the pulsed short-duty-cycle characteristic of this beam is not entirely favorable for the beam lasts only 0.6 microsecond per pulse. Consequently, all the counting must be carried on in this brief period and conventional coincidence techniques become virtually useless. At the same time, there is a huge background of gamma rays and fast neutrons, which make it extremely difficult to operate a scintillation counter [anthracene, NaI(Tl)] without pileup and other unwanted pulses. Nevertheless, there is a good way out of this situation which is solved as follows: (1) a Čerenkov counter is used as the detector, (2) magnetic bending and focusing of the scattered electrons are accomplished so that the detector may be positioned at a point where shielding can be erected about it, (3) through magnetic analysis, portions of the radiation spectrum coming from the target which would interfere with the wanted events are eliminated. These characteristics can be secured by using a magnetic momentum analyzing spectrometer which selects only the scattering events of the desired type, for example, purely elastic events. Other events are separated, and, thus, the counting of electrons of any energy with low background can be achieved. With the experimental arrangement described, a maximum beam, magnet in position of maximum background, closed spectrometer entrance slit, and target in place, the greatest background counting rate is about one pulse in two minutes.

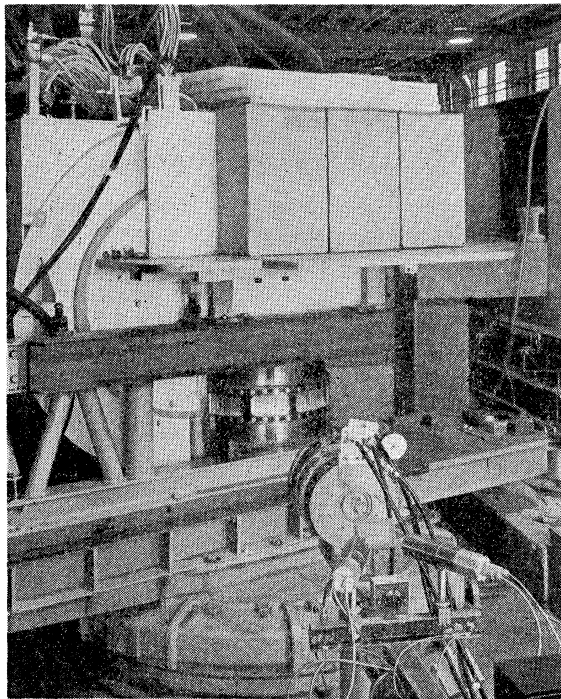


FIG. 15. The semicircular 190-Mev spectrometer, to the left, is shown on the gun mount. The upper platform carries the lead and paraffin shielding that encloses the Čerenkov counter. The brass scattering chamber is shown below with the thin window encircling it. Ion chamber monitors appear in the foreground.

The low background has been achieved with the spectrometer, detector, and shield now to be described. A photograph of the apparatus is given in Fig. 15. It may be seen that while the scattering plane is horizontal, the magnetic spectrometer is vertical. Scattered electrons emerge from the scattering chamber (Fig. 14) in all directions. Some fall within the angular aperture of the entrance slit of the magnetic spectrometer. The entrance slit is made of lead and can be opened to approximately one inch in the horizontal scattering plane or closed to zero. In typical cases it is used at a width of one-half inch. The vertical-slit dimension can be varied and is usually about one inch. The entrance slit is remotely controlled and is attached to the input face of the vacuum chamber of the spectrometer. Electrons enter the thin window (3-6 mils of aluminum) of the magnet chamber situated just behind the slit, and then fall into the magnetic field of the spectrometer where they are analyzed.

The spectrometer is of the double-focusing variety invented by Siegbahn and Svartholm⁶⁴ and modified by Snyder *et al.*⁶⁵ The pertinent details of this particular spectrometer are as follows: The field is inhomogeneous and falls off as $r^{-\frac{1}{2}}$ where r is the radius vector to the orbit trajectory. The mean radius of curvature is 16 inches and the pole faces are six inches wide, thus, stretching from radius 13 to 19 inches. The pole faces extend through a 180° arc and the electrons are bent, therefore, through this angle. A small fringing field extends beyond the input (and exit) slit but the deflection produced here is quite small. The width of the pole gap is 2 inches on the central trajectory and the slope of the pole faces is such that

$$dy/y = dr/2r \quad (44)$$

in order to obtain the required dependence of magnetic field on radius. "y" is the pole gap at any radius. Thus, the pole faces have a linear taper. A lip is machined on the inner and outer edge of the pole in order to prevent the field from falling too quickly to zero.

The magnet itself weighs $2\frac{1}{2}$ tons and is supported by four jacks on an obsolete 40-mm twin antiaircraft gun mount obtained some time ago on loan from the U. S. Navy through the cooperation of the Office of Naval Research. As shown in Fig. 15, a platform has been erected on the magnet to support the heavy shield surrounding the Čerenkov detector. The shield material consists mostly of lead and paraffin and weighs over 2 tons. Buried within the shield is a small Lucite Čerenkov counter built in the form of a truncated cone.

After the 180° deflection and momentum analysis of the electrons in the magnet, they leave the vacuum chamber through a thin window (0.006-inch aluminum) and pass through the horizontal opening in the jaws

⁶⁴ K. Siegbahn and N. Svartholm, Arkiv Mat. Astron. Fysik 33A, No. 21 (1946); N. Svartholm 33A, No. 24 (1946).

⁶⁵ Snyder, Rubin, Fowler, and Lauritsen, Rev. Sci. Instr. 21, 852 (1950).

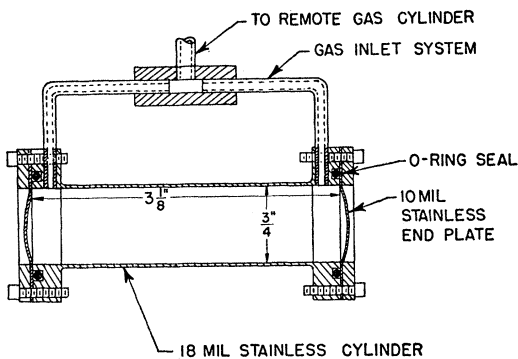


FIG. 16. A typical gas target chamber useful up to pressures of 2000 lb/sq in.

of a uranium slit one inch thick. The jaws of the vertical slit are made of lead and are usually fixed at a width of $\frac{1}{2}$ inch. The horizontal opening of the slit jaws determines the energy limits passed by the spectrometer into the Čerenkov counter and the vertical jaws define the effective width of the target. The dispersion of the instrument is 1.6% per inch at the horizontal slit opening.

The Čerenkov counter is made of highly polished Lucite, four inches long, one inch in diameter at the smaller input end, and 1.5 inch in diameter at the output end. The output end is coupled to a DuMont 6292 photomultiplier. A conical shape of the counter helps the internally reflected light to reach the photo-surface. The Čerenkov counter itself is enclosed in a lead jacket. The combination is placed in a brass tube which is fastened to the photomultiplier cathode follower head and is, thus, a complete optical-electronic unit. The counter is kept in a fixed position behind the exit slit and the shield, platform, and magnet rotate rigidly together on the gun mount. The angular position of the gun mount is controlled remotely and is measured by a combination of high- and low-speed selsyn indicators. No trouble has been experienced in obtaining positional errors smaller than 0.1 degree.

The target is maintained in vacuum in the scattering chamber shown in Figs. 14 and 15. A six-position target frame, built in the form of a vertical ladder, holds the desired scattering foils in place and, since it is remotely controlled, allows changing of the target at will during a run. The angular positions of the target can also be varied remotely.

When it is desired to work with a gas such as hydrogen or helium, a gas target chamber, shown in Fig. 16, is placed inside the bell jar. The bell jar is described in the next paragraph.

As stated previously, the scattering foils or gas target are held in the 20-inch diameter evacuated brass-scattering chamber. A schematic diagram of the scattering geometry is shown in Fig. 17. To keep the scattered electron's path as free of unwanted scattering material as possible, the wall of the scattering chamber is made

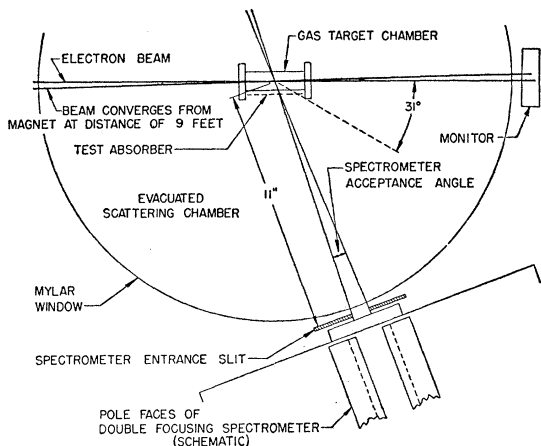


FIG. 17. Schematic diagram of scattering geometry employed with the gas target chamber.

of only 0.006-inch Mylar. This is achieved by holding the Mylar to the thick chamber walls by rubber gaskets. The Mylar window is allowed to stretch into the chamber, as it is pushed there by the force due to atmospheric pressure. The Mylar window extends from -150° to -15° and $+15^\circ$ to $+150^\circ$. The window extends 1.5 inches above and below the scattering plane, corresponding to a total of 3 inches in unobstructed height. In between -15° and $+15^\circ$ there are two brass posts to help hold the top and bottom of the chamber apart against the force of the atmospheric pressure. A 0.006-inch aluminum window occupies the forward region between $\sim -14^\circ$ to $+14^\circ$. Mylar windows were employed in this region also, but usually weakened and collapsed after a few hundred hours of full beam. Aluminum windows appear to hold indefinitely. The scattering chamber, containing the windows referred to, is built in the form of a bell jar and can be detached readily from the base plate. It contains a top port through which foils may be changed without removing the bell jar from the base plates. The base of the scattering chamber contains many well-insulated electrical lead-in connections. There are also provisions for moving monitoring or counting apparatus, inside the bell jar and in vacuum, by means of a large ring gear controlled remotely. At the present time, a secondary electron monitor⁶⁶ is mounted on the ring gear and can be moved into position either behind the scattering target or in front of it. The usual position has been behind the target. The plates of the monitor are large enough ($1\frac{3}{4}$ inches diameter) to contain safely all the beam after it is broadened by multiple scattering in the target. A conventional electronic accumulating charge type of integrator is employed to measure the total number of electrons passing through the foil and monitor. The advantage of the secondary monitor is that it is linear and does not saturate. Unfortunately,

it is useful in a practical sense only for beams larger than about 10^6 electrons per pulse. For smaller beams an ion chamber monitor is used outside the chamber and in the forward multiply-scattered beam. The outside monitor is sketched in Fig. 17.

The counting equipment is simple and consists of a model-501 Elmore amplifier whose pulses are fed to a gated scaler constructed according to a design of J. Narud. The gate can be varied and is usually about 10 or 12 microseconds long. The pulse size, plotted against the discriminator voltage of the gated scaler, shows a good plateau and is obtained before each run. A twenty-channel pulse-height discriminator has been very useful in obtaining the plateau curves. In the energy range over which the Čerenkov counter has been operated, 84–190 Mev, no dependence of pulse height on energy has been observed, and the efficiency is, thus, a constant over this range.

The magnet current is controlled to better than 0.1% by a feedback amplifier, where the input is a voltage taken from a shunt placed in series with the magnet windings. The magnet windings are constructed of hollow-conductor square copper rod $\frac{1}{2}$ inch on a side and water-cooled. Eight hundred amperes can be put through the coils and a maximum magnetic field on the central trajectory of 16 500 gauss has been attained. This field corresponds to approximately 192 Mev. The focusing at this highest energy is not as good as at lower energies (150 Mev) but is still usable. The energy calibration of the magnet has been carried out by (a) knowing the incident energy and placing the magnet in the forward direction, (b) knowing the incident energy and calibrating with hydrogen recoil energies given by Eq. (24), (c) using the known energies of the inelastic scattering from the carbon excited levels, (d) employing a rotating coil fluxmeter halfway along the trajectories, and finally by (e) using magnetic-induction proton-resonance devices. Small differences exist between the various methods, but thus far no experiment has warranted knowing the calibration better than the present differences among them ($\sim 1\%$). Magnetic induction devices are now being installed permanently.

In practice, the method employed in taking data at a given angle consists in (1) setting the magnet current, (2) counting electrons in the Čerenkov counter for a given charge accumulated on the calibrated monitor-condenser, and (3) taking the ratio of these two values. Points such as these are plotted for various values of the magnet current, as measured by the potentiometer reading of the voltage across the magnet shunt. Figure 11 shows typical data obtained in this way. From the elastic peak one may see that the full width at half-maximum is about 0.8 Mev or about 0.4%. Occasionally, with considerable loss of counting rate, 0.2% full width has been observed.

Absolute counting can be carried out approximately

⁶⁶ G. W. Tautfest and H. R. Fechter, Phys. Rev. 96, 35 (1954).

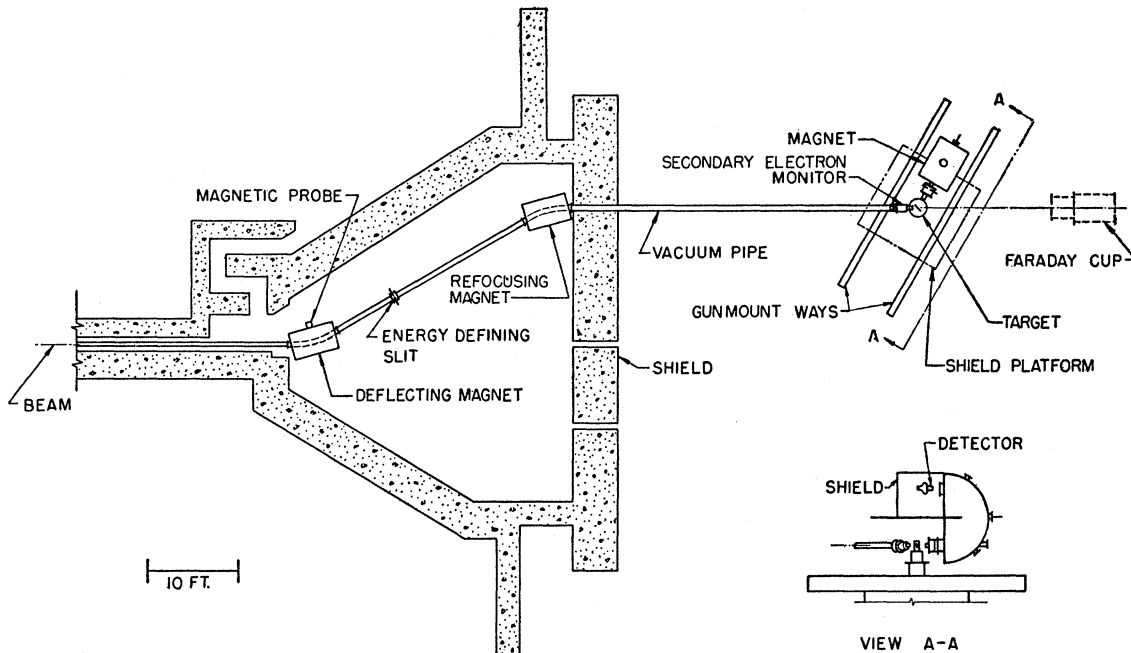


FIG. 18. The experimental installation of the 550-Mev spectrometer.

by using the absolute calibration of the secondary monitor⁶⁶ and the effective solid-angle calculations by Judd.⁶⁷ Accurate absolute counting has not been attempted up to the present time, but semiabsolute standardization has been carried out by measuring the unknown scattering and comparing the results simultaneously with the intensity of electrons scattered from protons. The cross section for scattering from protons may be taken from theory, as corrected by the results of McAllister and Hofstadter.⁴² Provisions are now being made, however, to obtain directly measured absolute cross sections.

(b) 550-Mev Spectrometer ("End Station")

The larger spectrometer (550 Mev) has dimensions scaled up considerably over that of the 190-Mev installation. Otherwise, many of the features of the larger installation are similar to those discussed in Sec. IV(a). It will only be necessary here to give the details where differences are important or where new devices are used such as, e.g., the spectrometer itself.

Figure 18⁶⁸ shows the experimental area where electron scattering studies are carried on. For other details of the end station and accelerator, reference 62 may be consulted. Schematic details of the spectrometer, platform target, monitor, detector, etc. are shown in Fig. 18. A photograph is shown in Fig. 19.

Some details of the larger magnet may be pertinent here. A scale drawing of the magnet and vacuum chamber is shown in Fig. 20. This spectrometer is, like

the smaller spectrometer, a double-focusing 180° modified Siegbahn-Svartholm design. This instrument weighs approximately 30 tones. It is not a scaled-up version of the 16-inch spectrometer. The maximum useful aperture is approximately 0.001 of the entire solid angle. The radius of curvature on the central orbit is 36 inches, and the pole gap at this orbit is 3.0 inches. The pole faces have a linear taper as given by Eq. (44) and a lip is machined on each pole edge. The width of the pole face is 15 inches. The dispersion of

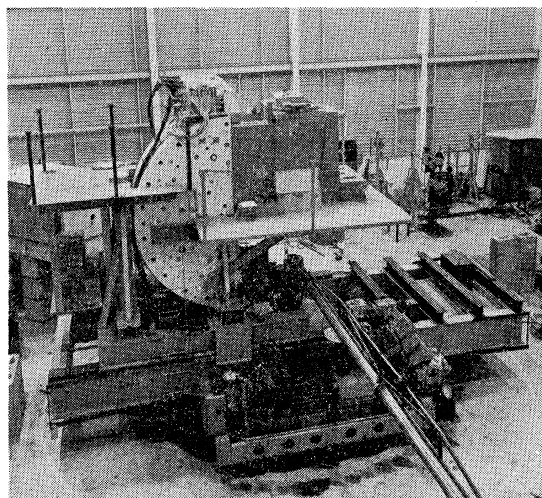


FIG. 19. Photograph of the 550-Mev spectrometer, the gun mount, and shield. The electron beam is brought to the target, shown under the platform, through the vacuum pipe in the foreground.

⁶⁷ D. L. Judd, Rev. Sci. Instr. **21**, 213 (1950).

⁶⁸ E. E. Chambers and R. Hofstadter (to be published).

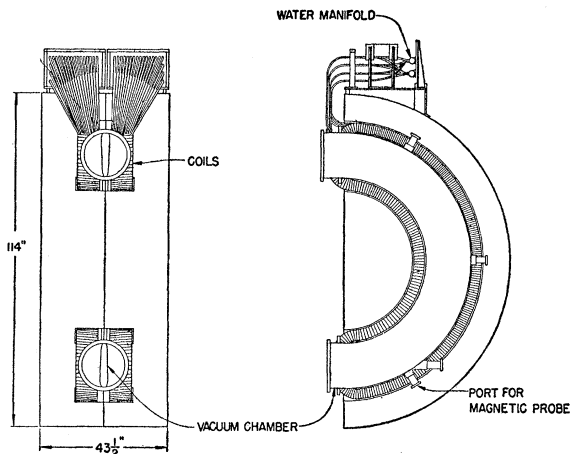


FIG. 20. Scale drawing of the 550-Mev, 36-inch spectrometer, and vacuum chamber.

this spectrometer is 0.75% per inch. On the central trajectory a maximum field of 20 000 gauss has been obtained, although the magnet is not often used at this high value because of saturation at the pole edges and other places in the gap. Although the cross-sectional area between the poles is 15 inches \times 3 inches, the full area has not been used, because of the presence of a thick-walled bronze vacuum chamber. The internal free dimensions have been reduced to 14 inches \times 2 inches by this chamber.

Passing through the outer yoke, as shown in Fig. 20, are three radial holes, each 4 inches in diameter. There are similar but smaller connecting holes in the vacuum chamber. These are used to allow the insertion of radial probes for magnetic measurements. At the 30° and 120° ports, the field has been observed to be 2% smaller than in the 90° hole at the center of the magnet. A magnetization curve for the spectrometer is given in Fig. 21 and shows that the field is proportional to the current up to 14 000 gauss (or up to 400 Mev). The region in which the field falls off as the square root of r lies between radii 33.5 and 38.5 inches and at higher fields it contracts so that it is only two inches wide at 550 Mev. At high fields the vertical aperture is, therefore, stopped down at the entrance slit to prevent electrons from entering the saturated region of the gap. The fringing field has been measured and is virtually negligible for all energies. A fourth hole, shown in Fig. 20, permits a bremsstrahlung beam to pass through the vacuum chamber and through a thin window from the target while all electrons and positrons are cleared out of the way by the magnetic field. Further constructional details are given in reference 68.

The poor duty cycle makes it necessary to use a massive ten-ton shield to protect the Čerenkov counter from background radiation. This shield is supported high above floor level on a platform on the magnet itself. The magnet, platform, and shield can be moved

radially on the two ways shown in Fig. 18. The magnet is supported on a modified double five-inch antiaircraft gun mount kindly provided on loan by the U. S. Navy. Remote control of the gun mount to 0.05 degree has been obtained with the standard selsyn indicators provided in the mount.

The Čerenkov detector is much like the smaller one described previously, but its dimensions are increased. Its input diameter is 2.75 inches, output diameter 3.75 inches, and the length is 5.0 inches. The truncated cone of Lucite couples to a DuMont five-inch photomultiplier. The slit system used with this detector resembles that of the smaller spectrometer.

The beam spot at the target position is usually about $\frac{3}{8}$ inch wide and $\frac{1}{8}$ inch to $\frac{1}{4}$ inch high. Under certain conditions it can be made considerably smaller. Gas target chambers of the kind shown in Fig. 16 have been used in this installation. The length of the gas target is increased so that small-angle studies can be made with less interference from the end windows than the small chambers allow. A ten-place target ladder is used with the larger spectrometer for foils and solid laminas. A snout-like extension of the vacuum chamber extends from the spectrometer near to the target so that only a few inches of air lie between the scatterer and the thin-windowed input port of the spectrometer. Figure 22 shows some of the details. Nevertheless, electrons scattered from this air layer have been detected and in a short time all experiments in the end station will be carried out in vacuum with a bell jar, as in the halfway station.

Finally Fig. 18 shows a large Faraday cup, which is now being installed and which will be used to make absolute measurements of cross section.

(c) Behavior of Čerenkov Detectors

While carrying on studies of the neutron,⁵⁰ (see later, Sec. VI) for which scattering targets of CH_2 and CD_2

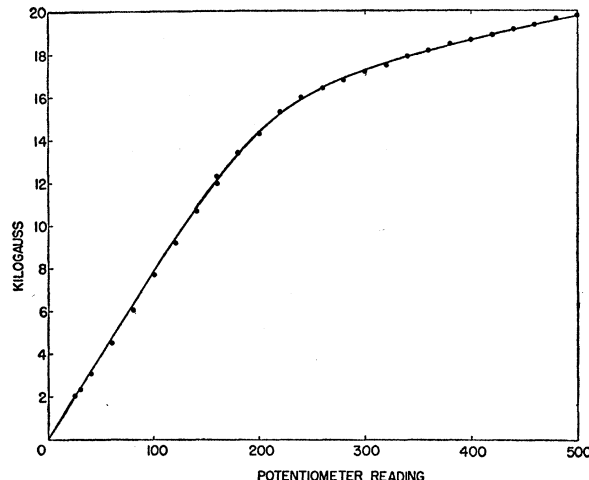


FIG. 21. Magnetization curve for the 550-Mev spectrometer. The potentiometer reading is proportional to the current in the magnet coils.

are used, a peculiar behavior was noted at high energies and large angles. Figure 23 shows the observed pattern at 120° and 550 Mev and is typical of the findings. Note the customary sharp free proton peak at a potentiometer setting of 127. In addition to this peak, very large peaks are observed in the energy spectra of CH_2 and CD_2 , centering at a reading of 90 on the potentiometer. There is a slight bulge in CD_2 near the position of the free proton peak. The bulge (Sec. VI) was the object under study, but it was completely masked by the large peaks noted above. An investigation, which will not be reported here, showed that the large peaks were due to negative pions produced in the target and carrying the same momenta as scattered electrons under investigation. Under careful investigation, the left side of the peaks turned out to be exceedingly sharp and corresponded exactly to the threshold velocity of pions required to first register a pulse in a Lucite (index of refraction $n=1.50$) Čerenkov detector. When the Lucite was replaced by the liquid $\text{C}_8\text{F}_{16}\text{O}$ (index 1.276), the pion peaks disappeared almost completely and the deuteron bulge could be seen clearly. It is, thus, quite advantageous to use a material with the smallest possible index of refraction when it is desired to isolate electrons. Of course, the index must be larger than unity or no light will be observed. A gaseous Čerenkov detector could have important uses in this instance.

In Fig. 13 the step near 175 Mev represents a pion background even for the smaller incident energy of 400 Mev.

V. RESULTS

The results obtained in investigating atomic nuclei with the two instruments described in this paper will be discussed below in the order of increasing atomic number. *Note:* Often the rms radius of an "equivalent uniform model" is mentioned in the text. This refers to a radius found from r_0 defined by Eq. (52).

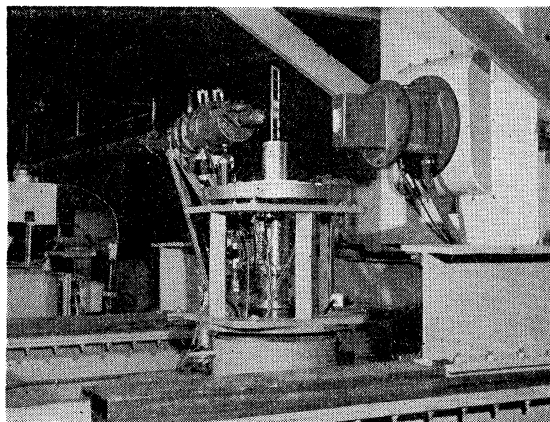


FIG. 22. Details of the monitor, target ladder, and magnet input port.

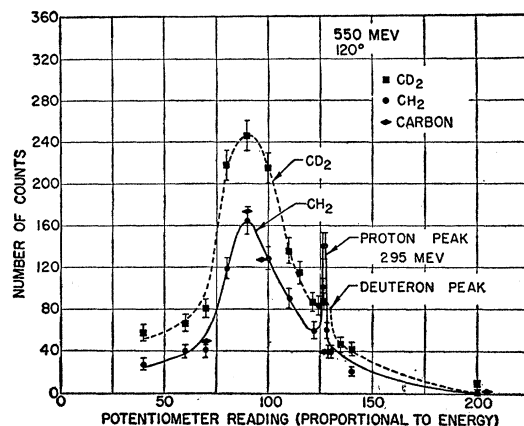


FIG. 23. The free proton peak, the deuteron incoherent peak, and the negative pion peaks. The first two peaks are associated with scattered electrons, the remaining three (CH_2 , CD_2 , C) are caused by negative pions having the same momenta as electrons scattered inelastically in this momentum range. See also Sec. VI.

(a) The Proton

Electron scattering from the proton has been investigated at energies extending from 100 Mev up to an energy of 550 Mev. Hydrogen gas at high pressure (2000 psi) has been used at energies of 100, 188, 210, 236 Mev by McAllister and Hofstadter.⁴² The earliest experimental results showed departures from the point-charge-point magnetic-moment calculations of Rosenbluth,⁵⁶ Eq. (35). The data are shown at 188 Mev in Fig. 24. The topmost curve (c) is the Rosenbluth curve for a point charge and point magnetic moment, where the magnetic moment has the full anomalous value, $1+\mu=2.79$ nuclear magnetons. The lowest curve (a) corresponds to no magnetic moment at all and is, therefore, the Mott curve, Eq. (36), in the laboratory system's coordinates. The large interval between curves (c) and (a) demonstrates the theoretical contribution of the magnetic scattering of a point. Curve (b) is Rosenbluth's cross section if the magnetic moment of the proton had a pure Dirac moment, i.e., the 1 of the $1+\mu$ nuclear magnetons. The experimental points shown in the figure lie in between the Dirac curve and the point charge point moment curve and, therefore suggest that the proton's magnetic moment is not a point and that form factors must be assigned to the proton.

Without further information, there is no way of deciding *a priori*, whether F_1 or F_2 , the Dirac or Pauli form factors of Eq. (39), respectively, are separately responsible for the smaller amount of backward scattering in Fig. 24, or whether both together share in the responsibility. However, Eq. (39) shows that F_1 and F_2 produce different angular distributions. For example, it can be shown that a point charge ($F_1=1$) and a spread-out Pauli moment ($F_2<1$) will result in a form factor that is nearly unity at small momentum transfers ($q<1$) and will begin to fall off more rapidly at larger momentum transfers. On the other hand, a spread-out

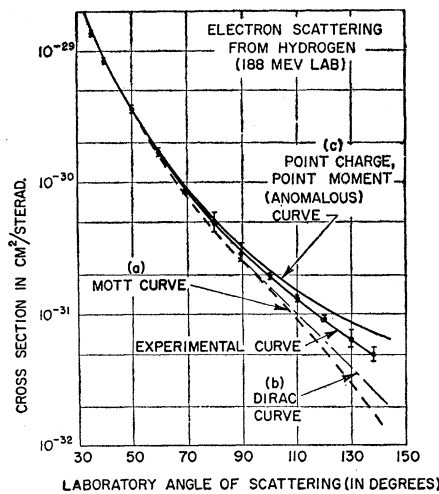


FIG. 24. Electron scattering from the proton at an incident energy of 188 Mev. The experimental points lie below the point-charge point-moment curve of Rosenbluth, indicating finite size effects.

charge ($F_1 < 1$) and a point Pauli moment ($F_2 = 1$) will show weaker scattering at small values of q and will show almost the entire amount of Rosenbluth point scattering at large momentum transfers. This is another way of saying qualitatively that the charge is responsible for small-angle low-energy scattering and the Pauli-magnetic moment is responsible for most of the large-angle high-energy scattering. It must be remembered that even if F_2 is zero there is a contribution to magnetic scattering from F_1 , namely, from the Dirac moment. However, the effect from F_2 is larger. A spread-out charge ($F_1 < 1$) and a spread-out moment ($F_2 < 1$) will produce a weakening of the scattering at both small and large values of q . Hence, in principle, by studying the scattering over a large range of energies and angles, it should be possible to disentangle the separate contributions of F_1 and F_2 .

The proton results were, therefore, analyzed at the energies 100, 188, 210, 236 Mev with choices of (1) point-charge ($F_1=1$) spread-out moment ($F < 1$), (2) point-moment ($F_2=1$) spread-out charge ($F_1 < 1$), and (3) both spread-out ($F_1 < 1$, $F_2 < 1$).

It should be noticed that at the lower energies (q small), only the mean square radii can influence the form factor, as shown by Eq. (19). Hence, the determination of F_1 and F_2 at energies less than 200 Mev will determine a radius r_e for the Dirac cloud and a radius r_m for the Pauli meson cloud, and not the shape of either of these distributions as a function of radius. The analysis showed further that $r_e = r_m = 0.74 \pm 0.24$ fermi where r_e and r_m are the radii associated with the Dirac and Pauli parts of the proton's charge and magnetic moment density distributions. These values of r_e and r_m fitted the data excellently at all energies. The solid line in Fig. 24 shows the theoretical curve for

$r_e = r_m = 0.70$ fermi, i.e., the foregoing choice (3), and is one particular example of the fit to the experimental data. The accuracy of the experimental points was not great enough to decide definitely that the other possible choices (1) and (2) could be eliminated.

The same type of experiment was, therefore, continued by Chambers and Hofstadter⁶⁸ between energies of 200 Mev and 550 Mev in the laboratory frame. Data were obtained in these cases with polyethylene (CH_2). Brief check data with hydrogen gas were also obtained at the single energy of 400 Mev. An elastic peak, showing electrons scattered against protons in polyethylene at 400 Mev and 60° , is plotted in Fig. 25. Because of the recoil of the proton, the electron carries off only an energy of 326 Mev at 60° . The area under the proton peak is the quantity measured in this experiment and is proportional to the differential cross section⁶⁹ for scattering at this laboratory angle. In obtaining this area, the carbon background is subtracted and the low energy side of the peak is extended as indicated by the dashed line AC in Fig. 25. When the proton peak areas are normalized by the monitor reading to unit incident electron, the cross sections at various angles may be compared. A typical curve is shown in Fig. 26; the experimental points at 400 Mev are indicated with their corresponding limits of error. Plotted as a solid line above the experimental curve is the Rosenbluth theoretical curve [Eq. (35)] for a point charge and point magnetic moment. This is indicated by the symbols $r_e = 0$ and $r_m = 0$ standing, respectively, for rms charge radius (Dirac) and moment radius (Pauli).

At the high energies used in these experiments (200, 300, 400, 500, 550 Mev) quantities higher than the second power of qa enter Eq. (19) and the shapes of the charge and moment distributions become important.

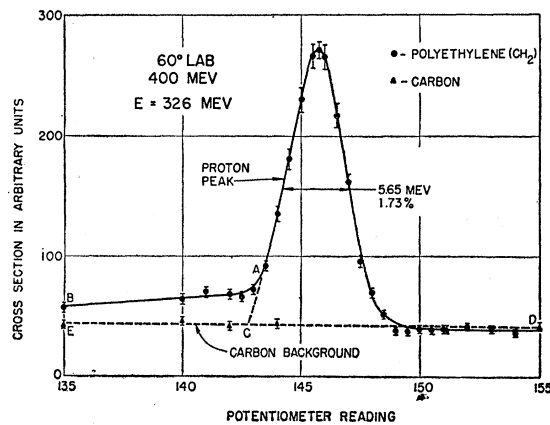


FIG. 25. Elastic scattering of 400-Mev electrons from protons in polyethylene at a laboratory angle of 60° .

⁶⁸ Since a constant slit width was used in all the experiments, there is a well-known correction in beta spectroscopy that must be applied to the areas because of the dispersion of the instrument (constant dp/p). This correction has been made in a standard manner to all cross sections.

Furthermore, the same distribution must fit the data at all energies if the particular model and the interpretation given by Eq. (39) are correct. Without going into details at this point the fit of one particular model is shown in Fig. 26. In this case, the model is the exponential distribution for both charge density and magnetic moment density. The rms radius of each distribution is taken as 0.80 fermi. From Eq. (39) and the F_1 and F_2 obtained from row IV in Table I, a theoretical curve can be prepared for this particular model. This theoretical curve is indicated by the solid line passing through the experimental points in Fig. 26. The experimental points can be moved upwards or downwards to make the best fit. No other adjustment is made. This procedure is necessary since absolute values are not known. The ratio of the experimental values (now normalized in an absolute way by the fit at smaller angles) to the point-charge point-moment values are the desired F^2 (form factor)² values. Independent fits of the experimental data were made at all the energies between 200 and 550 Mev and then assembled together in Fig. 27. The ordinate in this figure is F^2 as just described. The abscissa is the square of the momentum transfer $\times 10^{-26} \text{ cm}^2$. The fit of this particular model is good and it is consistent at all energies and angles.

The consistency of the fit under these diverse conditions lends confidence to the use of Eq. (39) and the phenomenological introduction of the F_1 and F_2 form factors. The good fit to the experimental data is not

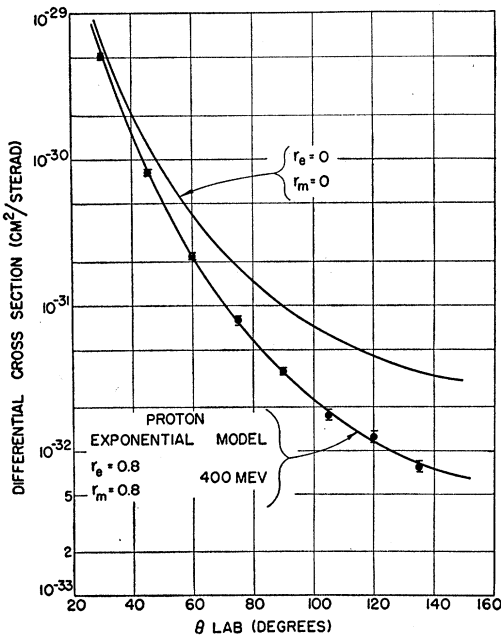


FIG. 26. Typical angular distribution for elastic scattering of 400-Mev electrons against protons. The solid line is a theoretical curve for a proton of finite extent. The model providing the theoretical curve is an exponential with rms radii= 0.80×10^{-13} cm.

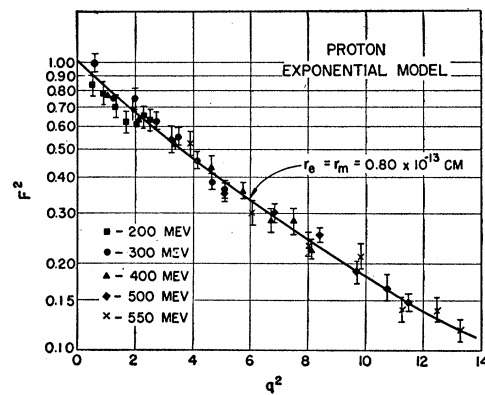


FIG. 27. The square of the form factor plotted against q^2 . q^2 is given in units of 10^{-26} cm^2 . The solid line is calculated for the exponential model with rms radii= 0.80×10^{-13} cm.

unique, however. A Gaussian model with $r_e=r_m=0.72$ fermi provides a similar fit and equally good consistency at all energies. Many other models have been studied in this way. Among those examined are II through X, inclusive, in Table I. With all these models the choice $r_e=r_m$ was made and the shapes were assumed to be the same for the charge (Dirac) cloud and the magnetic moment (Pauli) cloud. The best choices are shown in Table II. All other models do not fit well enough at all energies to be considered seriously.

Several of the models are shown in Fig. 28. In this figure $4\pi r^2 \rho$ is plotted. This is a quantity proportional to the amount of charge in a shell at radius r . Either one among the Gaussian, exponential, or "hollow" exponential models fits equally well. Any model, lying within a band in Fig. 28 including all the three models, represents a "best" present approximation to the charge distribution within the proton. The magnetic moment density distribution has the same appearance. The Yukawa model, also shown in the figure, will not fit the data. Neither will a uniform model.

All models considered above have involved the assumption of similar shapes and equal radii for the Dirac and Pauli charge and moment clouds. If differences among these shapes are assumed and F_1 is not to be the same as F_2 , the field of possible models is enlarged enormously. Considerable effort has been expended in attempts to find pairs of different radii and different shapes which could match the experimental data. Many

TABLE II. This table represents a summary of the proton models and the appropriate values of their root-mean-square radii which give the best fits to the data. Equal radii for Dirac and Pauli clouds are assumed.

Model number	Shape	rms radius for best fit ($r_e=r_m$) in fermi units
III	$\exp(-r^2)$	0.72 ± 0.05
IV	e^{-r}	0.80 ± 0.05
VI	$r e^{-r}$	0.78 ± 0.05
VII	$r^2 e^{-r}$	0.75 ± 0.05
Mean (best fit)	...	0.77 ± 0.10

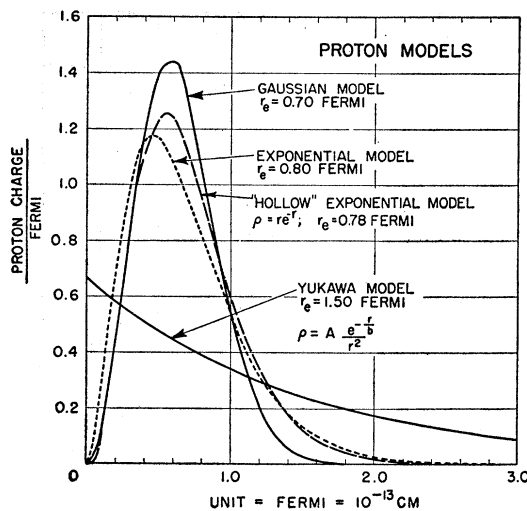


FIG. 28. The Gaussian, exponential, and "hollow" exponential models fit the proton data equally well. The Yukawa model will not fit. The ordinate is $4\pi r^2 \rho$.

possibilities have been eliminated. A single example is shown in Fig. 29 and shows a typical behavior observed for a choice of a magnetic cloud of small dimensions. It is not possible to make a realistic F_2 correspond to a small radius.

Without going into details it is possible to summarize the model testing by saying that if different radii are chosen for the Dirac and Pauli clouds, the limits on each *independently* lie approximately at 0.6 and 1.5 fermi units. Higher accuracy of the experiments can reduce these limits and can also decide between the models shown in Fig. 28. The experiments have the least accuracy in determining the region near zero radius and perhaps as far as 0.3 fermi. Among all the models tested the "hollow" exponential model with $r_e = r_m = 0.78$ fermi gives the best fit. This does not mean that $\rho = 0$ at $r = 0$ since, as has just been remarked, there is only a small accuracy at $r = 0$.

The interpretation of these experiments on the proton is also considered in Secs. VII and VIII. It is interesting, however, that the proton's "Dirac size" (r_e) seems to be just as large as the "Pauli size" (r_m), and is very large, indeed, being about three times the nucleon Compton wavelength. We call attention once more to the fact that the apparent finite size effects can be explained equivalently with point particles and a breakdown of electrodynamics.

(b) The Deuteron

Elastic scattering from the deuteron was investigated at high energies (192 Mev) by McIntyre and Hofstadter,⁷⁰ and recently in considerably greater detail at 188 Mev and 400 Mev by McIntyre.⁷¹ The interest in the deuteron is manifest since it is the only two-

nucleon system which is known to be stable and, in some respects, its position as a tool in resolving the problem of nuclear forces resembles that of the hydrogen atom in atomic physics. Because of this simplicity, the deuteron wave function in the ground state can be calculated for many possible nuclear potentials acting between the neutron and the proton. Among these are the square well, Hulthén, Blatt-Kalos, Gartenhaus, and the repulsive core potentials. It is well known that all give virtually the same behavior if adjusted for the proper binding energy of the deuteron, $\epsilon = -2.226$ Mev and the triplet scattering length. All that can be determined from the nuclear experiments is the effective range, a quantity essentially independent of the shape of the deuteron potential at the scattering energies investigated. In studying the deuteron it was hoped that electron scattering might cast a new and independent light on the neutron-proton potential.

From the deuteron wave function $\psi(r_{12})$ and the accepted value of the effective range 1.70 ± 0.03 fermi, the charge density in the deuteron can be computed from $\rho = e|\psi|^2$, where r_{12} is the internucleon distance. For a given potential, and, therefore, a given charge density ρ , the form factor for the deuteron F_D [see Eq. (41)] can be computed. Now, the electron scattering method also furnishes an independent value of the experimental form factor. Hence, the prediction of nuclear theory can be compared with the experimental electron scattering result. Such a comparison is given in Fig. 30 for three different potentials.

Experimentally, the data can be taken with deu-

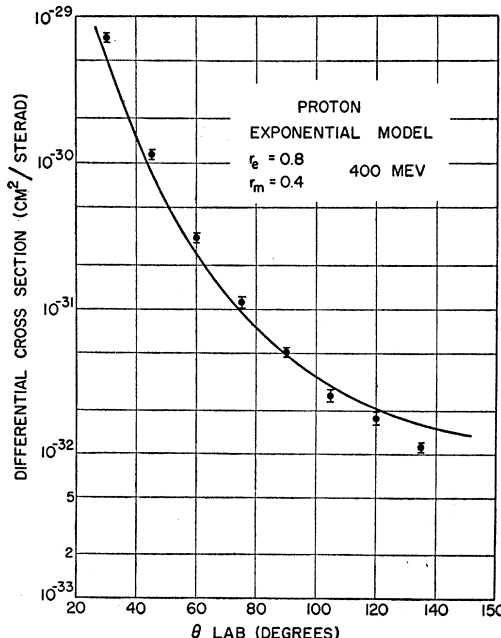


FIG. 29. Example of a model that will not fit the experiments. This model has a magnetic moment distribution which is too small.

⁷⁰ J. A. McIntyre and R. Hofstadter, Phys. Rev. **98**, 158 (1955).

⁷¹ J. A. McIntyre (to be published).

terium and hydrogen alternately in the gas target chamber and, thus, the deuterium data can be normalized to hydrogen. This is an important point since a vital calibration datum is furnished by the result of the proton experiment.

From the figure, it is evident that the actual scattering lies outside the limits of any of the theoretical curves and it is apparent that an additional form factor is needed to obtain agreement. When it is realized that the deuteron's charge density $e|\psi|^2$ has been computed as if the neutron and proton were points, it may not seem so surprising that agreement with experiment is unattainable in Fig. 30. As we have remarked in IIIc, the question of how to introduce this form factor requires great care and involves considerations that concern both the meson clouds surrounding the neutron and proton and also the Dirac "cores" in these particles.

Agreement in Fig. 30 can, of course, be achieved by increasing the effective range. This requires an increase from 1.70 to at least 2.2 fermis and appears to be outside the limit of permissible errors (± 0.03 fermi) in the effective range. On the other hand, McIntyre obtains excellent agreement with experiment by empirically using a finite Gaussian proton of rms radius $r_e = 0.80$ fermi with the repulsive core potential of Jankus.⁵⁹ Figure 31 shows the agreement for three proton radii. The consistency of this analysis with that of the proton⁶⁸ is remarkable. Similar agreement with slightly larger radii (0.85 fermi) are obtained with other potentials such as the Hulthén type.

We have noted before that the introduction of nucleon form factors due to finite size effects in the neutron and proton, must be considered carefully from a meson theoretic point of view. Naively we should expect that a finite proton's form factor would multiply F_D directly where F_D is the deuteron form factor. Actually, the finite size of the neutron also should contribute. Since the specific electron-neutron interaction

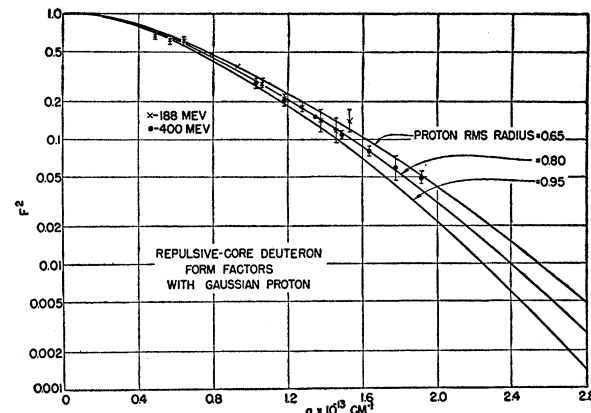


FIG. 31. Introduction of a finite proton core allows the experimental data to be fitted with conventional form factors (McIntyre).

has been shown to be very small, the neutron's apparent size can be assumed to be very small. (See Sec. VI and reference 90.) In this event only the proton's finite size would be important. However, the situation is more complicated and is the subject of an investigation by Yennie *et al.*⁵⁷ These authors show that, for the deuteron, a finite negative meson cloud in the neutron should cancel the proton's positive meson cloud, leaving as residue only the effect of the cores of the proton and neutron. While, it might be expected that the cores would be very small, it seems necessary to introduce an appreciable nucleon size to interpret the deuteron experiment. This is an indication that the nucleon core size is quite large (0.7 fermi).

Inelastic scattering from the deuteron has been discussed in Sec. IIIc and will be taken up again in the consideration of the size of the neutron (Sec. VI).

(c) The Alpha Particle

Scattering from the alpha particle in helium gas has been carried out by McAllister and Hofstadter⁴² at 188 Mev and by Blankenbecler and Hofstadter⁴⁹ at 400 Mev. Both experiments agree quite well with each other and show that there are very large effects due to the finite size of the alpha particle. Since the spin and magnetic moment of the alpha particle are both zero, the elastic scattering is due entirely to the charge alone. However, the large angle *inelastic* scattering will depend significantly on the magnetic moments of the nucleons.

Figure 32 shows the experimental data in helium gas at approximately 1500 psi. The gas target chamber was alternately filled with helium and hydrogen at certain angular settings. The scattered intensities were measured under the same experimental conditions. Hence, the helium data can be normalized to proton scattering and a Mott curve Eq. (36) can be constructed for helium. The solid line in Fig. 32, labeled "Theoretical Mott Curve," has been prepared in this way. Figure 33 shows that beyond 70° the elastic scat-

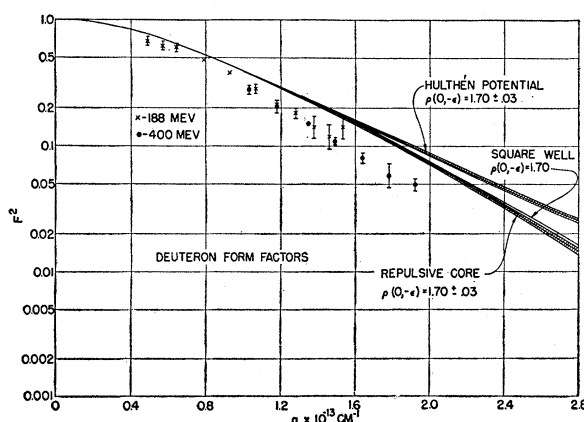


FIG. 30. The experimental data of McIntyre⁷¹ at 400 Mev. The ordinate is the square of the form factor. Conventional form factors, derived from well-known nuclear potentials, do not fit the experimental data.

tering is smaller by a factor of over a hundred from that expected from a point alpha particle. This figure exhibits the square of the form factor as a function of laboratory angle obtained from the data in Fig. 32. The points carrying limits of error are the experimental points and the three solid curves represent three theoretical form factor curves for possible models of the alpha particle of the indicated rms radii. It is clear that the Gaussian with rms radius 1.61 fermi is the best fit of the three. This radius is in close agreement with one previously obtained.⁴² No attempt is made here to introduce the finite sizes of the nucleons although, when the data are compared ultimately with a form factor calculated from a nuclear theory of the alpha particle, the finite size effects must be taken into account.

One brief study, needing repetition, was attempted by Blankenbecler and Hofstadter⁴³ to examine the inelastic continuum in helium at a large q value: 400 Mev, 60° . The results are shown in Fig. 13 and have been commented on briefly in Secs. IIIb2 and IIIb4. The incoherent scattering from the protons and neutrons in the alpha particle add up to a considerably greater cross section than the coherent scattering, represented by the elastic peak at 373 Mev. As far as is known to the author, there is no explicit theory giving the momentum distribution of the nucleons in the alpha particle for comparison with the inelastic continuum of Fig. 13.

The size of the alpha particle *can* be compared with the radius, 1.61 fermi, given by the phenomenological

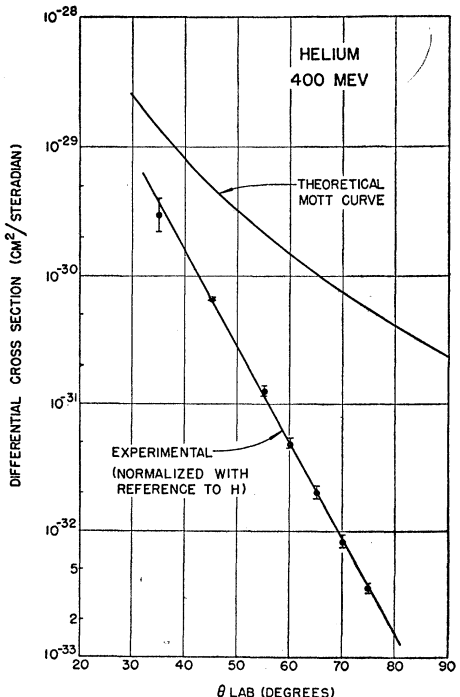


FIG. 32. Experimental angular distribution of 400-Mev electrons scattered from helium gas. The point charge curve is shown here.

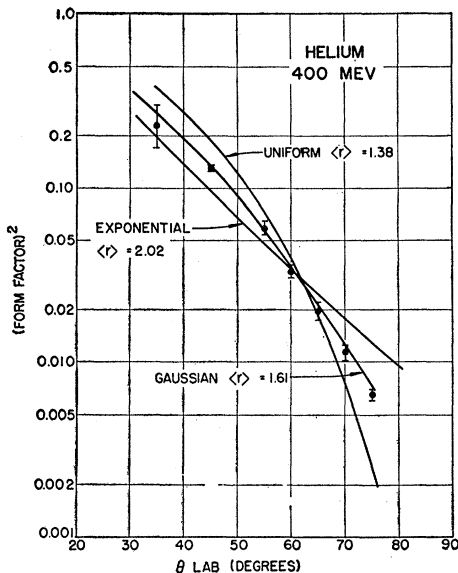


FIG. 33. The square of the form factor of the alpha particle for three possible models. The experimental points indicate that a Gaussian model with rms radius $= 1.61 \times 10^{-13}$ cm provides the best fit.

analysis of Fig. 33 for the best-fitting Gaussian model. To make this comparison Dalitz and Ravenhall⁷² computed an rms radius from the wave functions of Clark⁷³ who used a variational method to fit the binding energy of the alpha particle. The resulting radius was only about $\frac{2}{3}$ of the required size. Perhaps this discrepancy is due to the use of only two D states in Clark's calculations.

It may be noticed that there is an apparent peak in Fig. 13 at 352 Mev and perhaps other structure in the immediate neighborhood of the high-energy side of the inelastic continuum. Whether this points to an excited state of the alpha particle is difficult to say with the meager evidence at hand. This work needs early repetition to decide whether such structure is real or not.

(d) Lithium and Beryllium

The separate isotopes Li⁶ and Li⁷ have been studied by J. F. Streib⁷⁴ who finds that both nuclei appear to have the same rms radius to within a few percent. Both isotopes possess charge densities resembling closely model XII of Table I. The best type of fit to the elastic scattering was found by Streib⁷⁵ to be model XII with rms radii "a" (Li⁶) = 2.78 fermi and "a" (Li⁷) = 2.71 fermi with an accuracy of $\pm 2\%$. The ratio (a Li⁶/ a (Li⁷)) could be measured quite carefully and more accurately than either size, and gave the value 1.026 ± 0.008 . The effects of the magnetic moment of Li⁷ were calculated

⁷² R. H. Dalitz and D. G. Ravenhall (private communication).

⁷³ A. C. Clark, Proc. Phys. Soc. (London) A67, 323 (1954).

⁷⁴ J. F. Streib, Phys. Rev. 100, 1797(A) (1955).

⁷⁵ J. F. Streib (private communication). These are results more recent than those given in reference 74. The sizes were based on a comparison with scattering from the proton.

with a Rosenbluth-like formula [Eq. (35)] and were removed in arriving at the above values of nuclear radii. It is interesting that Li^7 appears to have a smaller size than Li^6 . This may be because the Li^6 nucleus behaves in some respects as if it had a deuteron outside its closed shell. For Li^6 , the value of r_0 is 1.98 fermis and for Li^7 , 1.83 fermis, for the equivalent uniform model [Eq. (1)].

In the case of Be^9 , an early study⁴⁴ showed that inelastic scattering to nuclear levels was quite prominent. The inelastic and elastic scattering have been studied again more intensively by Streib⁷⁵ who finds good agreement with the older results. Streib has analyzed the beryllium results, using model XII of Table I, which is a modified exponential charge distribution and finds an rms radius of 3.04 ± 0.07 fermis. This corresponds to an r_0 of 1.89 fermis, for an equivalent uniform model.

Shell model calculations of p -shell nuclei have been carried out by Ferrell and Visscher⁷⁶ who find that the nucleus Li^6 should have an rms radius of 2.8 fermis. This is in good agreement with Streib's value of 2.78 fermis. The experimental value of Li^7 (2.71 fermis) is higher than the theoretical value 2.3 ± 0.2 fermis, and the experimental radius of Be^9 (3.04 fermis) is likewise larger than the theoretical value of 2.3 ± 0.2 fermis.

(e) Carbon

C^{12} is a relatively simple nucleus and it is important that it should be investigated thoroughly. This nucleus has been examined by Fregeau and Hofstadter⁴⁵ and subsequently by Fregeau⁷⁷ in considerably greater detail. In Sec. IIIb1 we have illustrated the type of

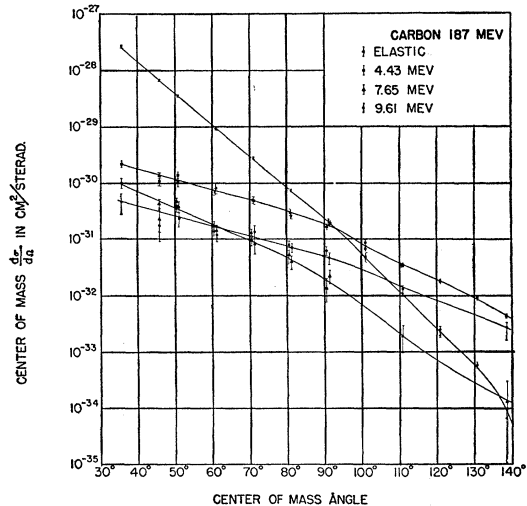


FIG. 34. Fregeau's data on the elastic and inelastic scattering of 187-Mev electrons as a function of center-of-mass angle.

⁷⁶ R. A. Ferrell and W. M. Visscher, Bull. Am. Phys. Soc. Ser. II, 1, 17 (1956).

⁷⁷ J. H. Fregeau, Ph.D. thesis, Stanford University, June, 1956. A shorter account is to be published.

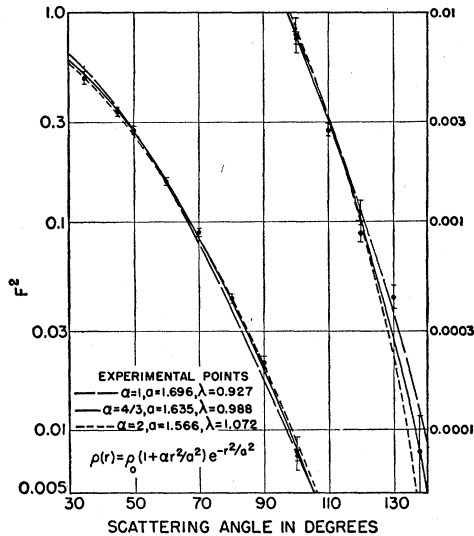


FIG. 35. The square of the form factor for C^{12} . Theoretical curves for Model XI of Table I, corresponding to Eq. (45), are shown in the figure. The parameter λ is a normalizing factor which should be unity if the theory and experiment fit exactly. The value $\lambda = 0.988$ for $\alpha = 4/3$ is very satisfactory.

data taken at a given scattering angle with this nucleus and have seen there not only the elastic peak, but the scattering due to the various levels of C^{12} . A summary of the data obtained at 187 Mev up to the present time is shown in Fig. 34. The graph includes the behavior of the elastic peak which shows a variation with scattering angle of about a factor 2×10^6 from 35° to 138° . The figure also shows the angular behavior of the scattering cross sections associated with the excited states of C^{12} at 4.43, 7.65, and 9.61 Mev. At the largest angles the elastic scattering is exceeded by the scattering from each of the nuclear levels. Angular distributions of the 4.43- and 9.61-Mev scattering cross sections appear to be similar to each other and less steep than the behavior of the elastic or 7.65-Mev peaks. Since the 4.43-Mev transition is a $0^+ - 2^+$ transition and the 7.65 Mev is believed to be a $0^+ - 0^+$ transition, the difference in angular behavior may be correlated with the radial oscillations of the $0^- - 0^-$ transition. On the basis of an angular behavior similar to that of the 4.43 transition, the 9.61-Mev transition might be thought to be $0^+ - 2^+$.

The elastic scattering leads to a determination of the radial charge density in the ground state of C^{12} . It is possible to compare the carbon scattering, directly in the experiment, with scattering from the proton and, hence, to obtain an "absolute" determination of the experimental form factor. In the early work⁴³ a comparison of an "absolute" form factor with those obtained from three trial models, i.e., the Gaussian, uniform, and exponential, led to a best fit lying between a Gaussian with rms radius 2.47 fermis and a uniform model with rms radius 2.20 fermis. This suggested a "best" value of 2.40 fermis for the rms radius. A con-

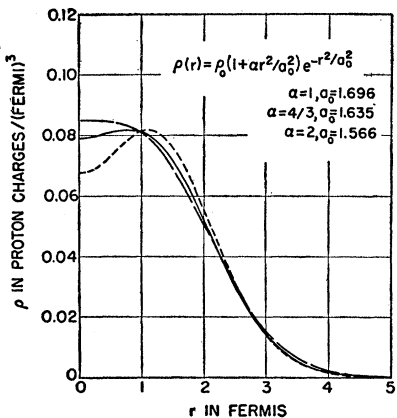


FIG. 36. The charge distribution for Model XI for three values of α . All three charge distributions fit the experimental data equivalently. $\alpha=4/3$ has some theoretical justification.

siderably better determination has been made recently by Fregeau⁷⁷ who finds excellent agreement with this conclusion

Fregeau's results are shown in Fig. 35 which gives F^2 as a function of angle for three models of a type suggested by Ravenhall,⁷⁸ and more recently by Morpurgo,⁷⁹ based on the oscillator shell model. (See also Model XI and Table I.) On this model the charge density ρ has the same behavior for JJ and LS coupling and has the appearance

$$\rho = \rho_0 \left(1 + \frac{r^2}{a_0^2} \right) \exp[-(r^2/a_0^2)], \quad (45)$$

where

$$\alpha = 4/3 \quad (46)$$

for the shell model and "a₀" is a parameter proportional to the rms value of the radius. α may be varied to find a best fit, as indicated in Fig. 35. It appears that $\alpha=4/3$ is as good a fit as can be obtained. Figures 36 and 37 show the charge distribution ρ , given by Eq. (45), for three values of α , and also $4\pi r^2 \rho$, for these same values. The solid line shows the case $\alpha=4/3$. With present accuracy it has not been possible to determine the exact behavior of ρ near $r=0$, but the charge density at larger values of radius is rather well determined. Other models have been investigated by Fregeau, but all successful models give $4\pi r^2 \rho$ curves similar to Fig. 37. For the best-fitting model, the rms radius has the value 2.40 ± 0.05 fermis. The value of r_0 for an equivalent uniform model [Eq. (1)] is 1.36 fermis.

The behavior of the inelastic scattering curves has been examined by Ravenhall and by Morpurgo. In the case of the 4.43-Mev level, both Ravenhall and Morpurgo find that LS coupling gives better agreement with experiment than the JJ coupling scheme. Morpurgo is also able to explain the behavior of the ratio

of the inelastic cross section relative to the elastic cross section as a function of energy. He also gives a satisfactory explanation of the constancy of the inelastic cross section (4.43 Mev) at 90° between the energies 80–187 Mev. Neither the LS nor the JJ coupling scheme gives exact quantitative agreement with the ratio of the inelastic (4.43 Mev) to elastic cross sections at all the energies studied. The experimental values are larger on the average by a factor of two, as found earlier by Ravenhall. Considering the crudity of the harmonic well model, this disagreement is not considered serious. The angular distribution of the (4.43-Mev) inelastic scattering seems to be given adequately by theory.

Of course, it should be noted that the Born approximation commits an error in dealing with the elastic and inelastic scattering. We have commented on this previously (Secs. IIb and IIc). However, in the case of elastic scattering, the reduction factor (γ) in rms radius between the exact value and the Born approximation value has been estimated by Ravenhall⁸⁰

$$\gamma = \frac{r_{\text{exact}}}{r_{\text{Born}}} = \frac{1}{1 + (3Z\alpha/2kR)} \quad (47)$$

for an equivalent uniform charge distribution of radius R , where α is the fine structure constant and k is the wave number of the incident electrons. In the case of carbon the exact rms radius should, therefore, be 2.37 ± 0.05 fermis instead of 2.40 ± 0.05 fermis. The corrected r_0 of Eq. (1) will then become 1.34 fermis for C¹².

On the theoretical side, a fair amount of work has been carried out on the carbon nucleus. The rms radius estimate of Ferrell and Visscher⁷⁶ for the ground state of C¹² ($a=2.3 \pm 0.2$ fermis) is in good agreement with the experimental value 2.37 fermis. Besides the calculations on the scattering from the 4.43 level,^{78,79} other calculations on the 7.65⁻⁸¹ and 9.61⁻⁸² Mev levels have

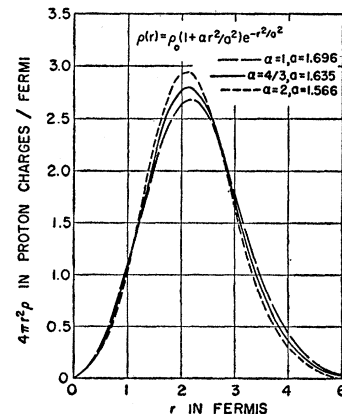


FIG. 37. The same charge distributions appearing in Fig. 36 when multiplied by $4\pi r^2$. Note the similarity of the resulting distributions.

⁷⁸ D. G. Ravenhall (to be published).

⁷⁹ G. Morpurgo, Nuovo cimento III, No. 2, 430 (1956).

⁸⁰ D. G. Ravenhall (private communication).

⁸¹ L. I. Schiff, Phys. Rev. 98, 1281 (1955).

⁸² D. G. Ravenhall, Phys. Rev. 100, 1797 (1955).

been made. Schiff⁸¹ has found that an alpha-particle model of C^{12} and an elastic fluid model both yield too-large values of the transition matrix element from the 7.65-Mev level to the ground state. He has also used the independent particle model and a JJ coupling scheme to investigate a two-nucleon transition between the $p_{3/2}$ and $p_{1/2}$ shells. In this case the transition matrix element turned out to be too small by about a factor of six. Schiff concludes that an intermediate type of model is required, i.e., one more collective in character than the independent particle model (with only pair interactions) and less collective than the alpha-particle model or elastic fluid model. Glassgold and Galonsky⁸³ have shown that an alpha-particle model of the C^{12} nucleus is consistent with the radius of the charge distribution in the ground state. However, this model, though successful for O^{16} , predicts a state at 5.54 Mev in C^{12} which has not been observed.

(f) Magnesium, Silicon, Sulfur, Argon, and Strontium

R. H. Helm⁴⁶ has made an electron-scattering survey of the even-even nuclei: $^{12}Mg^{24}$, $^{14}Si^{28}$, $^{16}S^{32}$, $^{18}A^{40}$, and $^{38}Sr^{88}$, in order to study the 0–2 transitions between the ground and first excited states, in addition to the elastic scattering. The first excited levels are sufficiently far removed from the ground state so that inelastic scattering can be resolved from the elastic scattering.

Helm's experimental results for the elastic scattering are shown in Fig. 38 and include Fregeau and Hofstadter's curve for C^{12} . Typical diffraction features are exhibited by the ordinate, which is the square of the form factor. The inelastic data of Helm are summarized

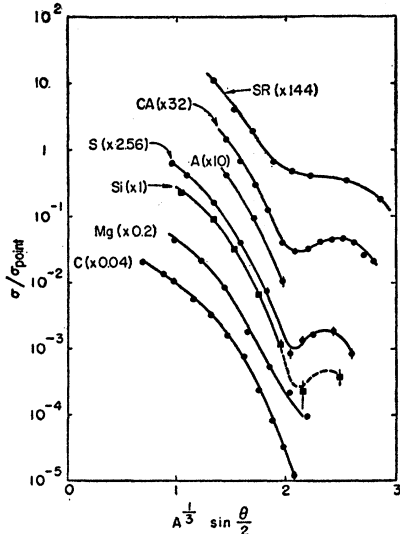


FIG. 38. The square of the form factor for elastic scattering of 187-Mev electrons from even-even nuclei. The diffraction dips occur at essentially the same value of the abscissa. This suggests that a radial parameter varies as $A^{1/3}$. This figure is due to Helm.⁴⁶

⁸³ A. E. Glassgold and A. Galonsky (to be published).

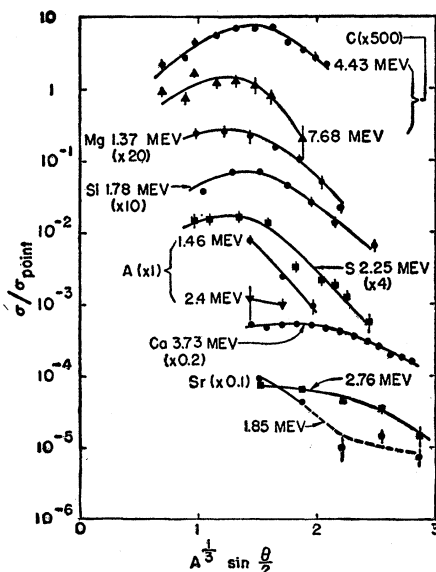


FIG. 39. Inelastic data for even-even nuclei. The ordinate is the square of a form factor for the inelastic processes.

in Fig. 39 as well as some of the carbon results. Here again the actual cross section is divided by the point charge cross section to obtain an effective (form factor)² for inelastic scattering.

Helm has developed a new and interesting "folded" charge distribution given, for example, by

$$\rho(r) = \int \rho_0(r) \rho_1(r-r') d^3r', \quad (48)$$

where $\rho_0(r)$ is a uniform charge distribution out to a distance $r=R$, i.e.,

$$\rho_0(r) = \begin{cases} 3/4\pi R^3 & r \leq R \\ 0 & r > R \end{cases} \quad (49)$$

and where

$$\rho_1(r) = \frac{1}{(2\pi g^2)^{3/2}} \exp[-(r^2/2g^2)]. \quad (50)$$

Helm calls this particular model the "Gaussian uniform" or gU distribution. This formulation has the advantage that the resultant form factor is the product of the two individual form factors

$$F(q) = F_0(q) F_1(q), \quad (51)$$

where the F_0 and F_1 are defined as usual by Eq. (17). Helm uses uU , or uniform-uniform folds, also. The folding procedure is satisfactory only as long as the Born approximation is valid.

The results obtained by applying the gU model to the data give the values in Table III. The radial estimates are corrected for the error made in using the Born approximation, *viz.*, Eq. (47). To compare the results with other experiments, the rms radius can be calculated from the gU distribution and can be equated

TABLE III. gU distribution. This table gives Helm's results for the radii of even-even nuclei and includes the C^{12} data of Fregeau and Hofstadter. The accuracy in the table is about 2–3%. Lengths are in units of 10^{-13} cm.

Element	r_0	$r_1 = cA^{-\frac{1}{3}}$	t
C^{12}	1.35	0.95	2.2
Mg^{24}	1.33	0.99	2.6
Si^{28}	1.29	0.97	2.8
S^{32}	1.30	1.03	2.6
Ca^{40}	1.28	1.08	2.4
Sr^{88}	1.20	1.08	2.3

to the rms radius for an “equivalent” uniform distribution of charge given by Eq. (1). An equivalent r_0 in Eq. (1) can, therefore, be deduced. This is the quantity given under the r_0 column of Table III. Such a procedure results in the expression for r_0 .

$$r_0 = (5/3)^{\frac{1}{3}} a A^{-\frac{1}{3}}, \quad (52)$$

where a is the root-mean-square radius of any charge distribution. The columns r_1 and t are related to the parameters defined by Hahn *et al.*³³ and refer to the “half-density” distance (c) and the skin thickness (t) of the charge distributions defined in that paper (see also Sec. Vg). The quantity r_1 is defined as

$$r_1 = c A^{-\frac{1}{3}}, \quad (53)$$

and t is the 90%–10% distance in the skin. The values obtained by Helm are reproduced in Table III and will be commented on later in the resumé on nuclear radii. Helm's uU results are similar to the gU results.

The most interesting result on inelastic scattering is shown in Fig. 40. This figure shows that, if the experimental cross sections are divided by the point-charge cross sections and arbitrarily normalized together at the maximum values of the form factors, several “universal” curves are obtained. The suggestion is made, therefore, that each electric multipole transition

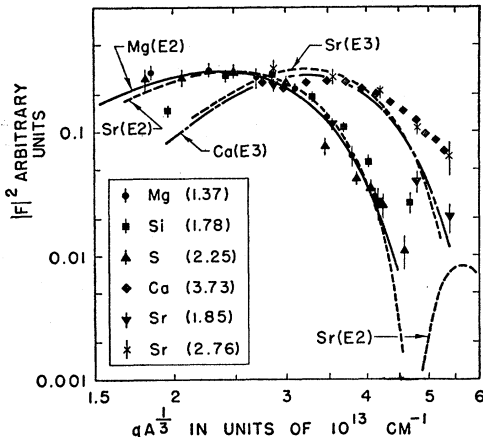


FIG. 40. The square of a form factor for inelastic scattering is plotted against a variable proportional to $A^{\frac{1}{3}} \sin \theta/2$. When the maxima are normalized together, Helm⁴⁶ obtains “universal” curves for various multipole transitions.

corresponds to its own universal curve for each value of $l=0, 2, 3$, etc. This, of course, may not be a general rule, but it seems to apply to these cases. As a result the assignment $J=2^+$ for S^{32} (2.25 Mev) and $J=3^-$ for Ca^{40} (3.73 Mev) can be made.⁸⁴ Helm⁴⁶ has also interpreted the relative intensities of the inelastic transitions in terms of a theory of Ravenhall⁸⁵ based on the Schiff treatment⁴⁷ which yields values for the partial level widths due to radiation.

(g) Medium-Heavy and Heavy Elements

The elements Ca, V, Co, In, Sb, Hf, Ta, W, Au, Bi, Th, and U were investigated by Hahn, Ravenhall, and Hofstadter³³ at an energy of 183 Mev and In, Au, and Bi at 153 Mev. Special attention was given to gold because of the previous information already available on this element. The early results on Au¹⁹⁷ and Pb²⁰⁸^{4,86}

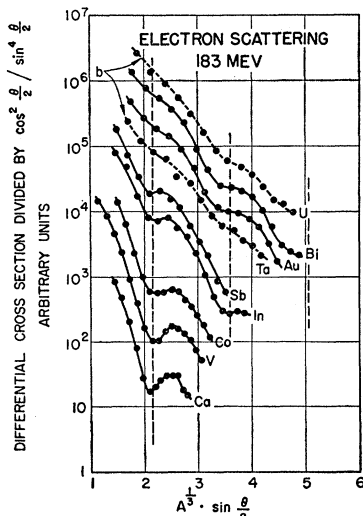


FIG. 41. Experimental results of Hahn *et al.*³³ which show that a radial parameter of the various charge distributions follows an $A^{\frac{1}{3}}$ law. The diffraction features are clearly evident and are emphasized at lower atomic numbers.

showed that two principal parameters governing the charge distribution were determinable from the experiments at these energies. These two parameters are called c and t and have been referred to previously. They are shown for a special model (Fig. 7), herein called the Fermi model. In general, these quantities refer to a radius parameter and to a surface thickness. The purpose of the investigation of Hahn *et al.* was to study how the two parameters varied over the range of nuclei from Ca to Bi. Only spherical nuclei were investigated in this connection. It was also desired to know how widely the two parameters might be adjusted so that they could still produce a good fit with experiment for the selected model. Other nonspherical nuclei (Hf, Ta, W, Th, and U) were investigated experimentally but no detailed interpretation of the results was given.

⁸⁴ D. G. Ravenhall and B. Hahn have also pointed out that these assignments appeared reasonable (unpublished).

⁸⁵ D. G. Ravenhall (to be published).

⁸⁶ D. G. Ravenhall and D. R. Yennie, Phys. Rev. **96**, 239 (1954).

The main experimental results are shown in Fig. 41, in which the Mott cross section has been arbitrarily divided out to better exhibit the diffraction effects. The phase shift method was employed in the manner of Yennie *et al.*^{17,18} since the Born approximation would be very poor for many of the elements investigated. Nevertheless, the angular positions of the diffraction dips in Fig. 41 occur at nearly the same value of $A^{\frac{1}{3}} \sin\theta/2$. According to the Born approximation, this fact suggests that some parameter, related to a radius, varies approximately as $A^{\frac{1}{3}}$. The parameter c , as we shall see later, is such a quantity. Some of the nuclei were chosen for study because they are near magic numbers such as Ca, In, Sb, Au, Bi, and presumably are spherical. Some were selected because they consist essentially of no more than a single isotope (Ca, V, Co, In, Ta, Au, Bi). The principal findings are given below.

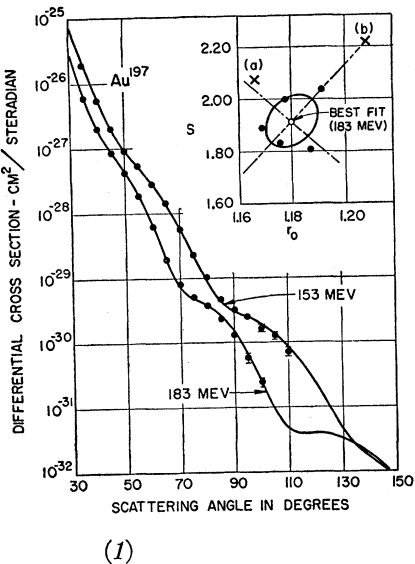


FIG. 42. Experimental points in gold at 153 and 183 Mev are compared with theoretical curves of Hahn *et al.*³³ obtained by phase shift methods. Sketch in inset is concerned with finding best statistical fit.

Au was studied in some detail. The experimental results are shown in Fig. 42 at two energies, 153 and 183 Mev. The diffraction dips are visible particularly if the curves are viewed along their lengths. These curves are not divided by a Mott factor, as in Fig. 41. The sketch in the insert refers to parameters used in Hahn *et al.* to find the best fit. The parameters s and r_0 are related to t and c . r_0 is the coefficient in Eq. (1) for the equivalent uniform sphere.

To fit the experimental curves, three test models were chosen.³⁷ Their forms are

$$\text{Fermi: } \rho(r) = \rho_1 / \{ \exp[(r - c)/z_1] + 1 \}; \quad (54)$$

$$\text{Modified Gaussian: } \rho(r) = \rho_2 / \{ \exp[(r^2 - c^2)/z_2^2] + 1 \}; \quad (55)$$

$$\begin{aligned} \text{Trapezoidal: } \rho(r) &= \rho_3, \quad 0 < r < c - z_3 \\ &= \rho_3(c + z_3 - r)/2z_3, \quad c - z_3 < r < c + z_3, \\ &= 0, \quad r > c + z_3. \end{aligned} \quad (56)$$

³⁷ The terminology of Hahn *et al.*³³ is used here.

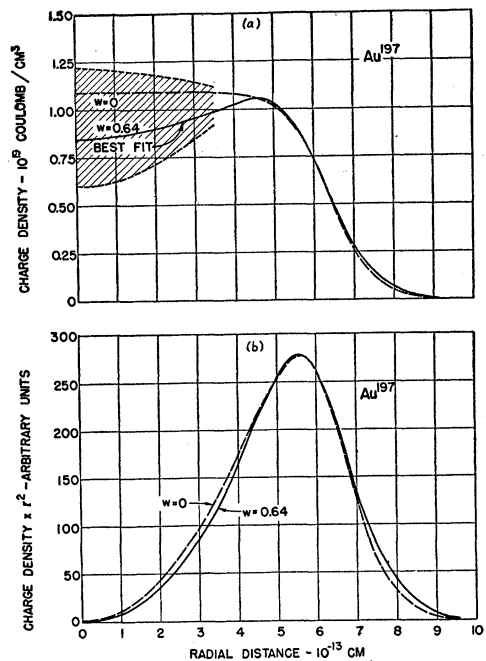


FIG. 43. Various gold charge density models which yield theoretical scattering curves very close to the best fitting ones of Fig. 42. The "best fit" in Fig. 43 (a) appears to have a small central depression, but the difference between the central depression ($w=0.64$) and the Fermi model ($w=0.0$) lies within the probable error of the determination. Figure 43 (b) shows why this is so. The curves represent $4\pi r^2 \rho$ or the amount of charge in a unit shell. Very little charge resides near the origin, and the amount of charge in a shell is very similar for models $w=0.64$ and $w=0.0$.

The parameters are defined by the equations themselves. For the various shapes it is useful to define the parameter c .

$$c = \frac{1}{\rho(0)} \int_0^\infty \rho(r) dr. \quad (57)$$

For shapes with a symmetrical skin, c is the distance from the center of the nucleus to the radius where the

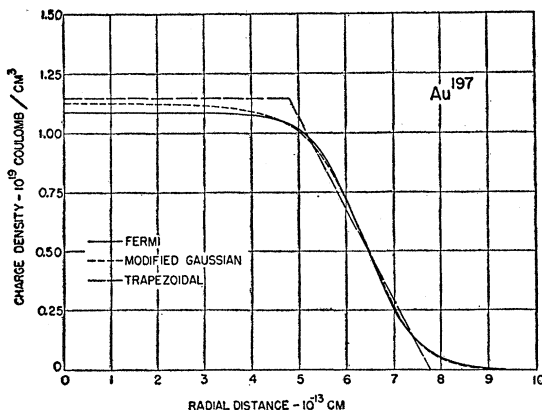


FIG. 44. Three models which fit the data in gold equally well.

charge density ρ has dropped to half its value at the center. For the Fermi shape, the skin parameter " t ", which gives the distance between the 90% and 10% values of ρ , is given by $4.40 z_1$. For the modified Gaussian, $t=2.20 z_2^2/c$ and for the trapezoidal model, $t=1.60 z_3$.

The central charge density in Au was varied by using the model

$$\rho(r) = \rho_s [1 + (wr^2/c^2)] / \{\exp[(r-c)/z_8] + 1\} \quad (58)$$

to see the effects of low and high central densities. In all cases a least square analysis was used to find the models with minimum errors. Figures 43(a) and 43(b) show the attempts made to fit the experimental Au points of Fig. 42. The best fit is indicated for $w=0.64$. However, Fig. 43(b) shows that the Fermi model ($w=0$) is so little different from the best fit, when expressed as $4\pi r^2 \rho$, that the added complication of carrying a third parameter w appears to be unnecessary with the present experimental accuracy.

Furthermore, Fig. 44 shows the three models which give "best fits" in their classes. The experiments are unable to distinguish between these three possibilities within the present limits of accuracy. It is to be noted that the three charge densities cross each other almost in the same positions on the downward slope of the skin. Such results show that only two parameters can be determined at present, namely, c and t , or something close to these two. These two parameters represent the common features of all models that fit the data.

The same model (Fermi shape), with the same numerical values of the parameter, fits the Au points at both 153 and 183 Mev as shown by the solid lines of Fig. 42. On the other hand, Fig. 45 shows definite discernible discrepancies. The two theoretical curves (a) and (b) which show discrepancies are based on the Fermi model with parameters differing slightly from those of the best fit. Both (a) and (b) refer to 183 Mev.

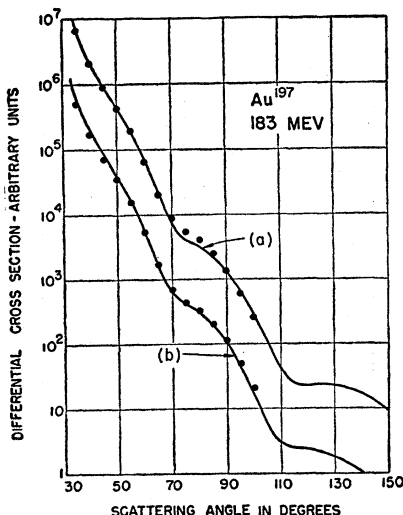


FIG. 45. Theoretical curves which are believed *not* to fit the experimental points. such curves lead to the limits of error assigned to the gold radius and thickness parameters.

The differences between models (a) and (b) are about the same as those between the models of Fig. 44.

(2)

Other elements were examined with only the Fermi model as the theoretical vehicle. The accuracy of these experimental runs is not as great as that in gold and different models are not at present justified. Figure 46 shows the experimental points for In as well as the solid theoretical lines. The fit is quite good.

Experience with the Fermi model shows that the parameter c mainly determines the angular position of the diffraction dips while the parameter t is concerned with the depth of the dips. Thus, the behavior exhibited in Fig. 41 must be correlated with a variation of c as the one-third power of A . This conclusion is verified below (see paragraph 3).

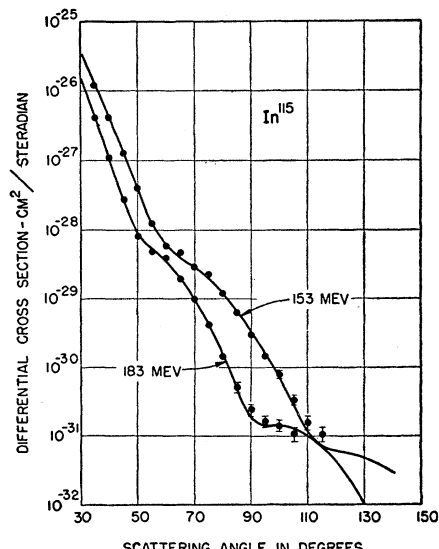


FIG. 46. Theoretical and experimental curves for In¹¹⁵ at two energies.

(3)

The results for the various nuclei are summarized in Fig. 47. These results are all based on the Fermi model. Table IV presents the relevant numerical data. Several interesting facts are revealed by Fig. 47 and Table IV: (a) The nuclear skin thickness seems to be a constant ≈ 2.4 fermis for all the nuclei investigated; (b) The radius parameter c varies as $1.08 A^{1/3}$ as suggested by Fig. 41. Thus, the flat portion shrinks towards the center as the nuclei become lighter. In the very light nuclei ($Z \leq 6$) it disappears. The behavior of r_0 of Eq. (1) is now seen to vary from low values, ~ 1.19 , for heavy elements to 1.32 for Ca. This trend continues towards lighter elements as we may see by examining Table III (1.33 for Mg²⁴ and 1.35 for C¹²). The differences between Helm's value 1.28 for Ca⁴⁰ (Table III)

and Hahn *et al.*'s value are due to the use of different models.

For the lighter nuclei, where the central flatter area shrinks towards nothing, and where, e.g., in carbon, a modified Gaussian is a better fit (Fregeau), the significance of t can be expected to decline. In still lighter elements the whole nucleus is not even as large as the skin — 2.4 fermis.

Thus, a comparison of these results with the assumed constancy of r_0 in Eq. (1) is not favorable. These models do not give a constant r_0 . The trend appears to be: small r_0 at large A , larger r_0 at small A . However, further data on other nuclei are required before this conclusion may be accepted for all nuclei. It is probable that local variations of r_0 may show exceptions to the rule.

(4)

For the nonspherical nuclei, Hahn *et al.* give the results shown in Fig. 48. These nuclei show smoother,

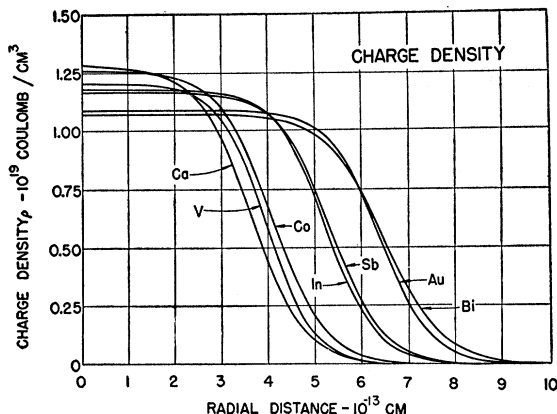


FIG. 47. Fermi models for various nuclei. Note the increase in average central charge density as Z decreases.

less well-defined diffraction features than, e.g., gold in Fig. 42. This has been interpreted qualitatively as evidence for quadrupole (ellipsoidal) distortions of such nuclei.

It is well known from other experiments that the nuclei of Fig. 48 have low-lying levels appearing strongly in Coulomb excitation and indicating large intrinsic-quadrupole moments. This is suggestive of large distortions from spherical symmetry which are associated with the collective motion of the outer nucleons.⁶⁰

A detailed calculation has been carried out by Downs and Downs *et al.*,⁶¹ etc. who have used a modified-Born approximation approach to estimate the effect of quadrupole scattering in "filling up" the diffraction dips observed in the scattering from spherical nuclei.

⁶⁰ B. W. Downs, Ph.D. thesis, Stanford University, October, 1955; Downs, Ravenhall, and Yennie, Phys. Rev. 98, 277(A) (1955); Yennie, Ravenhall, and Downs, Phys. Rev. 98, 277(A) (1955).

TABLE IV. Results of the analysis of nuclei in terms of the Fermi smoothed uniform charge distribution. All lengths are in Fermi units, charge densities in 10^{19} coulombs/cm 3 . The accuracy of these results is thought to be: radial parameters, $\pm 2\%$; surface thickness parameter, $\pm 10\%$. For lighter elements, the errors are probably larger. The accuracy for gold is higher. R is the radius of uniform charge distribution having the same rms radius as the Fermi distribution.

Nucleus	c	t	R	$c/A^{1/3} = r_1$	$R/A^{1/3} = r_0$
$^{20}\text{Ca}^{40}$	3.64	2.5	4.54	1.06	1.32
$^{23}\text{V}^{51}$	3.98	2.2	4.63	1.07	1.25
$^{27}\text{Co}^{59}$	4.09	2.5	4.94	1.05	1.27
$^{49}\text{In}^{115}$	5.24	2.3	5.80	1.08	1.19
$^{51}\text{Sb}^{122}$	5.32	2.5	5.97	1.07	1.20
$^{79}\text{Au}^{197}$	6.38	2.32	6.87	1.096	1.180
$^{83}\text{Bi}^{209}$	6.47	2.7	7.13	1.09	1.20

There are three contributions which arise from quadrupole effects; (1) The ellipsoidal distortions must be averaged over all orientations and lead to a nuclear density ρ_s having an effective surface thicker than one appropriate to a nucleus without the distortions. The elastic scattering from this type of quadrupole smoothing is shown as σ_s in Fig. 49, due to Downs. (2) A second type of elastic scattering corresponds to changing the orientation of the nuclear spin axis, that is, "spin flip." Since the nucleus is aspherical, this type of transition can occur. This scattering, when averaged over all orientations of the nuclei, adds independently to the elastic scattering (1) above. For oriented nuclei interference effects might be observed. (3) An inelastic scattering, representing the transitions from the ground

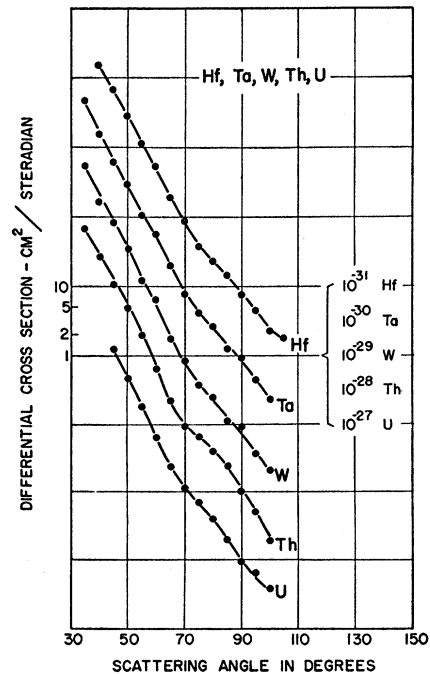


FIG. 48. The experimental data for nuclei believed to be appreciably nonspherical. The diffraction features appear to be smoothed out relative to gold.

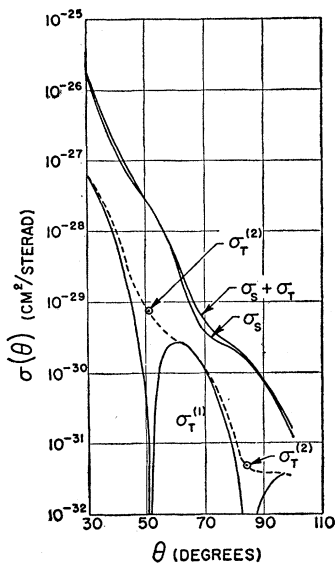


FIG. 49. Theoretical curves of Downs *et al.*⁸⁸ for the tantalum nucleus calculated with assumptions described in the text concerning quadrupole scattering.

state to the low-lying excited states, though actually inelastic, makes a contribution to the scattering usually called elastic. This contribution lies so close to the elastic scattering (~ 1 part in 2000) that it may be considered at present to be elastic, from a practical point of view.

As a result of (2) and (3), the contribution in Fig. 49, labeled $\sigma_T(2)$ adds to the elastic scattering σ_s to give the total scattering $\sigma_s + \sigma_T$. The latter should be compared with experiment. The curve σ_T , thus, represents the quadrupole scattering. Curve $\sigma_T(2)$ is an approximation and was estimated from the Born approximation $\sigma_T(1)$ for a pure quadrupole and a higher order approximation which does not vanish at the zeroes of the Born-quadrupole scattering. Curve $\sigma_T(2)$ is sketched as shown and is not calculated, except for the two points indicated by circles.

Figure 50 shows the same kind of computation for tantalum, using three values of the intrinsic quadrupole moment Q_0 , which represent three increasing states of nuclear distortion. The experimental points of Hahn and Hofstadter⁸⁹ are shown in the figure. It is clear that an intermediate value of Q_0 between 7 and 14 barns will fit the data. However, the calculations are not considered reliable enough by Downs to extract an actual value of the quadrupole moment. The probable reason for the smoothness of the curves in Fig. 48 is, with little doubt, due to such quadrupole contributions to the scattering.

VI. THE NEUTRON

It would be of great interest to determine the internal structure of the neutron, or at least to determine as much as is now known about the structure of the proton. The neutron-electron interaction has been inves-

tigated by Fermi, Rabi, Hughes, and their collaborators⁹⁰ and shows a surprisingly small effective charge distribution. These experiments, however, throw no light on the size or shape of the neutron's magnetic moment. It is precisely here that the electron scattering method can contribute significant information.

As a method of seeking this information, the following thought occurred to the present author: When large momentum transfers occur in the inelastic scattering of electrons from the deuteron (or Be^9 where there is a well-known loose neutron on the outside of the nucleus), the neutron and proton can be considered essentially as free particles since the binding in the deuteron is weak. Furthermore, at large angles and high energies, the electron scattering is almost entirely governed by the magnetic moment of the nucleon (Rosenbluth). Consequently, since the magnetic moment of the neutron is -1.91 nuclear magnetons and that of the proton is 2.79 nuclear magnetons, the scattering of electrons from protons should be only $[(2.79/1.91)^2 \approx 2]$ or about twice as large as from the neutron. This assumes that the particles are points or that their magnetic moment clouds have equal sizes. However, if the neutron should have smaller dimensions than the proton, its magnetic scattering should approach and perhaps exceed that of the proton. If the sizes are similar the neutron should scatter about half as much as the proton. By scattering electrons inelastically from deuterium⁷⁰ and comparing such scattering with that from free protons in hydrogen, the deuterium-hydrogen difference should yield the neutron scattering cross section and, hence, its size.

This argument is borne out by the detailed theory of Jankus.⁹¹ In fact, whenever F_D is small, Eq. (43) can be

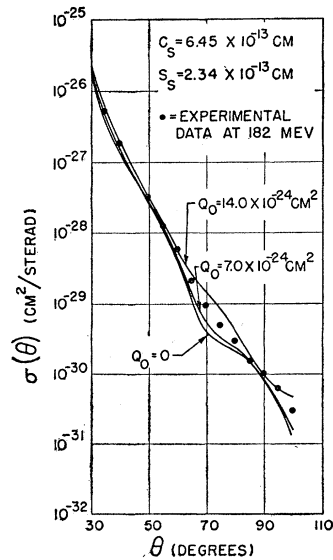


FIG. 50 Comparison of the calculation of Downs *et al.*⁸⁸ with the experiment of Hahn and Hofstadter⁸⁹ on tantalum.

⁸⁹ B. Hahn and R. Hofstadter, Phys. Rev. 98, 278(A) (1955).

⁹⁰ For a summary, see B. T. Feld, *Experimental Nuclear Physics*, edited by E. Segré (John Wiley and Sons, Inc., New York, 1953), Vol. II, p. 208.

written as follows:

$$\sigma_D^{\text{in}}(\theta) = \sigma_{\text{NS}} \{ 1 + (q^2/4M^2) [2\mu_p^2 \tan^2 \frac{1}{2}\theta + \mu_p^2] \} + \sigma_{\text{NS}} \{ (q^2/4M^2) [2\mu_n^2 \tan^2 \frac{1}{2}\theta + \mu_n^2] \}. \quad (59)$$

$$\sigma_D^{\text{in}}(\theta) = \sigma_p + \sigma_n. \quad (60)$$

Equation (60) is equivalent to the qualitative statement given above, but the latter is now expressed in exact form. Consequently, by a deuterium-hydrogen difference method, the value of σ_n may be found. From σ_n a form factor calculation, in association with σ_p , will yield the dimensions of the neutron.

The actual experiment is difficult to perform because of the spreading-out of the inelastic continuum due to the motion of the neutron and proton inside the deuteron. Figure 51 shows the approximate shape of this distribution obtained by Blankenbecler, Hofstadter, and Yearian⁵⁰ in recent preliminary experiments and shows the momentum distribution in the deuteron. The proton comparison peak is, however, a sharp one with a bremsstrahlung tail on the low-energy side. The elementary scattering from the deuteron's moving neutron and proton will show the same bremsstrahlung tails, but this radiative cross section will itself lie in the inelastic continuum. Proper appreciation of this correction is necessary in carrying out the subtraction.

Only preliminary data are available. The first indications suggest that the neutron's magnetic scattering is perhaps less than, but comparable with, the proton scattering at 135° and 500 Mev,^{42,68} but the accuracy is poor. If this result should continue to be true as the experiments improve, the neutron would have about the same dimensions of its magnetic moment cloud as the proton or perhaps a bit smaller. The present experi-

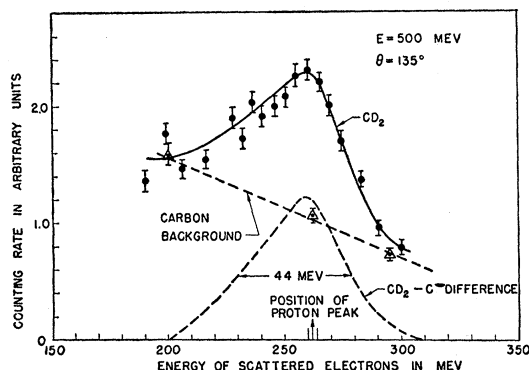


FIG. 51. Inelastic electron scattering in the deuteron for 500 Mev incident electrons deflected through 135°.⁵⁰ The upper curve shows the data in deuterated polyethylene (CD₂) and the triangular points show the corresponding contribution from pure carbon. The difference between the CD₂ and C data furnishes the dotted curve indicated in the lower position. The data are corrected for the dispersion of the spectrometer. The dotted curve is a preliminary indication of the momentum distribution in the deuteron and represents $\sigma_D^{\text{in}}(135^\circ) = \sigma_p + \sigma_n$ as expressed in Eq. (59). After subtraction of the area under the sharp free proton peak σ_p , the remainder represents σ_n .

ments appear to indicate more definitely that the neutron's magnetic cloud is not as small as found in the static experiments.⁹⁰

Other preliminary data on Be⁹ have recently been obtained by Chambers and Hofstadter⁹¹ which show that the method is feasible with beryllium and perhaps with many other nuclei, including isotopes differing by one neutron.

VII. VALIDITY OF ELECTRODYNAMICS

It was pointed out³ that the deviations observed in electron scattering experiments between actual scattering cross sections and those expected from a point charge could be wholly or partially ascribed to departures, at small distance, from the Coulomb law of electric interaction. In other words, the deviations which have been explained as finite size effects would be attributed to a failure of electrodynamics and the bodies themselves could be considered to be points. There are now too many independent pieces of evidence to the contrary to suppose that this view could be maintained for nuclei. It could, however, still be thought that the "differences" between electromagnetic sizes and nucleonic sizes could be due to such a failure, but this also appears to be unlikely, since, as the experiments and the interpretations are improved, the differences become smaller and smaller.

In the case of the proton and the neutron, we are confronted with a different situation, for it has not proved possible experimentally to fix any size on these particles prior to the recent experiments in electron scattering. It is true that meson theories predict that the meson clouds around the fundamental nucleons have dimensions lying somewhere between the Compton wavelengths of the nucleon and the pion, 0.2 fermi and 1.4 fermis, respectively, and probably closer to the smaller dimensions. Although the methods of meson theory have been fruitful qualitatively, they have not been spectacularly successful quantitatively, and at the present time it is difficult to have confidence in the predictions of any meson theory. Consequently, it would be quite consistent with known facts to attribute the radial dimensions, measured by McAllister, Chambers, and Hofstadter, of 0.77 fermi for the proton to a failure of electrodynamics, and to assume that the meson clouds are really quite small compared to 0.77 fermi. As far as concerns the electron-scattering experiments on the proton, either explanation is tenable⁶⁷ and, in fact, both finite size effects and a failure of electrodynamics may occur together. The final explanation of the scattering results would be identical in either of the two. There may even be some doubt that finite size effects and a breakdown of electrodynamics are not two aspects of the same phenomenon.

A simple illustration of how similar the two possibilities appear is the following: To explain the experi-

⁹¹ E. E. Chambers and R. Hofstadter (unpublished).

ments, a finite size and a given model, say, a Gaussian, are ascribed to the proton charge cloud. The Coulomb-potential function, in consequence, is rounded off so that it becomes finite at zero radius, whereas, if the proton is considered to be a point, the potential goes to minus infinity at zero radius. The algebraic difference between these two potential functions can be considered to be the law of deviation from the Coulomb interaction at small distances. A new potential, incorporating this deviation, will represent the "revised Coulomb law." We shall then have a specific model showing how the electrodynamic laws break down at small distances: i.e., a new law of force valid at all ordinary distances but with a new behavior at very small distances. A parallel situation would occur in the case of the magnetic charge density of the proton. The same breakdown would cover both cases simultaneously.

There may be several possible ways of distinguishing between a finite size and a failure of electrodynamics: One way would be to scatter electrons against electrons at high enough energies (~ 20 Bev) so that the center-of-mass de Broglie wavelength becomes comparable with the small dimensions inside which the Coulomb law may be conceived of as breaking down. Another way, more amenable to present experimental technique, would be to determine the neutron's dimensions, as discussed in Sec. VI. If the neutron's size turns out to be identical with that of the proton, it would appear that electrodynamics breaks down at certain small dimensions, and all objects smaller than these dimensions, including the neutron and the proton, appear to have the same size. On the other hand, if the neutron's size (or shape) appears to be different from the proton's, then it would seem reasonable to say that the sizes represent, at least in part, real structural effects and that the laws of electrodynamics are probably still valid even at small distances. A third way would be to see whether the radii of very light nuclei measured by, say, mirror nuclei methods, are the same as those measured by electron scattering methods. If consistency is obtained between these sets of measurements, this would be evidence for the validity of the Coulomb law. Unfortunately, the accuracy of the two sets of determinations is perhaps one order of magnitude smaller than needed to make an accurate assay of the situation. Other methods, making only light demands on nuclear theory, might also be acceptable for such a test. It is also possible that experiments on bremsstrahlung or pair production at large angles, perhaps in hydrogen or other nuclei, could help to settle this unresolved question. Perhaps mesonic atoms will help here, too.

It is entirely pertinent, at this stage, to ask about the size of the electron. It is conceivable that many of the facts pertaining to nucleon sizes could be attributed to a radius of the electron. The question cannot be answered in a very satisfactory way because, if finite

electrons are permitted to enter the picture, the Dirac theory, the backbone of the calculations with electrons, cannot be used without trepidation. In other words, the point electron and the Dirac theory go together at the present stage of knowledge. Of course, due to the electron's recoil during the ever-present virtual emission and absorption of photons to and from the radiation field, the electron *does* have a size and is not, strictly speaking, a point. But this size is equivalent in essence to the effects of the Schwinger radiative correction. These effects are not large and are one order of magnitude smaller than the proton's radius. Thus, at the moment, the question of electron size must be left unanswered. Consistency tests between electron scattering measurements and other types of measurements will help to provide a clear-cut answer to the question of electron size.

VIII. COMPARISONS WITH OTHER MEASUREMENTS OF NUCLEAR SIZES

There are many ways in which nuclear sizes and charge distributions may be measured. The recent review article by Ford and Hill⁹ presents a good summary of the available methods. Besides electron scattering, some of the various possible methods are the following:

- I. Charge sensitive methods
 - a. Coulomb effects in mirror nuclei.
 - b. μ -mesonic atoms and μ -meson scattering.
 - c. Fine structure in x-ray spectra.
 - d. Isotope shifts.
 - e. Hyperfine structure in hydrogen.
- II. Range of nuclear force methods
 - f. Medium-energy (14 Mev–25 Mev) neutron-scattering experiments.
 - g. Higher energy (90-Mev) neutron-scattering measurements.
 - h. Ultra-high energy (1.4-Bev) neutron-scattering measurements.
 - i. Proton-scattering experiments (20 Mev–340 Mev).
 - j. Alpha-particle-scattering experiments (13–42 Mev).
- Combination of I and II
 - k. Weiszacker semiempirical formula for binding energies.
 - l. Alpha-particle radioactivities.

There are probably many other methods in which nuclear sizes are important and, consequently, through which they may be measured.⁹²

It is not the purpose of this report to enter into a detailed discussion of the results of the various methods listed above. This has been well done in the article by Ford and Hill. It is probably useful, however, to point out that the present circumstances do not favor making

⁹² An example is given by Millburn, Birnbaum, Crandall, and Schecter, Phys. Rev. 95, 1268 (1954).

accurate comparisons among the different methods, primarily because of a paucity of experimental data and the reliable interpretations of these data. This is an understandable situation in view of our present ignorance of the nuclear law of force. Nevertheless, it may still be worthwhile to compare briefly a few examples where the data and interpretation appear to be satisfactory. We shall do this below.

a. On the basis of the shell model, including exchange effects for mirror nuclei pairs, Jancovici⁸ calculates a quantity he defines as a ratio of a Coulombic to a mesonic radius of O¹⁷ and N¹⁵. These ratios are 1.18 for O¹⁷ and 1.07 for N¹⁵. Experimentally, one finds 1.27 and 1.17 for these same ratios assuming that the mesonic radii for light nuclei follow Eq. (1) with $r_0 = 1.20$ fermis. This seems to imply a discrepancy between mesonic radii and mirror nuclear radii. On the other hand, if the mesonic radii are actually in the neighborhood of $r_0 = 1.30$ fermis, instead of 1.20 fermis, the discrepancy would be removed. It is interesting that the electron-scattering results on nuclei in this region^{33,46} lie close to the value $r_0 = 1.32$.

Carlson and Talmi⁹³ have also made calculations on pairing effects in Coulomb energies and have related them to determinations of nuclear radii. These authors obtain the r_0 values given in Table V. For nuclei for which $A < 11$ and those for which $A > 28$, the calculations are less reliable than for those between $A = 11$ and $A = 28$. The table shows a smooth decrease in radius between C¹³ and Al²⁷ from values of $r_0 = 1.34$ to 1.20 fermis. The results for $A > 28$ suggest an increase again in r_0 to values near 1.32 fermis. If these results are substantiated, it appears that local variations of r_0 may be expected to occur in other places and that a smooth variation of r_0 over the whole periodic system is more than can be expected.

These results suggest that generalizations about nuclear radii from a few cases should not be made. Furthermore, as evidenced by the work on electron scattering, more than one single parameter is required to specify a charge distribution and a simple rms radius may not be sufficient for this purpose. Thus, in comparing results of different methods, the often-stated counsel should be heeded; The various methods may measure *different quantities* which are represented as radii, and the results should be compared only with this in mind or under special circumstances. This is, of course, especially true when charge or electromagnetic radii are compared with the nucleonic radii determined by methods involving the range of nuclear forces.

b. The μ -mesonic results appear to be in excellent agreement with electron scattering results for the heavy elements.⁹⁴ In the case of lead, the agreement is within 1%. In the case of lighter nuclei, there may be some discrepancies with electron-scattering results although, so far, the mesonic-atom conclusions have less accuracy

⁹³ B. C. Carlson and I. Talmi, Phys. Rev. **96**, 436 (1954).

⁹⁴ Hill, Freeman, and Ford; quoted in reference 9, p. 36.

TABLE V. Included in this table are the r_0 results of Carlson and Talmi (reference 93) on mirror nuclei.

Nucleus	r_0
Li ⁷	1.489
Be ⁹	1.543
B ¹¹	1.283
C ¹³	1.340
N ¹⁵	1.305
O ¹⁷	1.262
F ¹⁹	1.259
Ne ²¹	1.248
Na ²³	1.217
Mg ²⁵	1.230
Al ²⁷	1.197

in this range than for heavy nuclei. There are similar discrepancies of the mesonic data with mirror-nuclei determinations.⁸ On the other hand, as stated above, the mirror nuclei radii appear to agree with electron scattering radii.

At present, the μ -meson results ($2P - 1S$ transition) measure only one parameter which, for light nuclei, is a mean square radius. For heavy nuclei the parameter measured is not exactly a mean square radius and is somewhat dependent on the density distribution. Higher transitions are also slightly sensitive to the charge distribution. The μ -meson method, therefore, seems promising and should help to elucidate the nuclear size question.

(c) The x-ray fine structure splitting in L -series lines has been carried quite far in recent experiments by Shacklett and DuMond^{95,96} but the interpretation of the results is not yet definite. Radii larger than those found by any other method are obtained from the present theoretical interpretation of the data.^{96,97} However, the theory is difficult and the interpretation is probably only in its early stages.

d. Isotope shifts will probably turn out to furnish a good method for evaluating nuclear compressibility, but, at present, do not add much information on nuclear sizes.^{9,98}

e. From the accurate measurement of the hyperfine structure of hydrogen and a highly accurate value of the fine-structure constant, it is possible to determine the spatial extension of the proton's charge and magnetic moment. A calculation of an upper limit of the *mean* radius (not root-mean-square radius) emerges from the analysis of the hyperfine structure by Moellerling *et al.*⁹⁹ The value obtained $R_m < 2.5(\hbar/MC) \approx 0.5 \times 10^{-13}$ cm which is just about at the limit of the electron-scattering result. Further study of this important source of information would be desirable.

⁹⁵ R. L. Shacklett and J. W. M. DuMond, Bull. Am. Phys. Soc. Ser. II, **1**, 219 (1956).

⁹⁶ J. W. M. DuMond (private communication).

⁹⁷ A. L. Schawlow and C. H. Townes, Science **115**, 284 (1952); Phys. Rev. **100**, 1273 (1955).

⁹⁸ Wilets, Hill, and Ford, Phys. Rev. **91**, 1488 (1953).

⁹⁹ Moellerling, Zemach, Klein, and Low, Phys. Rev. **100**, 441 (1955). Also, A. C. Zemach (private communication).

f. The experiments with 14–25 Mev neutrons are divided into two cases:

- (1) Capture (or absorption) cross sections.
- (2) Scattering cross sections.

(1) The experiments related to absorption cross sections were carried out some time ago by Sherr¹⁰⁰ and Amaldi *et al.*¹⁰¹ The experimental cross sections were equated to the asymptotic limit

$$\sigma_T = 2\pi R^2 \quad (61)$$

and a radius was found from this formula. Of course, R here means the radius at which a nuclear force begins to act and, therefore, includes a “radius” of the neutron. It is not at all clear that the interpretation according to Eq. (61) is valid, and in the 14–25 Mev region of neutron energy it is more likely that the factor 2 in Eq. (61) should be replaced by 2.5 for a medium-heavy nucleus.¹⁰² Substitution of this factor into Eq. (61) will result in radii with $r_0 \approx 1.30$ fermis, whereas the results of Sherr and Amaldi are calculated¹⁰² to give r_0 in the neighborhood of 1.40 fermi. Sherr quoted his results in the form

$$R = b + r_0' A^{\frac{1}{3}}, \quad (62)$$

where $b = 1.7$ fermis and $r_0' = 1.22$ fermis, but this is essentially equivalent to $r_0 \approx 1.37 - 1.40$ fermis within the experimental errors. The absorption cross sections, therefore, probably point to smaller values of $r_0 \approx 1.3$ or so when Eq. (61) is corrected.

(2) The neutron scattering cross sections have been measured at 14 Mev by J. H. Coon¹⁰³ and interpreted by Culler, Fernbach, and Sherman¹⁰⁴ using the optical model approach of Fernbach, Serber, and Taylor.¹⁰⁵ A two-step potential function, equivalent to a smoothed well, was employed by Culler *et al.* The potential includes, of course, an imaginary part to account for absorption. The radius of the real part of the well was found to be $1.22 A^{\frac{1}{3}} + 0.74$ fermi, but this is equivalent to about $1.4 A^{\frac{1}{3}}$ for medium range A . J. O. Elliott¹⁰⁶ has also carried out experiments with 14-Mev neutrons on a number of elements and interpreted his results with a simple potential model

$$V = -V_0(1+\xi) \quad \text{for } r < R_0, \quad (63)$$

where $V_0 = 42$ Mev, $\xi = 0.15$ and

$$R_0 = 1.32 A^{\frac{1}{3}} \text{ fermis.} \quad (64)$$

This radius, of course, is an interaction radius and

¹⁰⁰ R. Sherr, Phys. Rev. **68**, 240 (1945).

¹⁰¹ Amaldi, Bocciarelli, Cacciaputo, Trabacchi, Nuovo cimento **3**, 203 (1946).

¹⁰² J. M. Blatt and V. W. Weisskopf, *Theoretical Nuclear Physics* (John Wiley and Sons, Inc., New York, 1952), pp. 356, 482.

¹⁰³ J. H. Coon (referred to in reference 104).

¹⁰⁴ Culler, Fernbach, and Sherman, AEC DUCRL-4436 (January, 1955); also Phys. Rev. **98**, 273 (1955).

¹⁰⁵ Fernbach, Serber, and Taylor, Phys. Rev. **75**, 1352 (1949).

¹⁰⁶ J. O. Elliott, Naval Research Laboratory Report No. 4640 (October, 1955).

includes the “radius” of the neutron equivalently, the range of nuclear forces. This analysis, therefore, gives rather small radii, not far from the electromagnetic radii, when the range of nuclear forces is allowed for.

g. Fernbach *et al.*¹⁰⁵ developed the use of an “optical model” of the nucleus, in which the nucleus is partially transparent at the higher energies and is imagined to be a uniform sphere characterized by a complex refractive index. Without repeating the details here, these authors interpreted the careful scattering experiments of Cook *et al.*¹⁰⁷ at 90 Mev on a large number of elements and obtained a consistent fit to all the data with a spherical nuclear model of radius R where

$$R = 1.37 A^{\frac{1}{3}}. \quad (65)$$

This is quite close to the determination of $R_0 = 1.32 A^{\frac{1}{3}}$ by Elliott,¹⁰⁸ although the models are slightly different. Nevertheless, if the range of nuclear forces is allowed for, say, perhaps 1.0 fermi, the radii will fall close to the electromagnetic values.

h. Recently, important experiments by Coor *et al.*¹⁰⁸ on the absorption of ~ 1.4 -Bev neutrons by several elements were interpreted with the aid of the optical model and gave a consistent determination of the spherical radius $R = 1.28 A^{\frac{1}{3}}$ fermis. Thus, these experiments also indicate small radii. The same experiments were analyzed by Williams¹⁰⁹ who showed that the results were consistent with the electron scattering charge distributions and the small electromagnetic size.

i. Proton scattering experiments in the 20-Mev range were carried out by Cohen and Neidigh¹¹⁰ and by Dayton¹¹¹ and others.¹¹² The scattering cross sections show beautiful diffraction minima and maxima, which offer a splendid opportunity for the eventual determination of much about the structure of nuclei examined in this way. It was not possible to fit the data with an optical model when a square well potential was used.¹¹³ However, Woods and Saxon¹¹⁴ rounded the edge of the nuclear potential as follows:

$$V(r) = \frac{V+iW}{1+\exp[(r-r_2)/a_1]}, \quad (66)$$

where r_2 is a parameter measuring nuclear size and a_1 is related to the diffuseness of the surface, in other words, to the nuclear “skin” thickness. This may be seen to be just the Fermi model used by Hahn *et al.*¹¹⁵ and Yennie *et al.*¹¹⁶ The Coulomb part of the interaction with the incident proton was taken from a uniformly charged sphere with an r_0 consistent with the electro-

¹⁰⁷ Cook, McMillan, Peterson, and Sewell, Phys. Rev. **75**, 7 (1949).

¹⁰⁸ Coor, Hill, Hornyak, Smith, and Snow, Phys. Rev. **98**, 1369 (1955).

¹⁰⁹ R. W. Williams, Phys. Rev. **98**, 1387 (1955).

¹¹⁰ B. L. Cohen and R. V. Neidigh, Phys. Rev. **93**, 282 (1954).

¹¹¹ I. E. Dayton, Phys. Rev. **95**, 754 (1954).

¹¹² J. W. Burkig and B. T. Wright, Phys. Rev. **82**, 451 (1951).

¹¹³ D. M. Chase and F. Rohrlich, Phys. Rev. **94**, 81 (1954).

¹¹⁴ R. D. Woods and D. S. Saxon, Phys. Rev. **95**, 577 (1954).

magnetic values. For platinum, the parameters producing a good fit to the experimental curve of Cohen and Neidigh were $V=38$ Mev, $W=9$ Mev, $r_2=8.24$ fermis, and $a_1=0.49$ fermi. Remembering that $t=4.40 a_1$, for the Fermi model, t becomes 2.16 fermis, in very good agreement with the value consistently appearing in the electron scattering determinations of Hahn *et al.*³³ The model of Woods and Saxon does not fit experiment quite as well for low Z (e.g., Ni) but it appears as if a spin orbit interaction is also required.¹¹⁵ However, the radius r_2 , above, appears to be larger than the electromagnetic radius. This again may be a reflection of the fact that the range of nuclear forces appears as an effective "radius" of the nucleon whenever the radius is measured by a method involving the nuclear force.

Gatha and Riddell¹¹⁶ had noted earlier that a rounding-off of the edge of the (optical model) nuclear sphere would be necessary to fit the experimental data¹¹⁷ on high-energy proton scattering (340 Mev). They also found that an $r_0=1.25$ fermis would provide a better fit of the 340-Mev data than the larger, older, radii.

j. The elastic scattering of (13–42 Mev) alpha particles by heavy nuclei was studied by Farwell and Wegner¹¹⁸ and an interpretation of the observed sharp energy breaks has been given by Blair.¹¹⁹ The theory of such experiments is evidently not simple and probably the estimates of radii should be taken only as upper limits. Allowing for the radius of the alpha particle, the estimate of $r_0=1.5$ fermis was made. It is not clear how reliable this estimate may be.

k. In the Weizsäcker semiempirical formula for nuclear binding energies, there is an electrostatic term for a uniformly charged sphere proportional to

$$E_{el} = -\frac{3(Ze)^2}{5 r_0 A^{\frac{1}{3}}}, \quad (67)$$

and so, in principle, a value for r_0 can be found from the packing-fraction curve. Unfortunately, estimates of r_0 from 1.2 fermis to 1.5 fermis can be made consistent with the present data. If a nonuniformly charged model is introduced, the problem becomes more difficult, but, if the shape of the model is known, a new value of r_0 may possibly be found.

1. We shall not delve into the voluminous literature on nuclear radii determined from studies of natural and artificial alpha-particle radioactivities. This is a subject with a historic background and furnished the first evidence for the quantum-mechanical tunneling process. It may be worthwhile, however, to call attention to a recent paper which proposes some changes

¹¹⁶ D. S. Saxon, Brookhaven Report on Statistical Aspects of the Nucleus, BNL 331 (C-21) Brookhaven (January, 1955).

¹¹⁷ K. L. Gatha and R. J. Riddell, Jr., Phys. Rev. 86, 1035 (1952).

¹¹⁸ Richardson, Ball, Leith, and Moyer, Phys. Rev. 83, 859 (1951).

¹¹⁹ G. W. Farwell and H. E. Wegner, Phys. Rev. 93, 356 (1954); 95, 1212 (1954).

¹²⁰ J. S. Blair, Phys. Rev. 95, 1218 (1954).

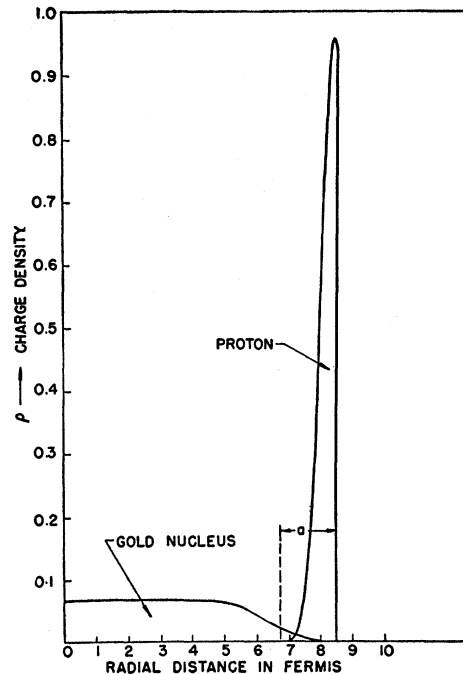


FIG. 52. A proton interacting with a gold nucleus at the old radius for gold, 8.45×10^{-13} cm. Owing to the finite size of the nucleon, there is already some nucleonic interaction at this distance. "a" represents the range of nuclear forces. Note the relatively high charge density of the proton relative to that of the gold nucleus.

in the older theories. Tolhoek and Brussard¹²⁰ use a nuclear model with a surface of finite thickness, resembling the model of Hahn *et al.*³³ This theory gives a value of $r_0=1.13$ fermis in contrast to the older determinations which gave $r_0=1.4$ to 1.5 for the most part.¹⁰² It is not yet possible to know how good the model of Tolhoek and Brussard may be in practice.

Finally, Fig. 52 may serve to remind us that the finite size of the nucleon should be considered when speaking of nuclear radii. This figure shows the charge density (in proton charges per cubic fermi) plotted as ordinate against the distance from the center of a gold nucleus. At the right of the figure a finite Gaussian-model proton, with rms radius 0.70 fermi, is shown at a distance of 8.45 fermis between its center and that of the gold nucleus. This distance corresponds to the conventional radius of gold for which $r_0=1.45$ in Eq. (1). In the figure, "a" indicates an approximate value for the range of nuclear forces. It will be seen that there is a fair overlap, both of charge, and of nuclear force fields. It is not surprising that there is a strong interaction at this distance. This figure should be contrasted with Fig. 1 and exhibits clearly the high average density of the proton's charge cloud when compared with that of a representative nucleus such as gold.

In concluding this section, we may note that many of the newer and some of the older determinations are

¹²⁰ H. A. Tolhoek and P. J. Brussard, Physica XXI, 449 (1955).

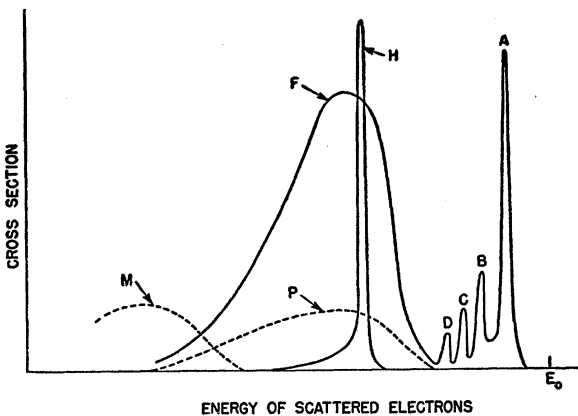


FIG. 53. This figure attempts a summary of the various possible phenomena observed in electron scattering for high momentum transfers. A represents an elastic peak and B , C , D refer to inelastic scattering from nuclear levels. H is the free proton peak observed in hydrogen. P is the incoherent scattering peak of an individual proton (or neutron) in the nucleus. It is broadened with respect to the free proton peak H by motion within the nucleus. F is the simple sum of all such peaks for all the A nucleons in the nucleus. M represents electrons scattered after producing pions. Note that all electrons lie on the low-energy side of E_0 (the incident energy) because of nuclear recoil effects. The figure is not to scale either vertically or horizontally.

consistent with the smaller electromagnetic radii. Still other determinations give stubbornly larger and different figures. Until the nature of the nuclear force is known, many of the "radii" cannot be significantly compared. It is hoped that the constant reference to the quantity r_0 in this section has not focused too much attention on it, since, in reality, nuclei appear to have more than one single parameter (such as r_0) determining their size and shape.

IX. SUMMARY

To summarize in words the results presented in this report would require a lengthy exposition. There would have to be a division of the material into results which are new and need to be checked, and the older, better confirmed results. Some of the older results need not be restated once again. Instead of a repetition of the newer and older conclusions, it is preferable to present the major findings in the form of a single figure and a single table presented below. Each will be inadequate but may serve to suggest new ideas for measurements and theoretical analysis. To accompany the figure and the table, we present the following remarks.

Figure 52 exhibits most of the varied phenomena observed in the electron scattering experiments. This figure is schematic and shows what is seen in a representative nucleus such as carbon at a relatively large scattering angle and at a medium high energy, say, e.g., 70° at 400 Mev. The relative proportions shown in the figure must not be assumed to be accurate.

The incident energy is shown at E_0 . The elastic peak appears at A and the inelastic peaks, due to scattering

from the nuclear levels, are shown at B , C , D . The bremsstrahlung tail of the elastic peak lies on its left side. Note that the elastic and inelastic peaks are shifted to energies lower than E_0 by recoil effects. At lower energies the inelastic continuum appears at F . The individual nucleons scatter electrons incoherently and all the individual cross sections, such as the one shown for proton P , add up to produce the large peak indicated at F . This broad maximum appears near the free proton peak, H , shown in the figure for reference purposes. But it lies below the peak H because of the binding energy of the protons and neutrons in the nucleus. A good part of the scattering in this incoherent peak is due to the magnetic spin-flip process. In this respect neutron and proton are almost equivalent. The study of how the individual proton and neutron peaks add up to make the continuum at various angles should provide an interesting story. If the experiments start with light nuclei, in which there are only a few components, such as D , H^3 , He^3 , He^4 , Li^6 , Li^7 , Be^9 , etc. and proceed to heavier ones, the interaction of the ejected particle with its surroundings may be studied. Furthermore, the momentum distribution of the nucleons should emerge from such studies.

At still lower energies in Fig. 53, pions will be produced and electrons, labeled M , will be scattered in this production process. The dotted line to the left indicates this in a schematic way. It will be recognized that most of the processes described in our report are incorporated in Fig. 53.

It is not possible to show in Fig. 53 the angular distributions corresponding to each of the various features of the diagram. This would require a many-dimensional plot. In place of this we refer to the figures in the report itself, such as Fig. 38 and Fig. 41 and to Table VI described in the next paragraph.

An analysis of these results is given in Table VI. Two parameters, characterizing the charge distributions, are supplied in those cases in which it is possible to do so. Otherwise, a description of the charge distribution is given as well as an equivalent rms radius and r_0 value. The most general features apparent in Table VI are the approximate constancy of the surface thickness and the shrinking away of the flat region as one proceeds to the lighter elements. A simple prescription does not apply to the extremely light nuclei or to the proton. In general, the average central-charge density of nuclei increases as the atomic number decreases, reaching a maximum in the proton. ρ_U in the table gives the charge density of the equivalent uniform model.

It is interesting to look back into the statistical approach of Jensen and Luttinger¹²¹ who applied the Thomas-Fermi model to the nucleus and calculated mean squared angular momenta. They showed that a constant surface layer of 1.8 fermis would give agree-

¹²¹ J. H. D. Jensen and J. M. Luttinger, Phys. Rev. 86, 907 (1952).

TABLE VI. This table gives the radial parameters for the nuclei of column 1 and the appropriate charge (and magnetic) distributions. All quantities used in the table are defined in the text, except the parameters of the Hill model (used only for $^{82}\text{Pb}^{208}$). All distances are given in units of 10^{-13} cm (one fermi unit). The accuracy in surface thickness parameter is about $\pm 10\%$ and may be somewhat poorer for the lighter elements where it is less well defined. The accuracy of the radial parameters is about $\pm 2\%$ except, possibly, in the case of Ta. The accuracy for gold is better than $\pm 2\%$. ρ_U in column 9 is the charge density in proton charge per cubic fermi for the equivalent uniform model and may be compared with Fig. 1 (b). The results for lithium and beryllium are to be considered preliminary.

Nucleus (1)	Type of charge distribution (see Table I) (2)	rms radius (3)	Radius of equivalent uniform model (R) (4)	$r_0 = \frac{R}{A^{\frac{1}{3}}}$ (5)	Skin thickness (6)	Half- density Radius c (7)	$r_1 = \frac{c}{A^{\frac{1}{3}}}$ (8)	ρ_U (9)	$A^{\frac{1}{3}}$ (10)	Comments (11)	Reference number (12)
$^1\text{H}^1$	III, IV, VI, VII mag- netic distribution similar	0.77 ± 0.10	1.00	1.00	0.239	1.00	The charge distribu- tions in column 2 are equivalent to each other. The rms radius is a mean value for all. The magnetic dis- tribution is the same as that of the charge. The fact that $R=1.00$ in column 4 is acci- dental.	42, 55, 68
$^1\text{D}^2$	Charge distribution calculated from deu- teron wave function for Hulthén, etc., potentials.	1.96	2.53	2.01	0.0147	1.26	...	71
$^2\text{He}^4$	III	1.61	2.08	1.31	0.053	1.59	...	42, 49
$^3\text{Li}^6$	XII	2.78	3.59	1.98	0.0153	1.82	...	75
$^3\text{Li}^7$	XII	2.71	3.50	1.83	0.0167	1.19	...	75
$^4\text{Be}^9$	XII	3.04	3.92	1.89	0.0157	2.08	...	75
$^6\text{C}^{12}$	XI	2.37	3.04	1.33	~ 2.0	~ 2.3	1.00	0.051	2.29	$\alpha = 4/3$	77
$^{12}\text{Mg}^{24}$	gU	2.98	3.84	1.33	2.6	2.85	0.99	0.051	2.88	...	46
$^{14}\text{Si}^{28}$	gU	3.04	3.92	1.29	2.8	2.95	0.97	0.056	3.04	...	46
$^{16}\text{S}^{32}$	gU	3.19	4.12	1.30	2.6	3.28	1.03	0.055	3.18	...	46
$^{20}\text{Ca}^{40}$	Fermi	3.52	4.54	1.32	2.5	3.64	1.06	0.052	3.42	...	33
$^{23}\text{V}^{51}$	Fermi	3.59	4.63	1.25	2.2	3.98	1.07	0.055	3.71	...	33
$^{27}\text{Co}^{59}$	Fermi	3.83	4.94	1.27	2.5	4.09	1.05	0.0662	3.89	...	33
$^{49}\text{In}^{115}$	Fermi	4.50	5.80	1.19	2.3	5.24	1.08	0.0605	4.87	...	33
$^{81}\text{Sb}^{182}$	Fermi	4.63	5.97	1.20	2.5	5.32	1.07	0.0572	4.96	...	33
$^{73}\text{Ta}^{181}$	Fermi plus quadru- pole	5.50	~ 7.10	~ 1.25	~ 2.8	~ 6.45	~ 1.14	0.0491	5.65	The radial distances should be considered "effective" radii in view of the quadrupole effects.	61, 88
$^{197}\text{Au}^{197}$	Fermi	5.32	6.87	1.180	2.32	6.38	1.096	0.0581	5.82	...	33
$^{82}\text{Pb}^{208}$	Hill <i>et al.</i> (reference 9) $n=10, s=0$	~ 5.42	~ 7.0	1.18	~ 2.3	~ 6.5	~ 1.09	0.057	5.93	The model of Hill <i>et al.</i> is similar to the Fermi model	9
$^{83}\text{Bi}^{209}$	Fermi	5.52	7.13	1.20	2.7	6.47	1.09	0.054	5.935	...	33

ment with the shell model predictions. This result is suggestive of the data presented in Table VI. It would seem profitable to carry out further work with this model. Additional theoretical approaches are also highly desirable. A few attempts of this kind have been made by various authors.¹²²⁻¹²⁹ It is hoped that some such model will be successful.

X. CONCLUSIONS

In this brief section we wish to remark that the electron-scattering method appears to offer great promise in unraveling the problems of nuclear size and shape and the internal dynamics of nuclei. But it must be emphasized that we do not have complete information on such subjects at the present time. The exper-

iments are just "scratching the surface." Many nuclei still need to be investigated and greater accuracy is needed; absolute cross sections must be obtained. Better resolution between elastic and inelastic scattering should be a fundamental objective and is at present a serious lack. Good electron counters must be made which distinguish high-energy electrons from all other particles having the same momenta. We may summarize these remarks in a familiar way: More and better data are needed. Time is needed to allow the electron scattering results to interact with the results of other methods. Only in this way will it be possible to test the experiments and their findings. It would be desirable to test the validity of electrodynamics by some independent method but this probably requires machines which are not yet built. Time is also needed to improve many of the experimental techniques. New and further development of theoretical ideas appear to be required before a clear picture of many of the detailed findings can be obtained. Some kind of analysis of the many-body problem is a necessity in addition to the prior and more fundamental need of a theory of elementary particles. In this connection everyone awaits the development of a successful, quantitative,

¹²² M. Born and L. M. Yang, Nature **166**, 399 (1950).

¹²³ L. M. Yang, Proc. Phys. Soc. (London) **A64**, 632 (1951).

¹²⁴ D. Ivanenko and W. Rodichev, Doklady Akad. Nauk. S.S.R. **70**, 605 (1951).

¹²⁵ P. Gombas, Acta. Phys. Acad. Sci. Hung. **1**, 329 (1952); **2**, 223 (1952).

¹²⁶ S. D. Drell, Phys. Rev. **100**, 97 (1955).

¹²⁷ M. Rotenberg, MIT Technical Report, Project D.I.C. 6915, No. 6 (1955).

¹²⁸ M. H. Johnson and E. Teller, Phys. Rev. **93**, 357 (1954).

¹²⁹ L. Wilets, Phys. Rev. **101**, 1805 (1956).

meson theory. It is hoped that the next few years may see the realization of some of these goals.

XI. ACKNOWLEDGMENTS

The accumulation of the large body of facts presented in this report is due to a large number of individuals. Many of their names appear in the references. Some may not, and in this case the author begs forgiveness on the grounds that their number is so large that oversights are easily made. The author wishes to thank R. Blankenbecler, E. E. Chambers, J. H. Fregeau, R. H. Helm, J. A. McIntyre, M. Lévy, D. G. Ravenhall, J. F. Streib, M. R. Yearian, and D. R. Yennie for kind

permission to quote their results prior to publication. He sincerely appreciates the generosity of D. G. Ravenhall and D. R. Yennie in taking a great deal of time to explain their results to the author. He has profited greatly from numerous discussions with his colleagues such as F. Bloch, W. E. Lamb, Jr., and L. I. Schiff. He owes much of the successful operation of the devices used in these experiments to F. Bunker, B. Chambers, L. Franklin, A. Knudsen, V. Prosper, and E. Wright, and to R. Mozley and the accelerator group. Finally he wishes to thank L. Becker, A. L. Berg, F. Bunker, R. Keith, A. Marcum, and E. McWhinney for their willing help in completing the manuscript.

Electron Interference Experiments

J. AROL SIMPSON

National Bureau of Standards, Washington 25, D. C.

INTRODUCTION

SINCE the original de Broglie¹ papers in 1924, there have been a number of experiments designed to investigate the wave nature of the free electron. For the purposes of this discussion we shall include only those diffraction experiments where the object was to study the electron rather than the diffractor. The information sought bears on the confirmation of the essential wave nature of the electron, and a quantitative comparison of the predictions of the de Broglie theory as it has been extended over the years. A further purpose, I believe, has been the subconscious desire to discover how far a simple theory, which treats a quasi-monoenergetic beam of electrons² as a monochromatic classical wave field, is valid. The questions that have been discussed since as early as 1930 concerning the length and breadth across the face of the coherent wave train belong in this latter category.

THE EXPERIMENTAL PROBLEM

In order to observe interference effects, several conditions must be satisfied; the history of interference experiments has been the history of the attempts to satisfy more perfectly these conditions. First there must be obtained a "coherent" beam of electrons. This question of what constitutes a coherent beam, or, more precisely, how coherent is the beam arising from any given source, is not a simple question and is discussed at length by D. Gabor in another paper in the series. For the purposes of the experimentalist, however, it

means that the source of the beam must be well defined in energy and position. The exact stringency of the restrictions depends fundamentally on the precise nature of the experiment. In other words, the beam must be monoenergetic; and the size of the effective source, either real or virtual, must be at most a few thousand wavelengths of the illumination. For electron optics these conditions in turn require a highly stable accelerating voltage, an intense source of reasonably monoenergetic electrons, an instrument with a high degree of mechanical rigidity, and freedom from perturbing fields. Second, there must be an "interferometer" such that at the point of observation two or more coherent beams are superimposed in such a manner that the interferences are observable with available means. To accomplish this result two things must be simultaneously true. The path differences introduced into the beam must be smaller than the "coherence length" of the beam, and the angles between the interfering wave fronts, β , must be small so that the fringe spacing, y , which is related to the wavelength, λ , by

$$y = \lambda/\beta, \quad (1)$$

is greater than the resolving power of the observing instrument.

There is one fundamental difficulty that has delayed the realization for electron optics of the classic experiments of Young and Fresnel upon which the wave theory of light optics was founded. To obtain reasonable penetration into the diffractor and freedom from perturbations by stray laboratory magnetic fields, it is highly desirable to work at electron energies on the order of 50 kev. At this energy the electron wavelength is only

¹ L. de Broglie, Phil. Mag. **47**, 466 (1924).

² G. P. Thomson, *Wave Mechanics of the Free Electron* (McGraw-Hill Book Company, Inc., New York, 1930).

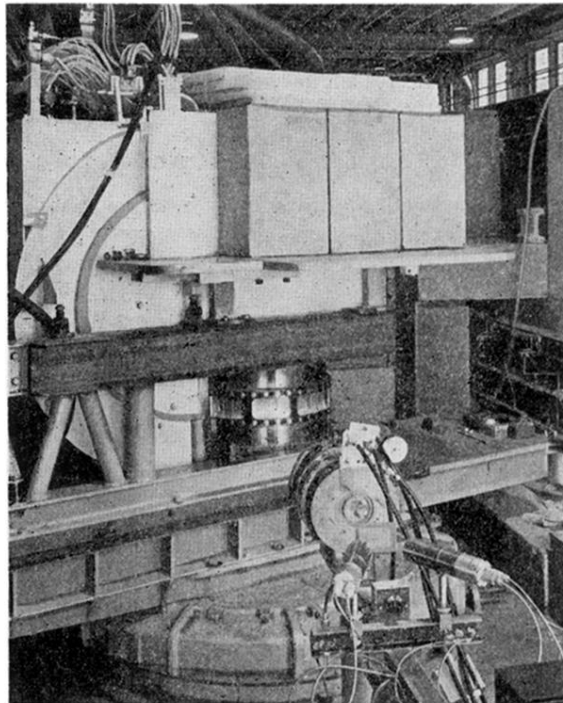


FIG. 15. The semicircular 190-Mev spectrometer, to the left, is shown on the gun mount. The upper platform carries the lead and paraffin shielding that encloses the Čerenkov counter. The brass scattering chamber is shown below with the thin window encircling it. Ion chamber monitors appear in the foreground.

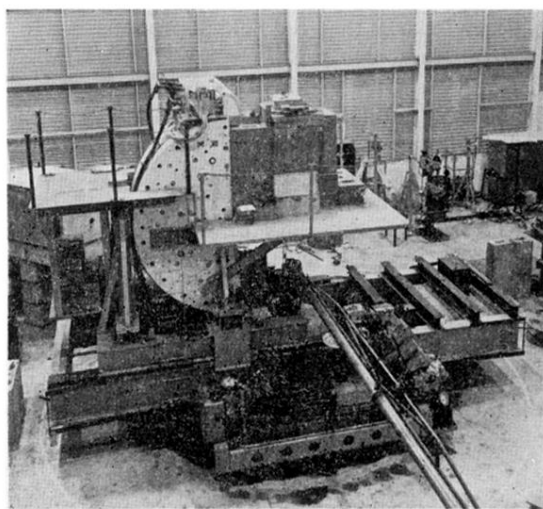


FIG. 19. Photograph of the 550-Mev spectrometer, the gun mount, and shield. The electron beam is brought to the target, shown under the platform, through the vacuum pipe in the foreground.

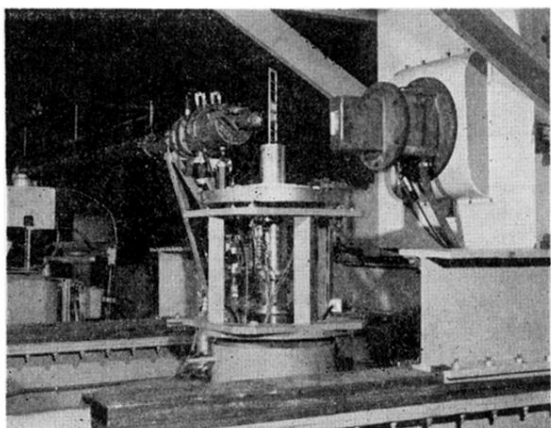


FIG. 22. Details of the monitor, target ladder, and magnet input port.